Computational Design of Interfaces: Mitigating He Damage in Nuclear Fusion Applications

by

Dina V Yuryev

Submitted to the Department of Materials Science and Engineering
in partial fulfillment of the requirements for the degree of

Doctor of Philosophy in Materials Science and Engineering

at the

MASSACHUSETTS INSTITUTE OF TECHNOLOGY

February 2017

© Massachusetts Institute of Technology 2017. All rights reserved.

Author . . . .

Signature redacted

Department of Materials Science and Engineering
December 1, 2016

Certified by . . . .

Signature redacted

Michael J. Demkowicz
Associate Professor
Thesis Supervisor

Accepted by . . . .

Signature redacted

Donald Sadoway
Chairman, Department Committee on Graduate Theses

Computational Design of Interfaces: Mitigating He Damage in Nuclear Fusion Applications

by

Dina V Yuryev

Abstract

In order for nuclear fusion to be a feasible source of energy, materials must be developed that are resistant to the damaging byproducts of a fusion reaction. One of these byproducts is He, that is implanted into the plasma facing wall of the reactor. Once implanted, it causes irreparable damage due to it's insolubility in the material: the He cannot escape in a non-destructive manner. In this thesis, an interface in a layered metal nanocomposite is designed to have desirable precipitation properties, specifically that He precipitates will link up to form stable, continuous pathways. Once in these channels, the He may still migrate within the channels themselves. Thus, channels that terminate at free surfaces may enable controlled He removal via outgassing, thereby averting He-induced damage. In this thesis, computational methods are developed for identifying promising interfaces that give rise to He channels and for modeling He network behaviors at these interfaces. These models are then applied to materials systems of interest to determine if elongated precipitates arise. Finally, experimental results are presented that support computational predictions that Cu-V interfaces result in linear helium channels.

Thesis Supervisor: Michael J. Demkowicz
Title: Associate Professor

Acknowledgments

Finally, I'd like to thank my parents and grandparents for their unwavering love and support in all my endeavorers.

Contents

List of Figures

9

10

13

List of Tables

Chapter 1

Introduction

1.1 Motivation

Fusion power has the potential of meeting world energy demands with minimal environmental impact [4, 5]. The performance and safety of a fusion reactor is primarily governed by the integrity of the plasma-facing wall under operating conditions [6]. During operation, this wall gets bombarded with matter and energy, byproducts of the fusion reaction. As a result plasma-facing materials need to withstand high temperatures, thermal cycling, neutron radiation, light radiation and ion and helium (He) bombardment [7]. While He is often considered a harmless, non-reactive gas, it gets implanted into the plasma facing wall and causes irreparable damage to engineering alloys. Once implanted into a metal, He amplifies radiation-induced embrittlement [8], swelling [9], and surface damage [10]. The destructive effects of He originate in its insolubility: implanted He precipitates out into nanoscale He-filled cavities[11]. Under some conditions, this cavity maintains it's size as a stable "He bubble" up to a diameter of approximately 10nm, while under other conditions it can grow without bound into a void [12, 13]. It is these voids that are responsible for the He-induced damage rather than small scale He bubbles. The current approach to managing implanted helium has two primary components: 1. Maximizing the size at which a harmless He bubble transitions into a damaging void and 2. Increasing the number of nucleation sites for He bubbles to form, decreasing the He flux per bubble, and slowing down the bubble growth rate [14]. These approaches focus on delaying the onset of the "bubble-to-void"

transition.

Recent research has suggested that some interfaces are excellent trapping sites for He bubbles due to their structure [11, 14, 15, 16, 17]. However, the array of interfaces is extensive and to enumerate over all possible interfaces in not feasible. Rather than finding an appropriate interface for He management through brute force, we propose using patterned designer interfaces with properties tailored for mitigation of He damage. While free surfaces can be easily patterned [18, 19, 20], interfaces are buried within a material and thus difficult to access directly. Rather than using, for example, a hydrophobic coating to pattern a free surface as a means of controlling water droplet dynamics [21, 22], we tune interface crystallography and composition as a means of controlling the intrinsic interface structure and thus the interface properties. This thesis will focus on the design and investigation of interfaces that promote precipitation of He bubbles in such a way that they coalesce into long, linear channels, enabling controlled He removal via outgassing, thereby averting He-induced damage, prolonging materials lifetime, and increasing safety.

1.2 Overview of Interfaces

In this section models for classifying the structure of an interface are discribed, particularly focusing on the misfit dislocation model chosen for the design work proposed in this thesis. Furthermore, interface properties are examined and specifically their connection to structure.

An interface in a polycrystalline solid is often thought of as a dividing plane between two adjoining crystals. However, it has an atomic-level structure of its own, which depends on numerous crystallographic and compositional variables. This structure plays a key role in determining a wide range of interface properties, including mechanical, electrical, thermal, and diffusion properties [23]. Thus, if the structure of an interface may be controlled, then–in principle–so may a wide range of its properties.

An interface between misoriented crystals of identical composition and structure (i.e. a homophase interface or grain boundary(GB)) has five macroscopic degrees of freedom (DOFs): three to describe the misorientation of the adjoining crystals and two to describe

the orientation of the interface plane. In addition to these macroscopic DOFs, a complete description of the state of an interface (homophase or herterophase) may require additional "microscopic" DOFs, which detail the atomic-level configuration. The structure, and therefore the properties, of an interface depend on all of these DOFs [23]. A brute force approach to interface structure design that relies on direct enumeration is infeasible. It is therefore necessary to develop a more intelligent approachs towards selecting interfaces whose structures give rise to desired properties.

1.2.1   Classification of Interfaces

Interfaces in polycrystals are either homophase or heterophase. A homophase interface or grain boundary (GB) is formed between two misoriented crystals of identical composition and crystal structure. A heterophase interface is formed when materials of two different phases adjoin each other. The adjoining crystals may differ in composition, crystal structure, or both.

Interfaces that have perfect atomic matching across the entirety of their area are referred to as "coherent". GBs may be coherent and stress free, while heterophase interfaces may generally only be coherent if one of the adjoining crystals is strained such that it matches the crystallography of the neighboring crystal. Since coherent interfaces are often lower in energy than an interface lacking perfect atomic matching, it can be energetically favorable for such straining to occur if the strained crystal is sufficiently thin. However, as the thickness of the strained crystal increases, the elastic energy needed to maintain coherency exceeds the energy difference between the coherent and incoherent interfaces and a coherent-to-incoherent structural transition may occur [24, 25, 26].

Coherent-to-incoherent transitions occur by the nucleation of dislocations, which move through the adjoining crystals and are deposited on the interface. At the end of this transition, the resultant configuration is an array (or arrays) of misfit dislocations at the interface. The long-range elastic fields of this array are equal and opposite to the stress needed to impose coherency at the interface. If the arrays are spaced such that there are patches of coherency between them, the resulting interface is called "semicoherent". However, if the
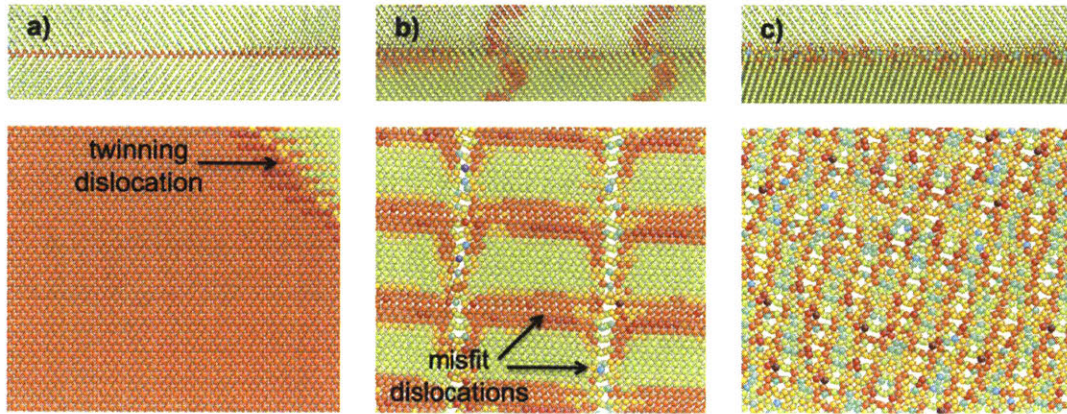
Figure 1-1: Edge-on (top) and In-plane (bottom) views of a) coherent, b) semicoherent, and c) incoherent GBs in α-Fe. The atoms are colored according to coordination number.

dislocation array density is so high such that no coherent patches remain, the interface is classified as "incoherent."

An example of coherent, semicoherent, and incoherent structures is given in Fig. 1, which shows the structure of a GB along {112} planes in α-Fe for different twist angles. The interface in Fig. 1-1.a) is a coherent twin boundary with a single extrinsic dislocation. Both the edge-on (top) and in-plane (bottom) view show perfect atomic matching (except in the region of the dislocation). Fig. 1-1.b) shows an interface with a 5° twist from the coherent configuration in Fig. 1-1.a). It contains two arrays of misfit dislocations. In the inplane view, there are clearly coherent patches between the intersecting dislocations. Finally, Fig. 1-1.c) depicts an interface with a 30° twist from the coherent configuration where the dislocation arrays are so dense that there are no discernable coherent patches. The atoms in these figures are colored by coordination number. Atoms with the same color have the same structure and thus are "ordered", while atoms of different color have different structure and are "disordered".

It has also been suggested that some incoherent interfaces may be amorphous and experimental studies have imaged interface films that indeed appear to be amorphous [27, 28]. The idea of amorphous interfaces, however, remains controversial. For example the existence of thin intergranular disordered films of nanometer thickness has been predicted in the atomic structures of certain high-energy GBs in silicon [29]. However, it was subsequently

argued that these GBs do contain structural ordering after all [30].

1.2.2 Quantitative Interface Structure Models

Several models have been developed to describe and predict the structure of different classes of interfaces. The coincident site lattice (CSL) model, the misfit-dislocation model, and the structural unit model (SUM) are the most commonly used ones for describing coherent, semicoherent, and incoherent interfaces, respectively.

In the CSL model, the degree of fit (Σ) between two crystals at an interface is described as the reciprocal of the number of coincident sites (i.e. atomic sites common to both lattices) to the number of total sites. While two misoriented crystals will have an identical CSL for a given misorientation (because CSL only takes into account 3 of 5 of the DOFsjust the misorientation of the crystals), the structure of the boundary will drastically change depending on the orientation of the interface plane (it does not depend on the Σ value alone) [31]. This model is a purely geometric one in which boundaries with more coincident sites are thought to have lower energies than boundaries with fewer coincident sites [32]. Mori *et al.* measured the grain boundary energies for a [001] twist boundary in copper (Cu) [33]. They found that while Σ boundaries did, in general, have lower energies than general boundaries (those that can not be described by a CSL), there was no clear relationship between Σ number and energy, e.g. lower Σ values did not correspond to lower GB energies. This implies that GB energy does not depend on Σ values alone. Although CSLs can only describe a small fraction of GBs, they are more frequently encountered in polycrystalline materials than non-CSL boundaries. Another advantage of the CSL model is that the interface can be thought of as a structure of identical repeating units. If the properties of a single unit can be characterized, the properties of the entire interface can be inferred, but only for certain GB plane orientations. While this model is useful because coherent CSL type boundaries are often low in energy and therefore abundant, it has shortcomings when it comes to describing a broader class of interfaces. For example, CSL is only useful in describing GBs because heterophase interfaces typically have no CSLs. Furthermore, the CSL does not take into account the orientation of the interface plane, which
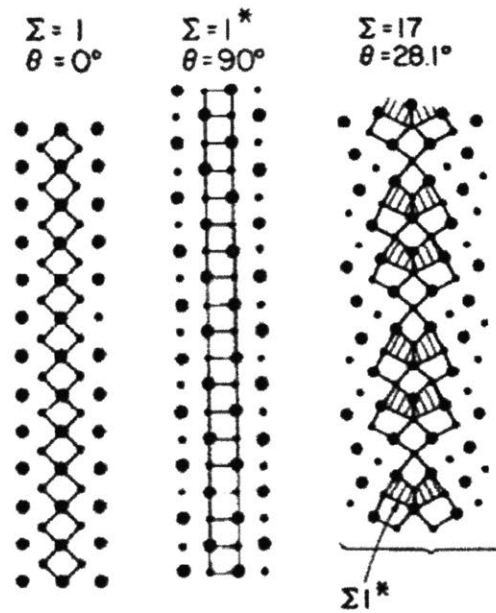
Figure 1-2: $\Sigma 1$ and $\Sigma 1*$ are favored boundaries. A $\Sigma 17$ boundary can be described to be made up of repeating units made up of $\Sigma 1$ and $\Sigma 1*$ structures[1].

plays an important role in determining interface structure.

It has been observed that the structure of some non-CSL boundaries may be described as consisting of recurring structural units drawn from coherent structures. This observation led to the development of the structural unit model (SUM) of interfaces. The SUM defines a structural unit as a small group of atoms (on the order of 10 atoms), arranged in a characteristic configuration drawn from coherent interfaces, which are referred to as delimiting boundaries. All other boundaries that have misorientations and boundary planes between the favored boundaries can be thought of as being made up of a mixture of the structural units present in the favored boundaries [34, 1].

1 and $\Sigma 1*$ boundaries (i.e. a perfect crystals) are the simplest delimiting boundaries used. The structure of these boundaries is identical, as demonstrated in Fig. 3, but they give rise to differing structural units. An example of an application of the SUM to a [001] tilt boundary is shown in Fig. 1-2. The structure of this boundary can be described in terms of distorted $\Sigma 1$ (empty boxes) and $\Sigma 1*$ (shaded boxes) structural units [1]. As the tilt axis changes, so does the number and distribution of these structural units within the boundary.

24

One of the key strengths of the SUM is that it may be applied to incoherent interfaces. However, the SUM has many limitations. It is not applicable to all boundaries in all materials: the SUM cannot be used for both twist and tilt GBs [1]. First, to use the SUM it must be possible to define favored boundaries, which is problematic for interfaces between materials that have no CSLs. In practice, this restriction has confined application of the SUM to GBs in cubic materials. Furthermore, the SUM does not give unique descriptions of GBs: different combinations of structural units can be used to describe a single boundary and there is no way to determine the best choice of units. Also, as seen in Fig. 1-2 the units can be distorted for some boundaries. These distortions may be very large, putting into question the validity of the model. Another limitation of the SUM stems from its assumption that the structure of any GB with a given character may be described with a single set of structural units. In fact, however, the structural units that are present at a given boundary may be material dependent. A computational study done by Rittner and Seidman demonstrated that while the SUM is applicable to a range of Al boundaries, the results cannot be used to predict the structure of same Σ boundaries in Ni [35]. In conclusion, the capability of the SUM is descriptive rather than predictive.

The misfit dislocation model is useful in describing semicoherent interfaces. In this model, the structure of the interface is described by one or more intersecting arrays of misfit dislocations. Between the dislocations are coherent patches of interface. The number and character of the misfit dislocations in an interface is related to the strain needed to impose coherency. Therefore it is possible to predict a misfit dislocation configuration in an interface, specifying the spacing, direction, and Burgers vector of the dislocations. O-lattice theory [36, 37] and the Frank-Bilby equation (FBE) [23] provide some insight into the misfit dislocation structure at a semicoherent interface.

O-lattice theory computes the distribution of misfit dislocation arrays, giving geometrical information about dislocation arrangement. One way to interpret the results of O-lattice theory is that it gives the distribution of misfit dislocation intersections (MDIs). However, it cannot uniquely specify misfit dislocation Burgers vectors and different sets of dislocation arrays can give rise to an identical distribution of MDIs. Each interface can have up to three sets of dislocation arrays. In its original form [38, 39], O-lattice theory can only be

25
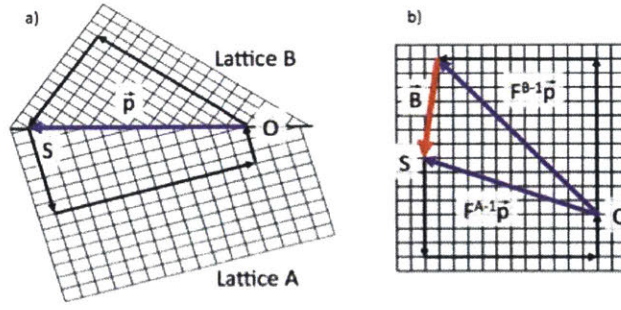
Figure 1-3: a) Burgers circuit that encloses a vector $\vec{p}$ that lies within the interface b) Burgers circuit redrawn in the reference configuration with closure failure.

used for crystal structures that can be related to each other through uniform deformations (e.g. it can handle FCC/BCC interfaces but not BCC/HCP because transforming between these two structures requires a deformation and a shuffle of atoms).

The Frank-Bilby equation can be use to determine the average Burgers vector content of an interface [23]. This equation may be derived by drawing a Burgers circuit that encloses a probe vector $\vec{p}$ in the interface as shown in Fig. 1-3.a). The crystals on either side of the interface are related to some reference state by uniform displacement gradients F^A and F^B. If the Burgers circuit is then redrawn in the reference state, there will be a closure failure as shown in Fig. 1-3.b):

$$\vec{B} = [(F^B)^{-1} - (F^A)^{-1}]\vec{p} \tag{1.1}$$

$\vec{B}$ may be interpreted as the sum of the Burgers vectors of all dislocations crossed by $\vec{p}$. However, it cannot uniquely specify spacing or directions of the dislocation arrays. For example, an array with Burgers vector $\vec{B}$ is equivalent to an array that has twice the density of misfit dislocations but Burgers vector of $\vec{B}/2$. To fully characterize the dislocation structure, additional assumptions must be made [40].

Typically, to fully predict the misfit dislocation structure of an interface, defined by the spacing between dislocations, the dislocation line direction, and the Burger's vector, it is necessary to use atomistic level modeling [41, 42]. This methodology is computationally costly as it requires the tracking of millions of variables. However, recently methods

26

have been developed to determine misfit dislocation array structure using mesoscale modeling which are on the order of 100x faster than using atomic simulation [43, 44]. This methodology relies on O-lattice theory to calculate dislocation line direction and spacing. Anisotropic elasticity theory is used to calculate the Burgers vector, yielding multiple possible solutions [45]. To identify the correct solution, the lowest interface energy is determined using the elastic energy of the misfit dislocations.

It is only appropriate to use the misfit dislocation model at interfaces where individual misfit dislocations can be identified. Thus for large misfits (for example big differences in lattice parameters or structure) or large misorientations (or both), the dislocations begin to overlap and the misfit dislocation model no longer applies.

The misfit dislocation model is a promising for making predictions of the structure of an interface. It may be applied to some heterophase interfaces and can describe interfaces with general misorientations of crystals. Although this model has limitations, it provides the distribution of MDIs allowing for the predictions of precipitation behavior at semicoherent interfaces.

1.2.3   Effect of semicoherent interface structure on properties

Interface structure plays a key role in determining interfacial properties. Properties such as segregation, diffusion, and precipitation governed by interface misfit dislocations are discussed here. Both the misfit dislocations and their intersections influence behavior.

The segregation of solutes to interfaces has been observed in a variety of alloy systems. For example, in austenitic stainless steels, chromium (Cr) and carbon (C) may segregate to grain boundaries [46]. This process is the mechanism of sensitization in stainless steels, which negatively affects their corrosion and fracture resistance [47]. Because of its technical importance, the effect of interface structure on segregation in steels has been widely studied. Laws and Goodhew measured the full width half maximum (FWHM) of Cr concentration profiles at the GB for a variety of CSL and non-CSL grain boundaries. They found that the FWHM did not depend on whether the boundaries were CSL or not, and furthermore the -value of the CSL boundaries did not have a correlation with the FWHM. For

27

example, Σ3 and Σ11 boundaries exhibited among the narrowest Cr concentration profiles, whereas 9 boundaries exhibited profiles that were twice as wide. Non-CSL boundaries also had both wide and narrow profiles. They concluded that the differences in concentration profile width, and thus segregation of Cr, must be a function of the atomic packing at the boundary, which depends on both misorientation and the GB plane orientation [48].

Another study done by Isheim et al. examined the relationship between coherency and solute segregation at metal/metal-nitride heterophase interfaces. They found that molybdenum nitride particles in Fe-2at% Mo-X (where X=0.4at% Sb or 0.5at% Sn) formed with either a very thin platelet type structure or a much thicker structure of coarser plates. The thin plate particles formed a coherent interface whereas the coarser plates formed a semi-coherent interface with the Fe-rich matrix. They observed segregation of large Sb and Sn atoms only to the thicker precipitates. They concluded that there is a preference for segregation to interfacial misfit dislocations due to the excess free volume associated with the semi-coherent interface [49]. Simulations have contributed to the understanding of the relationship between interface structure and segregation. In Monte Carlo simulations of segregation at [001] twist boundaries in Pt(Au) alloy, Seki et al. varied twist angle between the crystals from 0 to 45° and measured the spatial distribution of Au atoms at the interface [50]. They determined that Au atoms segregate primarily to the cores of the misfit screw dislocations formed at the boundary and found that the Au concentration increased linearly as the twist angle increased, saturating at ~ 35°. This is because as twist angle increased, so did misfit dislocation density. Once dislocation cores began to overlap (i.e. the interface is incoherent)the interface was saturated and there is no preference for the Au to segregate to specific locations within the boundary [51]. In summary, the literature suggests that the structure of interfaces, in particular, the misfit dislocation structure, plays a role in determining segregation properties of solutes.

Interface structure not only affects segregation properties at interfaces, but also plays an important role in diffusion. Atomistic studies have shown that highly mobile He interstitials in α-Fe migrate readily along screw dislocation cores [52]. Thus, in pure twist GBs, screw misfit dislocations provide fast pathway for 1-D He diffusion.

The phenomena of dislocations acting as fast paths for diffusion has been observed

experimentally. Average diffusivity (measured by the tracking of a radioactive tracer) increased with increasing misorientation angle for tilt boundaries in Cu/Au bicrystals as observed in a study done by Couling and Smoluchowski [53]. They found that at some critical angle, the average diffusivity saturated. They concluded that the increased diffusivity was correlated to an increase in misfit dislocation density at higher misorientations. However, at some critical angle the dislocation arrays were so closely spaced that diffusion was easy in all directions. Sommer et al. [54] investigated the diffusion of a radiotracer in a Au/Cu bicrystal. In this study they measured diffusion in two mutually perpendicular directions in a (111) interface and in a (011) interface between two FCC crystals with different lattice parameters. The (111) interface was described as having a hexagonal network of misfit dislocations while the (011) interface had an anisotropic, (different Burgers vectors and spacing for each set of dislocation arrays) mutually perpendicular network of misfit dislocations. They found that diffusion in the (011) interface was anisotropic whereas it was nearly identical in the two directions measured for the (111) interface. This study demonstrates the correlation between diffusion and the structure and directionality of dislocations in an interface.

Like segregation and diffusion, precipitation is influenced by interface structure. Both simulations and experiments have show that fluid (liquid or gas) precipitates tend to accumulate and cluster into bubbles at inhomogeneities in materials such as GBs, interfaces, and dislocation rather than in perfect crystalline grain interiors [55]. In particular, the precipitation behavior of He is of interest due to it's presence in nuclear materials systems. Helium precipitate size and density have been observed to vary from grain boundary to grain boundary [56]. In an experimental study, Thorsen et al. observed that low energy boundaries contained smaller He precipitates and smaller densities of precipitates then boundaries that were likely to have higher energy [57].

In addition to GBs acting as preferential areas for helium precipitates, it has been found that dislocations are preferred nucleation sites for He. Atomistic studies on the interaction of He with α-Fe have shown that He is bound to both edge and screw dislocations in α-Fe to a distance of approximately two Burgers vectors from the core of the dislocation. The binding energies correlate with the excess atomic volume near the core regions (i.e. high

29

He dislocation bonding energies indicate high excess atomic volume)[58, 52]. Thus in pure twist and tilt GBs that contain misfit screw and edge dislocations respectively, the misfit dislocations act as preferred nucleation sites, due to more excess atomic volume.

Singh and Leffers experimentally studied the formation of He precipitates in aluminum (Al) GBs. They found that while He precipitates formed on dislocations in the boundary, dislocation nodal points or locations of dislocation intersection were even more strongly preferred. The precipitates that formed within the GB were larger than those observed in the matrix, indicating a preference for He to precipitate at GBs. Additionally, the authors observed rows of precipitates in the GB that appeared parallel and regularly spaced and were thought to have nucleated on MDIs. They also found that precipitate distribution varied from boundary to boundary, indicating a dependence of He behavior on GB structure, namely the density of dislocation intersections [59].

Figure 1-4 demonstrates the distribution of He bubbles in a) a single crystal of Au, b) at a ~ 1° twist boundary on {100} planes in a Au bicrystal, and c) a Monte Carlo simulation of a ~ 2° {100} twist boundary in Cu, which has the same crystal structure as Cu. Both the TEM image and simulation demonstrate that He preferentially precipitates at the dislocation nodes. Furthermore, this study shows the effectiveness of the boundary at collecting He from the neighboring crystalline material [2]. In conclusion, He precipitation depends on interface structure and in particular He demonstrates a strong tendency to precipitate at MDIs.

1.2.4   Growth mode of He precipitates at semicoherent interfaces

Recently, a mechanism for the way He precipitates at semicoherent interfaces has been suggested through atomistic modeling [60]. This study focuses on a FCC/BCC Cu-Nb interface due to the availability of experimental results [14, 61] and validated potentials [62]. It has been experimentally observed that Cu-Nb follows the Kurdjumov-Sachs (KS) orientation relation where a FCC Cu {111} plane neighbors a BCC Nb {110} plane and an interfacial Cu <110> direction lies parallel to a NB <111> direction. Though atomistic simulations, it has been shown that this interface contains two sets of parallel misfit dislo-
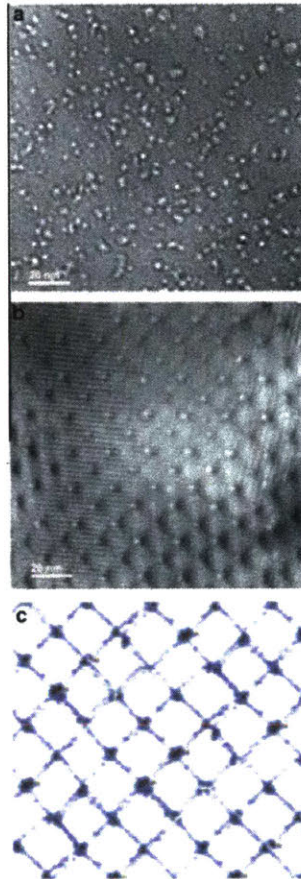
Figure 1-4: a) He precipitates in single crystal Au. b) Plane view of a ~ 1° twist GB in Au. He precipitates (bright dots) decorate the nodes of the GB dislocation network. c) Monte Carlo simulation of He precipitates at a ~ 2° twist GB in Cu [2].

cations, thus this interface can be described as semicoherent [61]. In agreement with the work reviewed in the preceding sections, the study found that successively added He atoms aggregate into clusters located at MDIs. These clusters preferentially grow into the Cu side of the interface likely due to lower vacancy formation and migration energies in Cu than Nb.

Up to about 20 He atoms, the clusters grow as flat platelets along the interface while maintaining a thickness of two atomic layers. These platelets are stable even when there is a vacancy supersaturation. Beyond about 20 atoms, however, the clusters grow by increasing their thickness one atomic layer at a time, while maintaining a constant area at the interface.

In order to explain this mechanism of He growth, it is necessary to consider interface wetting, the phenomena that dictates He favorability towards adhering to the interface. Consider three surface energies that occur when He is at an interface formed between two elements A and B. γ_{AB} is the location-dependent energy of an interface between elements A and B, γ_{AHe} is the interface energy between helium and element A, into which the helium precipitates grow, and γ_{BHe} is the interface energy between helium and element B[63]. From these energies an excess interface wetting energy can be derived:

$$W = \gamma_{AB} + \gamma_{AHe} - \gamma_{BHe} \tag{1.2}$$

When W<0, it is energetically favorable for He to exist as a cluster or bubble entirely within A. However, when W>0, the surface energy of the precipitate is minimized when he He cluster wets the interface. The interface energy determines the He bubble contact angle [64] which is discussed further in section 3.3.

Applying this general equation to the Cu-Nb system, if the Cu-Nb interface had a single uniform surface energy, then He precipitates would either wet or not wet the interface. However, the Cu-Nb interface energy is not uniform over dimensions comparable to the size of the He platelets mentioned above. Thus, certain areas of the interface may satisfy the condition for wetting while others do not. It was determined through atomistic modeling that interface regions around misfit dislocation intersections have high energy and satisfy the wetting condition (W>0) [60]. The regions between the dislocation intersections have

32

considerably lower energy and do not satisfy the wetting condition (W<0). As such, He clusters tend to grow at dislocation intersections. Once a cluster has completely covered the high energy region near a dislocation intersection, no further wetting is possible and the He grows into the Cu layer.

The implication of this finding is that it is not necessary to know the exact atomic structure of an interface to know where He will preferentially precipitate. Rather, it is sufficient to know the position-dependant energy distribution and, more specifically, the regions of sufficiently high energy for wetting to occur (e.g. dislocation intersections as in the example above). This description of He precipitate growth relies on the thermodynamics of interfaces and free surfaces and therefore is not limited to the model interface discussed above, but can be expected to hold for any surface.

1.3   Thesis overview

This thesis designs semicoherent interfaces with energy distributions that cause He to precipitate into stable, connected pathways. The first part of this work focuses on developing computational methods for identifying promising interfaces that give rise to He channels and for modeling He network behaviors at these interfaces. The second part of this work focuses on applying the developed model to interface systems of interest with non-uniform interface energies.

Chapter 2 develops an approach to interface design using O-lattice theory as a means of predicting MDI structure given crystallography and composition. Design criteria is used to identify a candidate interface, Cu-V, as a "proof of concept" materials system that gives rise to He channels. Chapter 3 describes a phase field model that can simulate the growth, coalescence, and stability of He precipitate morphologies on interfaces with location dependent energies. Chapter 4 applies the phase-field model to the Cu-V interface to determine if He channels do indeed form at these interfaces. Finally, Chapter 5 applies the phase-field model to interfaces that have high energy features other than MDIs, namely threading dislocations. The simulations are compared to experimental results of implanted Cu-V biylayer and trilayer systems. We conclude that He channels do form as a result of the intrinsic

interface structure of a Cu-V trilayer.

Chapter 2

Calculating MDI distributions with O-lattice Theory

2.1 Introduction

O-lattice theory is a well-known method for predicting certain features of the internal structure of interfaces between crystalline solids. Provided the crystallography of an interface, it gives the distribution of periodically recurring structural elements, such as MDIs or regions of local coherency [23, 40]. Rather than using it to predict interface structure from interface crystallography, we use it to design interfaces with pre-specified internal structure by controlling interface crystallography. In this section we perform O-lattice calculations of FCC||BCC interfaces and apply design constraints to isolate interfaces with desirable precipitation properties, namely that He coalesces into long, linear channels.

2.2 O-lattice calculation for FCC||BCC interface

O-lattice theory calculates locations of O-lattice points, which are points of "best match" in an interface. To better understand the concept of best match, consider the following construct: two crystals are misoriented and parallel cuts are made to both at a prescribed plane orientation. The cut faces subsequently adjoined. When the boundary is relaxed, the atoms will shift slightly, except those at a location of "best match". This shift will

result in areas surrounding the points of "best match" to extend into coherent patches (i.e. regions of perfect atomic matching) and the areas of bad match" to contract to dislocations. The superlattice that describes the points of best match (i.e the distribution of coherent patches) will have an identical distribution to the superlattice that describes the points of worst match: the distribution of MDIs.

To promote precipitation of He into linear channels, we seek interfaces with MDIs spaced closely in one direction, $\hat{p}$ and far apart in the perpendicular direction, $\hat{n}$ as shown in Figure 2-1. As He bubbles nucleate at MDIs and grow, they are expected to impinge upon each other, coalescing and forming a linear channel along $\hat{p}$. If neighboring channels are sufficiently far apart, then they do not interact and the interface area between them remains free of precipitates. This design objective calls for a highly anisotropic MDI distribution in order promote precipitation of He into linear channels. Some semicoherent interfaces, such as low-misorientation grain boundaries in cubic metals [2], tend to contain relatively isotropic MDI distributions and are therefore poor candidates for our design. We choose to investigate heterophase interfaces formed by joining a 111 plane of a face-centered cubic (FCC) metal to a 110 plane of a body-centered cubic (BCC) metal. MDI distributions at such interfaces have been studied extensively and are known to be anisotropic [61, 41].

Within this class of interfaces, there are two parameters that influence MDI distributions: the ratio of cubic lattice parameters in the neighboring crystals, $\rho = \alpha_{fcc}/\alpha_{bcc}$, where α_{fcc} is the lattice parameter of the FCC crystal and α_{bcc} is the lattice parameter of the BCC crystal, and the twist angle θ describing the relative rotation of the crystals parallel to the interface plane. We measure θ with respect to the Nishiyama-Wasserman (N-W) orientation relation, where a BCC <100> direction is parallel to a FCC<110> direction. ρ and θ define the interface design space.

O-lattice theory calculates two basis vectors $\vec{u}$ and $\vec{v}$, which describe translations of the MDI lattice. To determine these basis vectors, first we must find a displacement gradient matrix, A, that takes a set of translation vectors $\vec{x}_{fcc}$ of the interfacial FCC $\{111\}$ plane and maps them to corresponding translation vectors $\vec{x}_{bcc}$ of the interfacial BCC $\{110\}$ plane: $A\vec{x}_{fcc} = \vec{x}_{bcc}$ [65]. When the $\theta = 0°$, we can write the displacement gradient as $A_0 = X_{bcc}X_{fcc}^{-1}$, where X_{bcc} and X_{fcc} are 2×2 matrices whose columns contain corresponding

36
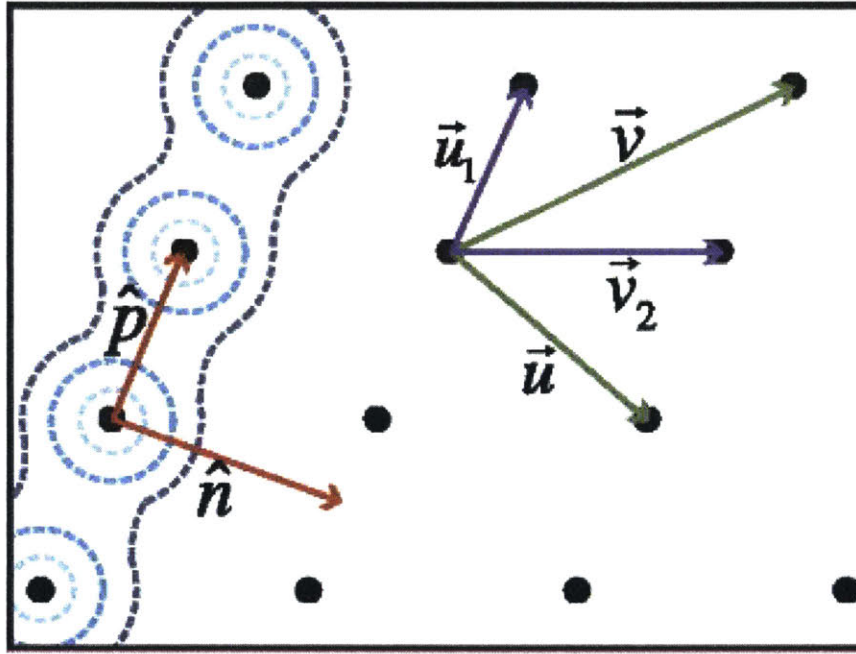
Figure 2-1: The distribution of MDIs (black dots) desired in our design: closely spaced along $\hat{p}$ and far apart along $\hat{n}$ ($\hat{n} \perp \hat{p}$). He bubbles precipitating on MDIs are expected to link up and form continuous linear channels along $\hat{p}$ as illustrated by the dotted contours. O-lattice theory gives translation vectors of the MDI lattice, $\vec{u}$ and $\vec{v}$. From these, Gaussian lattice reduction determines the shortest and second shortest MDI basis vectors $\vec{u_1}$ and $\vec{v_2}$.

translation vectors $\vec{x}_{bcc}$ and $\vec{x}_{fcc}$. These matrices may be written in many equivalent ways, for example,

$$X_{fcc} = \alpha_{fcc} \begin{bmatrix} \sqrt{6}/4 & \sqrt{6}/4 \\ -\sqrt{2}/4 & \sqrt{2}/4 \end{bmatrix}, X_{bcc} = \alpha_{bcc} \begin{bmatrix} \sqrt{2}/2 & \sqrt{2}/2 \\ -1/2 & 1/2 \end{bmatrix}$$

In this configuration the blank direction points along the x-axis and the blank direction points along the y-axis. The BCC <100> direction is parallel to the FCC <110> direction as specified by the N-W orientation relation. We can imagine rotations of the FCC translation vectors relative to the BCC translation vectors. For non-zero θ values we can find A, where $A = R(\theta)A_0$, where $R(\theta)$ is a rotation matrix applied to the bcc side of the interface. We can calculate the MDI distribution using the O-lattice equation [65]:

$$\begin{bmatrix} \vec{u} & \vec{v} \end{bmatrix} = (I - A^{-1})^{-1}X_{fcc} \tag{2.1}$$

where I is the identity matrix. When expressed in units of α_{fcc}, $\vec{u}$ and $\vec{v}$ only depend on ρ and θ.

The $\vec{u}$ and $\vec{v}$ vectors given by equation 2.1 may be any two translation vectors of the MDI lattice. In general, neither of them lies along the direction of smallest MDI spacing, $\vec{p}$. We use Gaussian lattice reduction to determine the shortest and second shortest MDI basis vectors, $\vec{u_1}$ and $\vec{v_2}$ [66], starting from any given $\vec{u}$ and $\vec{v}$. The Gaussian lattice reduction algorithm can be seen in Appendix A. The shortest distance between MDIs is $l_{min} = |\vec{u_1}|$. From $\vec{u_1}$ and $\vec{v_2}$, we also determine the perpendicular distance $l_\perp$ between rows of closest-spaced MDIs, as shown in Figure 2-1. Both quantities are expressed in units of α_{fcc}.

Figure 2-2 a) and b) shows l_{min} and $l_\perp$, respectively, as functions of θ and ρ. They demonstrate remarkably rich variations of l_{min} and $l_\perp$ across the design space. Neither l_{min} or $l_\perp$ are monotonically increasing or decreasing with θ or ρ.

2.3 Applying design criteria to l_{min} and $l_\perp$

To select the θ and ρ that represent interfaces where coalescence of He bubbles into continuous linear channels is likeliest, we prescribe three physics-based design criteria:

38
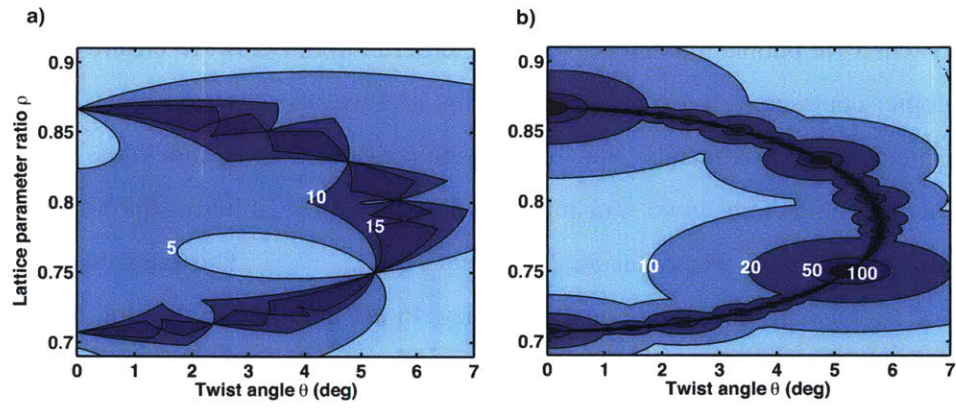
Figure 2-2: Contour plots of l_{min} and $l_\perp$ over the design space, in units of α_{fcc}, described by θ and ρ. The design objectives call for l_{min} values that fall into lighter regions in (a) and $l_\perp$ values that fall into darker regions in (b).

1. l_{min} must be small enough so that He bubbles growing at MDIs coalesce before becoming unstable He-filled voids,

2. $l_\perp$ must be large enough so that neighboring channels do not interact, and

3. $l_\perp$ must not be so large that implanted He impurities cluster and precipitate before they are able to diffuse to the closest channel.

The purpose of criterion 1 is to avoid the "bubble-to-void transition": an osmotically driven instability of He precipitates under vacancy supersaturation [12, 13]. Criteria 2 and 3 ensure that there are precipitate-free regions between neighboring channels.

Under irradiation conditions relevant to nuclear energy, the "bubble-to-void" transition occurs when He bubble diameters are on the order of 10nm [13]. To ensure that adjacent He bubbles coalesce well before they reach this size, we state criterion 1 as $l_{min} < 7$, which corresponds to approximately 3nm for transition metals. Thus, individual bubbles will reach a maximum diameter of 3nm before coalescing with neighboring bubbles, preventing a void from forming. For criterion 2, we require $l_\perp > 3l_{min}$. This ensures that adjacent rows of bubbles are far enough apart that they do not interact. To develop a quantitative expression for criterion 3, we require that the fraction f_{bind} of implanted He atoms that form di-helium clusters (which we assume to be immobile) before reaching a channel be below a specified limit: $f_{bind} < f_{bind}^{max}$.

We define f_{bind} as the proportion of the rate of di-helium cluster formation (R) of the total rate of He arrival at the interface (K_i):

$$f_{bind} = R/K_i \qquad (2.2)$$

Assuming that all of the He implanted into a crystalline layer of thickness t_l which is centered on an interface of thickness $t_i = 2\alpha_{fcc}$ becomes trapped at the interface,

$$K_i = K_0 \frac{t_l}{2\alpha_{fcc}} \qquad (2.3)$$

K_0 is the number of He atoms implanted per unit volume per unit time. The operating conditions of an implanter or reactor determine K_0. To ensure our design is conservative,

40

we use the especially high implantation rate $K_0 \approx 10^{32} m^3/s$, characteristic of the plasma-facing wall of a fusion reactor [67]. To find the reaction rate, we use mean field reaction rate theory[68] to define the reaction rate as:

$$R = 2K_{2He}\bar{c}_{He}^2 \tag{2.4}$$

where K_{2He} is the rate constant calculated assuming one of the He species is immobile and the other is mobile and $\bar{c}_{He}$ is the average concentration of implanted He. Since both He are mobile, we multiply K_{2He} by a factor of 2. The reaction rate constant K_{2He} is equal to

$$K_{2He} = 12\alpha_{fcc}D_{He} \tag{2.5}$$

where D_{He} is the temperature dependent diffusivity of interstitial He. Within the interface, steady-state He diffusion between two adjacent channels obeys

$$D_{He}\frac{\partial^2 c}{\partial x^2} + K_i = 0 \tag{2.6}$$

We calculate a general solution to the partial differential equation above:

$$c(x) = -\frac{K_1}{2D_{He}}x^2 + C_0 x + C1 \tag{2.7}$$

where C_0 and C_1 are constant coefficients. We apply the boundary conditions $c(0) = c(\alpha_{fcc}l_\perp) = 0$ (no He re-emission from channels) to obtain the expression for c(x):

$$c(x) = -\frac{K_1}{2D_{He}}x^2 + \frac{K_1\alpha_{fcc}l_\perp}{2D_{He}}x \tag{2.8}$$

Finally, we average c over the distance between neighboring channels, $\alpha_{fcc}l_{bot}$,

$$\bar{c} = \frac{1}{\alpha_{fcc}l_\perp - 0} = \int_0^{\alpha_{fcc}l_\perp} -\frac{K_i}{2D_{He}}x^2 + \frac{K_i\alpha_{fcc}l_\perp}{2D_{He}}xdx \tag{2.9}$$

which yields

$$\bar{c} = \frac{K_i\alpha_{fcc}^2 l_\perp^2}{12D_{He}} \tag{2.10}$$

41

We plug in the expression for $\bar{c}$ and K_{2He} into equation 2.4 giving us the expression for R:

$$R = \frac{K_i^2 \alpha_{fcc}^5 l_\perp^4}{6D_{He}}$$ (2.11)

Finally we plug in 2.11 and 2.3 into the expression for f_{bind} 2.2:

$$f_{bind} = l_\perp^4 \frac{K_0 \alpha_{fcc}^4}{12D_{He}}$$ (2.12)

To determine how severely criterion 3 constrains our design, we calculate f_{bind} as a function of temperature and layer thickness, t_l, for three values of $l_\perp$: 20, 25, and 30. Using Cu as a prototype, we take $\alpha_{fcc} = 0.36$ and assume D_{He} equals the self-interstitial diffusivity given in Ref. [69]. We select $f_{bind}^{max} = 10^{-2}$, signifying more than 99% of the implanted He arriving at channels rather than forming dihelium clusters between channels. We plot envelopes where $f_{bind} < f_{bind}^{max}$ in Fig. 3. For first wall conditions in fusion reactors [67], criterion 3 is met over a wide range of implantation temperatures and layer thicknesses t_l, but a narrow range of channel spacings, $l_\perp$. Based on the chart, we choose to implement $l_\perp < 30$. This choice meets the condition $f_{bind} < f_{bind}^{max} = 10^{-2}$ within the corresponding temperature and layer thicknesses envelope shown in Figure 2-3. From Figure 2-3 we can see that for temperatures of $500°C$ and above, we require layer thicknesses of 5-10nm. Multilayered metallic composites with layers as thin as 5nm have been successfully deposited in the past. Furthermore, maximizing the number of interfaces maximizes the number of available He trapping sites, making our material more effective at He-induced damage mitigation. Thus it is reasonable to consider layers on this scale.

2.4 Results

We apply the constraints imposed by our physics-based criteria on our contour plots for l_{min} and $l_\perp$:

$$l_{min} < 7$$

$$3l_{min} < l_\perp < 30$$
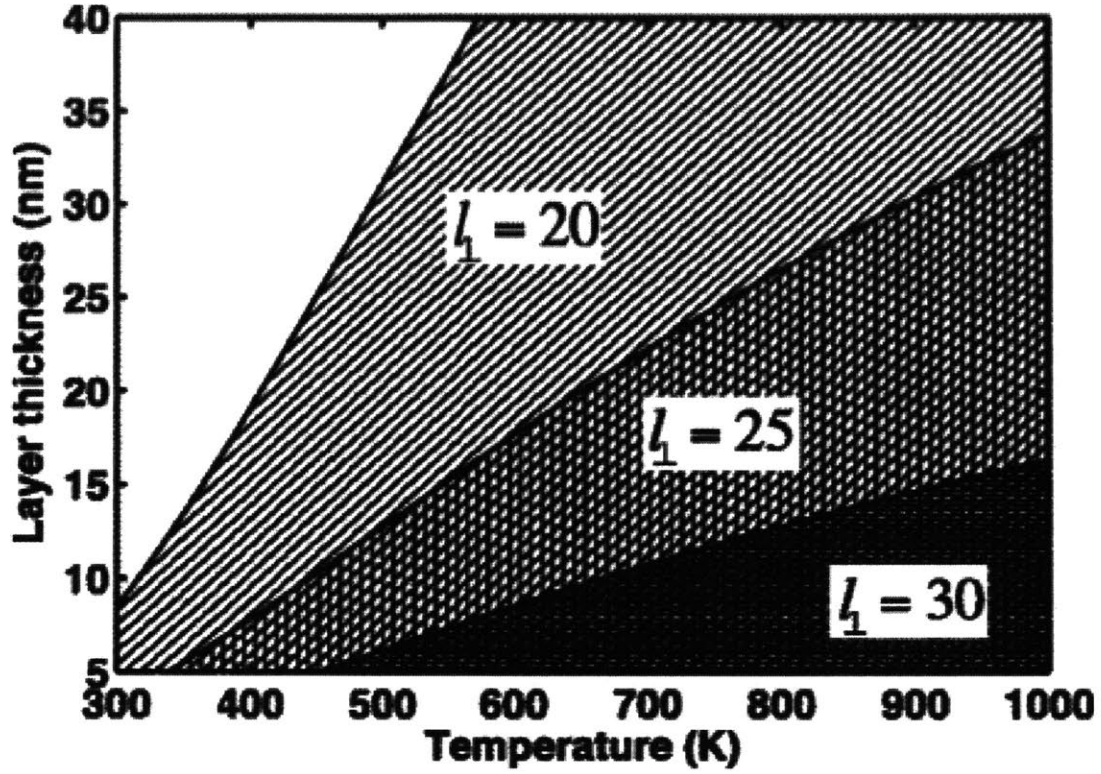
Figure 2-3: Envelopes of layer thickness and temperature where $f_{bind} < f_{bind}^{max} < 10^{-2}$ for three values of $l_\perp$: 20, 25, and 30. Changes in $l_\perp$ alter the temperatures and layer thicknesses where $f_{bind} < f_{bind}^{max} < 10^{-2}$. We impose $l_\perp$ in our design, restricting the temperature and layer thickness to the darkest cross-hatched envelope shown above.

Figure 2-4 shows envelopes of the design space that satisfy the restriction on l_{min} imposed by criterion 1 (black hatching) as well as the restriction on $l_\perp$ imposed by criteria 2 and 3 (red hatching). The intersection between these envelopes is the solution space for our design problem. Since this space is fairly extensive, we may apply additional constraints on it. One choice would be to select just those interfaces that are easily synthesized using standard processing methods. For example, physical vapor deposition (PVD) of alternating fcc and bcc metal layers yields interfaces exclusively in the Kurdjumov-Sachs orientation relation, where $\theta \approx 5.26°$ [70].

The blue vertical line in Figure 2-4 corresponds to interface synthesis via PVD. It intersects the solution envelope over two intervals: $\rho \approx 0.72 - 0.74$ and $\rho \approx 0.82 - 0.84$, as shown by green ovals in Fig. 4. Further restricting our design to pure transition metals, we find that the fcc/bcc pair Pd/Fe falls into the $\rho \approx 0.72 - 0.74$ range, while Cu/V, Pt/Nb, and Pt/Ta fall into the $\rho \approx 0.82 - 0.84$ range. While any of these metal pairs would work, since we intend to fabricate these composites for experimental validation, we impose additional constraints excluding the costly elements: Pd and Pt. This leave us with one solution: Cu/V. In this interface, $l_{min} = 6.4$ and $l_\perp = 23.3$. These values correspond to MDI spacings of $l_{min} = 2.3nm$ and $l_\perp = 23.3nm$. It's worth noting that all the FCC/BCC metal pairs listed are immiscible with each other in the solid phase. This is a necessary condition to ensure mixing does not occur between the phases and the layered material maintains it's structural integrity.

2.5 Applying FCC/BCC O-lattice calculation to HCP/BCC interfaces

We can easily adapt our solution calculated in section 2.4 to interfaces formed between the basal {1000} plane of HCP metals and the {111} plane of FCC metals. We can do this because the {1000} HCP plane has the same atomic arrangement as a {111} FCC plane. However, the FCC lattice parameter, α_{fcc} cannot simply be replaced by the the basal plane HCP lattice parameter, α_{hcp} in the O-lattice calculation. To determine the equivalent
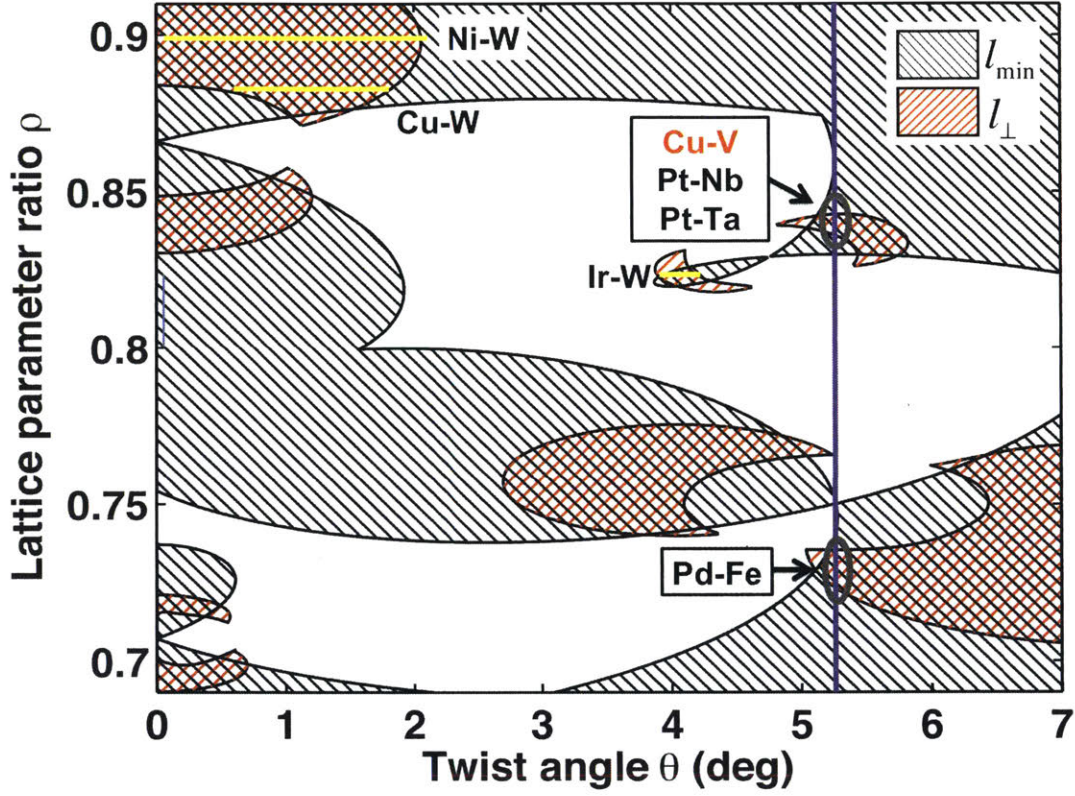
Figure 2-4: The solution space for our design problem is the intersection of envelopes satisfying the restriction on l_{min} imposed by design criterion 1 (black hatching) as well as the restriction on $l_\perp$ imposed by criteria 2 and 3 (red hatching). The vertical line at $\theta \approx 5.26°$ denotes interfaces synthesized by PVD. Ovals highlight the intersection of the solution space with this line. From the element pairs that fall into this subspace, we select Cu-V due to relatively low materials cost for validation. The horizontal yellow lines depict possible tungsten containing composites that satisfy the design criteria. However, these composites (Ni-W, Cu-W, and Ir-W) cannot be synthesized with PVD methods.

FCC lattice parameter, we must perform the following transformation to the HCP lattice parameter:

$$\alpha_{fcc} = \frac{2\alpha_{hcp}}{\sqrt{2}}$$

(2.13)

Once this calculation is done, the maps in Figure 2-2 can be read as before. For example, the HCP/BCC pair, cobalt-molybdenum (Co-Mb), satisfies the design criteria imposed in section 2.3. Cobalt, an HCP metal, has $\alpha_{hcp} = 0.25nm$ and an equivalent $\alpha_{fcc} = 0.31nm$, with a $\rho = .75$. Co-Mb satisfies the design criteria over twist angles of $\theta \approx 3 - 4°$ and $\theta \approx 6.5 - 7°$.

2.6   Comparison to experimental results

Using O-lattice theory, we predicted the MDI structure of $\{111\}FCC\|\{110\}BCC$ interfaces, and identified Cu-V as an interface with MDI spacing of interest. To validate our calculations, our collaborators at Los Alamos National Laboratory (LANL), Di Chen, Nan Li, Kevin Baldwin, Juan Wang, and Yongqiang Wang synthesized a Cu-V bilayer, implanted it with He, and imaged the interfaces post-implantation in order to observe He bubble distributions. We expect the He bubble distributions to correspond to the predicted MDI distributions.

A Cu-V bilayer film was fabricated using electron beam evaporation at elevated temperatures using copper and vanadium targets. A 150nm V layer was deposited on a MgO substrate followed by the deposition of a 150nm thick Cu layer. Once synthesized, TEM foils were made from the bilayer to perform cross-sectional and planeview TEM imaging of the interface post implantation. The samples were then implanted with 30keV He+ ions to a fluence of $5 \times 10^{15} ions/cm^2$ at $250°C$ using a 200kV Danfysuk research ion beam implanter at the Ion Beam Materials Laboratory at LANL. This energy, determined by SRIM calculations, was chosen to ensure that the peak He concentration would be located at the Cu-V interface.

Once implanted, the TEM foils were imaged. Cross-sectional TEM imaging verified

that the majority of the bubbles were on the Cu side of the interface. Planeview TEM indicated that there were three different interfacial structures influencing the precipitation patterns of the He: grain boundaries, threading dislocations, and MDIs. While the fabrication technique used to make the Cu-V bilayer was optimized for laying down large grains (grain size on the order of $.5\mu m$) of Cu and V, there were still GBs present in the sample. Helium atoms preferentially decorated the GBs, which has been observed in past He implantation experiments [56, 71]. Within the grain, the He bubbles demonstrated additional ordering behavior. It was found that the bubbles aligned themselves in high density lines that are oriented at 60° relative to each other with a preferential direction of <110> in the Cu layer. Furthermore, parallel high density bubble lines were observed to be 10, 20, or 30nm apart. This pattern and spacing is not consistent with the predicted Cu-V MDI network described in this section. Rather, the He bubbles seem to be precipitating on the trace of threading dislocations in the Cu layer. These threading dislocations form steps in the interfaces which, like the MDIs, have a higher energy and are preferential wetting locations. While these dislocations have preferential directions, namely the <110> directions that lie in the {111} slip planes of Cu, they do not have a periodic spacing or regular distribution like the MDIs [25].

Finally, our collaborators observed that some He bubbles formed a network pattern that differed from the He precipitate behavior at the GBs and on the threading dislocations. Figure 2-5 a) shows a plan view micrograph that images this aligned He pattern. Figure 2-5 b) is the magnified yellow dashed boxed shown in a). The red dashed lines highlight a group of the aligned He bubbles. The spacing between two adjacent rows was measured to be approximately 8nm. The average spacing between two bubbles within a row has been determined to be approximately 2nm. These measurements agree very will with our theoretical calculations that $l_{min} = 6.4$ and $l_\perp = 8.4$. Based on the O-lattice calculations, these MDI rows do not point in the direction of any low index crystallographic directions. The direction of the shortest spacing, is lmin, is rotated from the [11-2]FCC and [1-12]BCC directions, which are parallel in the K-S orientation, by approximately 14°. However, the directions of the MDI distributions in the TEM foil could not be confirmed.

While the experimental results demonstrated multiple interactions between interface

structures and the He bubbles, they suggest that the MDI distribution we predicted for a Cu-V interface in the K-S orientation may occur. Furthermore, this experiment implies that while the high energy steps formed by threading dislocations are irregular, they do tend to aggregate He bubbles into linear configurations. It may be possible to observe linear channels if the samples are He implanted to a higher fluence.

2.7 O-lattice summary

In the work described in Chapter 2, we applied constraints to the solution space specific to our goal of designing an interface with a particular MDI distribution that may give rise to He channel which lead to the selection of a specific Cu-V interface. While the interface we have chosen is a good candidate for experimental validation in a lab setting due to inexpensive materials cost and synthesis using a standard processing method, neither copper nor vanadium are typically considering for first-wall construction in a fusion reactor. Tungsten, however, is often considered a prime candidate due to it's high melting temperature and heat conductivity. There are quite a few FCC/BCC materials pairs containing tungsten that satisfy our constraints on l_{min} and l_{bot} as outlined in section 2.3: Cu-W, Ni-W, and Ir-W which are highlighted in yellow in Fig. 4 for a range of misorientation angles. While there are not standard methods, like PVD, that guarantee these twist angles, there are some processing methods, such as severe plastic deformation (SPD),40 that yield a narrow distribution of interfaces, rather than a single interface type. An extensive solution space, such as that in Figure 2-4, is advantageous in this context since it allows the design to remain robust, even when the processing method chosen has some intrinsic variability. The need for such robust solutions in computational materials design is widely recognized [72, 73].

Although we use interface design to approach the problem of mitigating He-induced damage, our method may be extended to other engineering problems such as managing damage induced by the precipitation of hydrogen [74] or methane [75]. The misfit dislocation structure of solid-state interfaces is also known to control mechanical properties such as dislocation emission [76], twin nucleation [77], and stability under severe deformation [78]. Interface design based on O-lattice theory is a promising approach for tailoring all

of these behaviors, providing a class of interface-related design parameters for creating materials with enhanced performance.

In the following chapters we will take our result from this section, that the MDI distribution at a Cu-V interface in the K-S orientation is a prime candidate for giving rise to linear He channels, and model He bubbles on this heterogeneous interface.
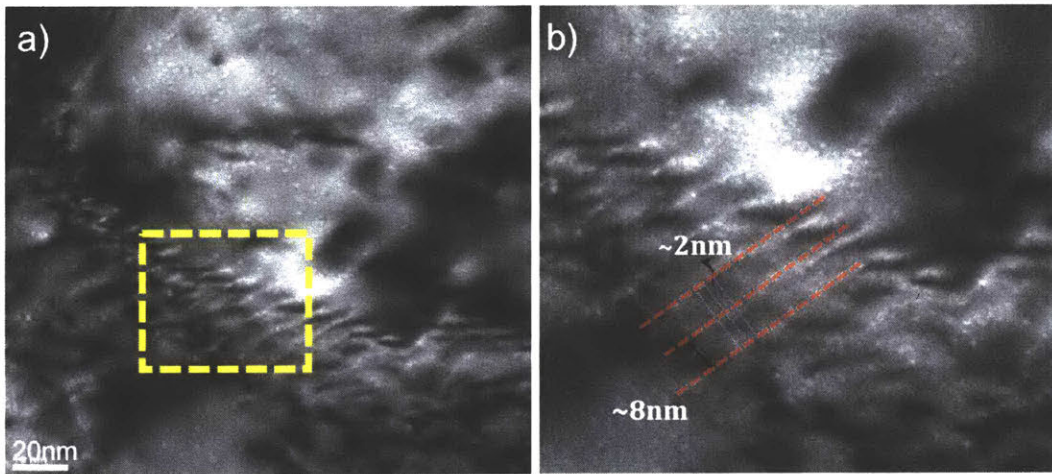
Figure 2-5: a) Planeview TEM image of He bubbles aligned on MDIs in a Cu-V K-S oriented interface. The yellow dashed box highlights the area where these He distributions are present b) The magnified image of the yellow dashed box in a). Red lines mark the aligned MDIs. The rows have an average spacing of approximately 8nm and the average spacing between bubbles is approximately 2nm. This agrees with the calculated MDI spacings from O-lattice theory of $l_{min} = 6.4$ and $l_{\perp} = 23.3$.

Chapter 3

Developing a phase field model for simulating He precipitates on heterogeneous energy interfaces

3.1 Introduction

While O-lattice allows us to predict the distribution of MDIs at an interface and thus the preferential precipitation location of He, it does not tell us how the He bubbles will interact with each other. Thus, in this chapter, we describe a phase field simulation for modeling capillarity-driven evolution of helium precipitate morphologies on solid-state interfaces with location dependent energies and, consequently, non-uniform wetting characteristics. Our approach models the metal/gas system as two immiscible components described by a single order parameter that obeys the Cahn-Hilliard equation [79, 80]. We employ a quasi-static simulation that incrementally adds precipitate to the model, driving morphology evolution. We demonstrate our method on an example problem relevant to MDI wetting: the growth and evolution of helium precipitates on a linear chain of wettable patches surrounded by non-wetting regions. Our model is a first approximation description of He precipitates in metals that is able to simulate their growth, coalescence, and stability during continuous helium loading.

51

3.2 Modeling Assumptions

Our approach to modeling helium precipitates is based on the phase field method [81]. We forego atomistic modeling because it cannot easily reach the timescales needed to capture precipitate morphology evolution [82]. Following Perryman and Goodhew [83], we assume that metal surface diffusion governs precipitate morphology evolution. We estimate that it takes individual metal atoms $\tilde{t} = \tilde{l}^2/\tilde{D} = 3 \times 10^{-7}s$ to diffuse a distance of $\tilde{l} = 10^{-8}m$ (comparable to helium precipitate dimensions [84]), given a surface self-diffusivity in Cu under vacuum of $\tilde{D} = 3 \times 10^{-10}m/s$ at 933K [85]. However, with molecular dynamics simulations, it is difficult to model times beyond several tens of nanoseconds. Thus, we carry out our simulations using continuum methods, which do not suffer from such time constraints.

We use the phase field method because it does not require explicit tracking of the interface between precipitated helium and the surrounding metal matrix. Explicit interface tracking is computationally expensive and requires an additional partial differential equation (PDE) to describe interface motion [86]. In the phase-field method, interfaces are implicitly present as regions of rapid order parameter variation in the solution of the phase field PDEs [79]. In our model, we use just one order parameter governed by the Cahn-Hilliard equation rather than using a coupled Cahn-Hilliard and Allen-Cahn equation system with two order parameters [87, 88]. This choice is adequate for capturing capillarity driven morphology evolution of the helium precipitates. Potential extensions of our model requiring more than one order parameter are presented in the section 3.5.

Helium precipitate morphologies evolve through precipitate growth, migration, and coalescence. Migration and coalescence are thought to occur via diffusion of metal atoms along precipitate surfaces [83]. The formation energies of helium defects in a metal matrix are so high that re-solution of helium from bubbles is negligibly low, averting significant Ostwald ripening [89]. Thus, helium precipitate growth usually proceeds through the diffusion of helium atoms to the precipitate and the vacancy-mediated diffusion of metal away from the precipitate [12, 13].

Our model, however, assumes that neither of these processes are rate-limiting in pre-

cipitate morphology evolution. Rather, we assume that the rate of He precipitate growth is determined directly by the rate of He generation or implantation into the material, i.e. that the addition of helium to pre-existing precipitates is a quasi-static process. Thus, we do not explicitly model the implantation of helium into the material or its subsequent diffusion through it. Rather, we assume that any implanted helium immediately makes its way to the surrounding precipitates, driving them to expand. This assumption is based on previous investigations, which found that–under typical implantation conditions [90]-the average time between arrivals of successive implanted helium atoms in the vicinity of individual precipitates is one the order of minutes. By contrast, the typical time for an implanted helium to diffuse through the metal matrix to a pre-existing precipitate is on the order of nanoseconds [34]. Thus, after an initial nucleation stage [91, 92], all implanted helium atoms are likely to be trapped at existing precipitates before encountering each other.

In some cases, e.g. during helium generation through the decay of tritium in palladium tritides [93], the concentration of helium generated may be far greater than the concentration of vacancies. In such situations, the helium-to-vacancy ratio in helium precipitates may increase well beyond unity, giving rise to additional bubble growth mechanisms, e.g. emission of interstitials [94] or prismatic dislocation loops

As mentioned in the section 3.1, our model accounts for non-uniform helium precipitation on interfaces with location-dependent energies. The current version of the model, however, considers precipitate growth exclusively on one side of the interface. This simplification is motivated by observations on heterophase interfaces, where helium precipitates preferentially grow into one of the two adjoining solids [60, 95, 84]. For example, in the case of Cu-Nb composites, interfacial helium precipitates preferentially grow into the Cu side due to the lower formation and migration energies of vacancies in Cu than in Nb as well as the lower surface energy of Cu [95, 96]. Since we are primarily interested in He behavior at a Cu-V interface, where Cu has a lower formation and migration energy of vacancies than V, the model where He only grows into one side of the interface will apply. Furthermore, as mentioned in section 2.6, when He was implanted into the Cu-V bilayer, He bubbles were found primarily on the Cu side.

53
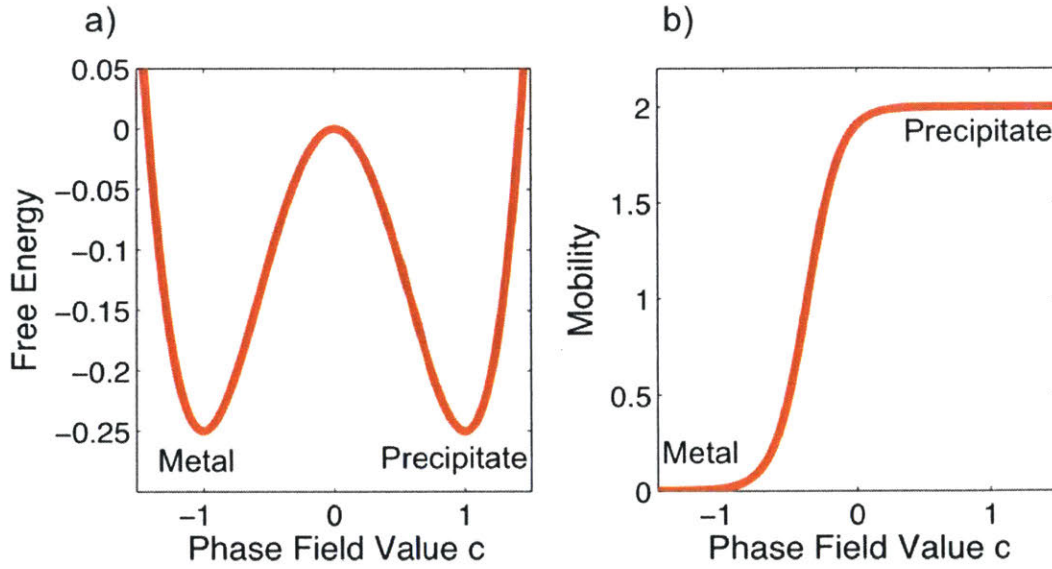
Figure 3-1: a) The free energy of the two-phase system described by our model. Minima occur at $c = -1$ (the pure metal phase) and $c = 1$ (the helium precipitate phase). b) The order parameter-dependent mobility is high in the precipitate and at the precipitate/metal interface. It is low in the metal phase

3.3 Implementation of the phase field model

The phase field method is adopted for these simulations [37, 38]. This model tracks one conserved order parameter $c(x, y, z, t)$ which is a function of both position (in three dimensions) and time. The order parameter is unitless and defined such that it takes on a value of $c = -1$ to represent a pure metal phase and $c = 1$ for a pure helium precipitate phase. The behavior of the two phases is governed by the bulk energy density [97]

$$f(c) = \frac{c^4}{4} - \frac{c^2}{2} \tag{3.1}$$

As shown in Figure 3-1.a), this energy function has minima at the pure phase values of the order parameter, i.e. $c = 1$ and $c = -1$, and a local maximum at $c = 0$. This form of energy function favors phase separation of the two phases, as required when modeling helium precipitates in metals.

The total energy of the model is

54

$$F(c) = \int_\Omega (f(c) + \frac{\epsilon}{2}|\nabla c|^2)dxdydz \qquad (3.2)$$

where Ω is the spatial domain. In addition to the bulk energy, $f(c)$, the energy functional F contains a gradient penalty term $\frac{\epsilon}{2}|\nabla c|^2$, where ϵ is a parameter that describes the magnitude of the energy penalty associated with gradients in the order parameter. Thus, decreasing ϵ leads to a sharper interface between the two phases and vice versa.

The temporal evolution of the order parameter field is described by the Cahn-Hilliard equation

$$\frac{\partial c}{\partial t} = \nabla \cdot M(c)\nabla \frac{\delta F}{\delta c} \qquad (3.3)$$

which minimizes the energy functional in Equation 3.2 while conserving the order parameter locally. In Equation 3.3, $M(c)$ is a mobility term that describes the relative diffusion of the phases. We implement a c-dependent mobility:

$$M(c) = tanh(4c + 1.5) + 1 \qquad (3.4)$$

The reason for adopting such a mobility function is to separate the time scale of precipitate morphology evolution from the time scale of Ostwald ripening by making it difficult for small quantities of dissolved precipitate to migrate through the metal. A similar outcome may be achieved by adjusting the depth of the energy wells in Equation3.1 and the gradient penalty parameter ϵ, so as to decrease the interface thickness between the two phases while maintaining a constant interface energy. However, decreasing the interface thickness necessitates the use of a finer mesh when solving Equation 3.3, thereby increasing the computational expense of the model. The c-dependent mobility function in Equation 3.4 reduces the coarsening rate while allowing us to use a thicker interface width and therefore a coarser (and computationally less expensive) mesh.

To confirm the equivalence of simulations performed using thinner interfaces to ones that use c-dependent mobilities, we simulated Ostwald ripening of two unequal sized precipitates in two dimensions. All the simulations had identical interface energies. When using the c-dependent mobility given by Equation 3.4, we do not observe Ostwald ripening

55

at any interface thicknesses. When using a c-independent mobility, Ostwald ripening does occur, but its rate decreases as the interface thickness decreases. Thus, with a sufficiently fine interface, an arbitrarily low rate of ripening may be achieved. The drawback to using sharp interfaces is that a much finer mesh is required in the interface region, negating the advantages of the phase field method described in section 3.2. Thus, to ensure computational efficiency, we adopt a concentration-dependent mobility.

To describe the location-dependent energy of the interface, we define different boundary conditions on wetting and non-wetting interface regions. The relation between interface energy and wettability is described by equation 1.2: where W defines the excess interface wetting energy, and the relevent interface energies (γ_{AB}, γ_{AHe} and γ_{BHe} are illustrated in Figure 3-2.

When $W > 0$, there is a driving force for helium precipitates to wet the interface at an angle, ϕ, determined by Young's equation:

$$\gamma_{AB} = \gamma_{BHe} + \gamma_{AHe}cos(\phi). \tag{3.5}$$

This relation may be derived by considering the above mentioned interface energies as tensions tangent to the corresponding interfaces and normal to the line of contact between them. Requiring the horizontal component of these tensions to balance yields Equation 3.5. Note that, while γ_{BHe} and γ_{AB} are always horizontally aligned, the direction of γ_{AHe} changes with the wetting angle. When $W = 0$, $\phi = 180°$ and γ_{AHe} points in the same direction as γ_{AB}(antiparallel to γ_{BHe}). When $W < 0$, there is a thermodynamic driving force for complete de-wetting of helium from the interface because γ_{BHe} is larger than the sum of γ_{AB} and γ_{AHe}. When $(\gamma_{AB} - \gamma_{BHe})/\gamma_{AHe} \geq 1$, spreading occurs: the precipitate wets the interface with a contact angle of 0° [63].

We apply a Dirichlet-type boundary condition to model the low energy, non-wetting regions, enforcing that there is only metal phase at these locations on the interface:

$$c(x, y, z, t) = -1 \tag{3.6}$$

To describe a wettable region on the interface, we apply Neumann conditions following the

56

approach of Yue and Feng [98]:

$$\epsilon \hat{n} \cdot \nabla c = -\frac{\partial f_w(c)}{\partial c}.$$ (3.7)

This boundary condition fixes the contact angle, ϕ, between the precipitate/metal interface and the wetting region. Here, f_w is the boundary energy,

$$f_w(c) = -\gamma_{AHe}cos(\phi)\frac{c(3-c^2)}{4} + \frac{\gamma_{BHe} + \gamma_{AB}}{2}$$ (3.8)

This energy is solely a function of the order parameter immediately adjacent to the boundary. When the wetting angle is $\phi = 90°$, the wall energy depends only on γ_{BHe} and γ_{AB}. The energy γ_{AHe} is related to the field equations through [99]

$$\gamma_{AHe} = \frac{2\sqrt{2}}{3}\frac{\epsilon}{\lambda}$$ (3.9)

where λ is the interface thickness computed from $\epsilon = 4\lambda^2 \Delta f$. Here, ϵ is the gradient penalty coefficient and Δf is the depth of the well energy of $f(c)$. In our calculation, $\Delta f = .25$.

Substituting Equations 3.8 and 3.9 into Equation 3.8, we obtain an expression for the boundary conditions on wettable regions that only includes the phase-field variable c, gradient energy penalty ϵ, and contact angle ϕ:

$$\hat{n} \cdot \nabla c = \sqrt{2/\epsilon}\,cos(\phi)(1 - c^2)$$ (3.10)

Because the Cahn-Hilliard equation is a fourth order PDE, we require two sets of boundary conditions on each boundary. On boundaries that do not model interfaces, as described above, we set a no-flux condition on c:

$$\epsilon \hat{n} \cdot \nabla c = 0$$ (3.11)

This corresponds to a wetting angle of $\phi = 90°$ in Equation 3.10. However, we do not expect any of the helium precipitate to interact with these boundaries in the simulations to be presented here.

In addition to the boundary condition on c, we also set a condition on the chemical

57
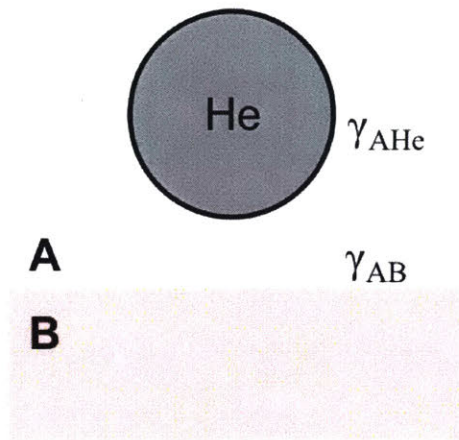
a) No wetting: W<0   b) Wetting: W>0
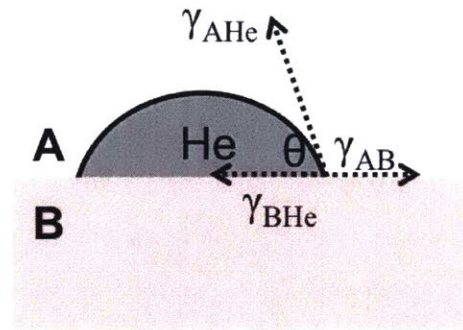
Figure 3-2: a) No wetting occurs when W, the excess interface wetting energy, is less than 0. b) Wetting does occur when W is greater than 0. The arrows indicate the directions of interface tensions used to derive Youngs relation in Equation 3.5. γ_{AB} is the location-dependent energy of the interface between elements A and B, γ_{AHe} is the interface energy between helium and element A, into which the helium precipitates grow, and γ_{BHe} is the interface energy between helium and element B.

potential, defined as $\omega = c^3 - c - \epsilon \nabla c^2$:

$$M\hat{n} \cdot \nabla \omega = 0 \qquad\qquad (3.12)$$

This no-flux condition on ω ensures that there is no order parameter inflow or outflow from the simulation cell. Any change in the net phase field value arises from the explicit modifications described below.

We introduce a net increase in the helium precipitate phase into our model following the quasistatic assumptions outlined in section 3.2. Thus, our simulations do not model precipitate nucleation. Instead, precipitate nuclei are created explicitly by specifying their shape, size, and location in our initial condition. We place the precipitates on interface regions wettable by helium. Next, we relax our model by evolving the order parameter field following the Cahn-Hilliard equation. We consider the model to have reached equilibrium once the time derivative $\frac{\partial c}{\partial t}$ at every location has fallen below the threshold of 10^{-3}. While true equilibrium occurs when $\frac{\partial c}{\partial t} = 0$, we find that at $\frac{\partial c}{\partial t} = 10^{-3}$ the precipitate morphology evolution is negligible compared to the initial time steps of the simulation (where $\frac{\partial c}{\partial t} \approx 1$) and that the total energy has plateaued.

Starting from a well-relaxed state (indexed by subscript n), we add precipitate to the model by performing the following transformation on the entire scalar field $c_n(x, y, z, t)$ to obtain $c_{n+1}(x, y, z, t)$:

$$c_{n+1}(x, y, z, t) = (1 + g_n)(c_n(x, y, z, t) + 1) - 1 \qquad\qquad (3.13)$$

This loading operation increases the value of the order parameter in the precipitate phase from $c(x, y, z, t) = 1$ to $c(x, y, z, t) = (2g_n + 1)$, where g_n is a growth factor. The loading modifies the net order parameter, but this change is localized to the precipitates. Thus, when the order parameter field redistributes to reach equilibrium, it does so in a way that enlarges pre-existing precipitates, rather than nucleating new ones. The operation in Equation 3.13 does not change the order parameter value in the metal, where $c = -1$. We relax the model with initial condition $c_{n+1}(x, y, z, t)$, causing the non-equilibrium precipitates to expand and the phase field value inside them to once again approach $c = 1$. The evolution of the

59

precipitate morphology–including any precipitate coalescence or de-wetting events–occurs during this relaxation.

Figure 3-3 illustrates a single growth step of an isolated precipitate at an interface with uniform wetting angle. In Figure 3-3.a), the metal and precipitate are in equilibrium and the initial precipitate volume is V_i. We then carry out the operation in Equation 3.13 using $g_n = 1.5$, thus changing the order parameter value in the precipitate to $c(x, y, z, t) = 4$. We choose such a large g_n value for demonstration only. Our precipitate growth simulations typically use much smaller values to approximate continuous precipitate growth. The color change of the precipitate from Figure3-3.a) to Figure 3-3.b) demonstrates the change in phase field parameter value inside the precipitate. We then relax the model, obtaining the configuration in Figure 3-3.c). We see that the precipitate volume has increased from V_i with an order parameter value of $c(x, y, z, t) = (2g_n + 1)$ to a final precipitate volume of $V_f = V_i \times (g_n + 1)$ with an order parameter value of $c(x, y, z, t) = 1$. The factor of two multiplying g_n in the expression for V_i arises from the fact that the difference in order parameter between the two equilibrium phases is two.

The sequence of steps described above may be repeated iteratively until we have added the desired amount of precipitate to the model. To ensure that a constant amount of precipitate is added in each iteration, n, we specify the following value for g_n:

$$g_n = \frac{1 + f_{grow} \times n}{1 + f_{grow} \times (n - 1)} - 1 \tag{3.14}$$

Here, f_{grow} is the fraction of the initial precipitate phase volume we wish to add in each step. In our simulations, we typically use $f_{grow} = 0.2$. The outcome of these operations is a series of equilibrium states with differing precipitate morphologies and linearly increasing precipitate volume. We implement these simulations in the Multiphysics Object-Oriented Simulation Environment (MOOSE): a finite element multiphysics modeling framework [100].
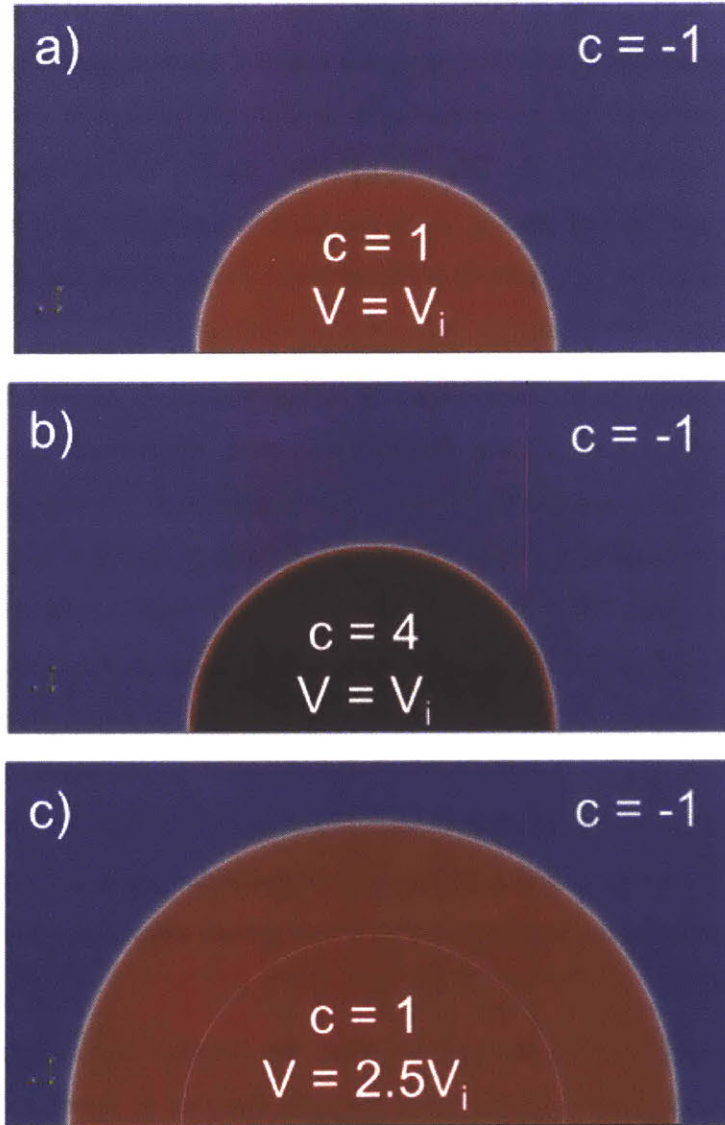
Figure 3-3: A cross section through a hemispherical precipitate wetting an interface. Blue and red represent metal and precipitate phases in equilibrium, respectively. a) Initial state with precipitate volume V_i. b) The order parameter value inside the precipitate is increased to $c = 4$. The color change of the precipitate indicates the precipitate phase is no longer in equilibrium. c) After relaxation, the precipitate grows from its initial volume, V_i, to $V_f = 2.5V_i$ and the phase field value inside it returns to equilibrium.

3.4 Application to a model problem

As a demonstration and a way of validating our model, we apply the method described in section 3.3 to a model interface containing a linear chain of circular, wettable patches. This is a small scale simulation that represents a component of a network of wetting MDIs at an interface. We are modeling the MDIs as perfectly circular wetting regions. Running this small scale problem will show us if our model demonstrates the properties we have built in: heterogeneous wetting, growth of He bubbles, and He bubble coalescence through capillarity driven morphology change rather than Ostwald ripening.

Figure 3-4.a) shows the model geometry to be investigated. It consists of six circular wettable regions surrounded by a non-wetting background. On each of these patches, we place a hemispherical helium bubble with the same diameter as the wetting patch, depicted in Figure 3-4.b). We model the growth of these precipitates as described in section 3.3 for a range of wetting angles [$30°$, $40°$, $60°$, $80°$, $100°$, $120°$] and wetting patch spacings [6.3λ, 9.4λ, 12.5λ, 15.6λ, 18.7λ, 21.8λ]. We express all lengths in our model as multiples of the metal/precipitate interface thickness, λ. We choose the value for ϵ such that the interface thickness is 50 times smaller than the wetting patch diameter, approximating an atomically sharp interface if the patches are of nanometer dimensions [101]. The total cell size is 500 $\times$ 190 $\times$ 140λ. We use f_{grow} = 0.2, adding 20% of the initial precipitate volume in each simulation step. We stop the simulations after fifteen growth steps (300% increase in total precipitate volume).

Each simulation has a total of 15 growth steps. We initialize the simulation by covering each wetting patch with a He bubble of the same diameter as shown in Figure 3-5.a) Typically, in steps 1 through 8, the precipitates grow uniformly in size, as shown in Figure 3-5.b). Around step 9 or 10, the precipitates begin to interact, as shown in Figure 3-5.c). By step 10 or 11, they coalesce with each other. Thus, the coalescence process usually only takes one or two steps to complete. Figure 3-5.d) depicts the the precipitate morphology after the coalescence process is complete. After this coalescence event, the precipitate morphology maintains the same general shape while growing uniformly larger for several subsequent loading steps, as depicted in Figure 3-5.e).
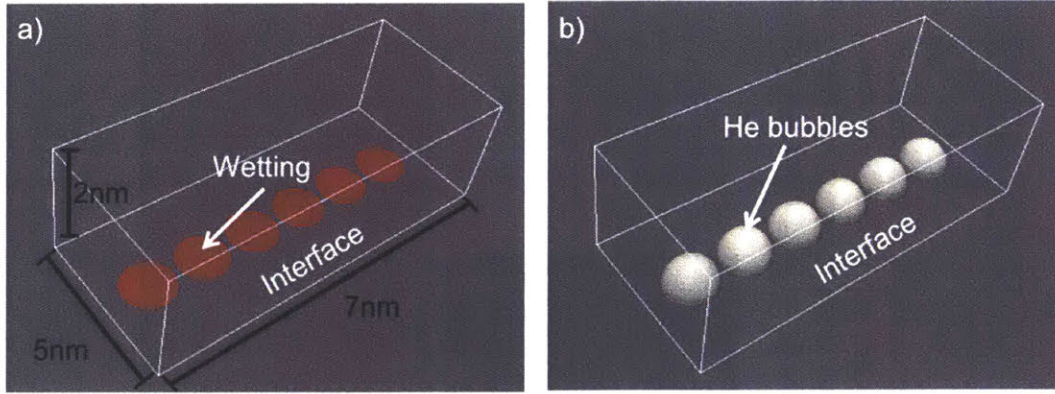
Figure 3-4: a) The simulation cell for the model problem described in section 3.4. The red circles are wetting regions while the surrounding interface area is non-wetting. b) Initial precipitate morphology with a helium bubble covering each wettable patch. This figure shows the isosurface with order parameter c=0, corresponding to the midpoint of the metal/precipitate interface.

We classify the final precipitate morphologies obtained from our simulations into four categories. The first morphology is a continuous linear precipitate channel, as illustrated in Figure 3-6.a). In it, all of the helium forms a single precipitate that fully covers all the wettable patches. We find three combinations of wetting angles and patch spacings that give rise to this morphology: $[30°, 12.5\lambda]$, $[30°, 15.6\lambda]$, and $[40°, 15.6\lambda]$. In the second morphology, all wettable patches are fully covered by helium precipitates, but more than one helium precipitate is formed. This morphology was observed over a range of low contact angles and for all patch spacings, as summarized in Table 3.1. Figure 3-6.b) depicts an example of this morphology.

The third morphology involves partial de-wetting of one or more patches, in addition to the presence of multiple precipitates, as demonstrated in Figure 3-6.c). The final morphology is typified by full de-wetting of one or more patches as shown in Figure 3-6.d). The third and fourth morphology types both occur for all patch spacings, but larger contact angles than the first two morphologies. Table 3.1 gives the combinations of patch spacings and contact angles at which we observed all four morphologies.

Table 3.1 shows that coalescence of precipitates into low aspect ratio, approximately spherical bubbles occurs for larger contact angles regardless of patch spacing, while smaller wetting angles result in extended precipitate formations with higher aspect ratios. All of
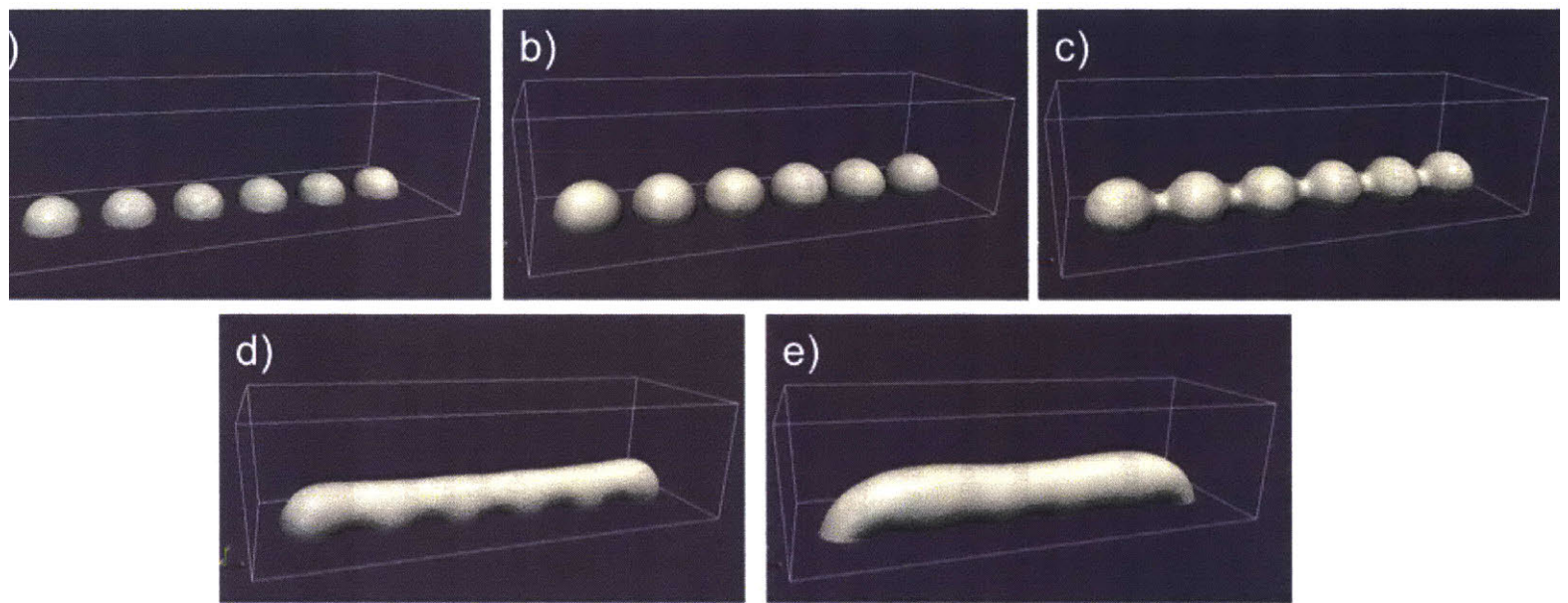
Figure 3-5: Isosurfaces of the typical progression of our example simulations: a) Initialization: each wetting patch is covered with a precipitate of equal diameter, which relaxes to the designated wetting angle. b) The precipitates become larger, but do not interact. c) Precipitates interact and begin to coalesce. d) The coalesced precipitates reach an equilibrium configuration. All coalescence or wetting processes typically take place in 1 or 2 simulation steps. e) The precipitate grows uniformly as more precipitate phase is added.
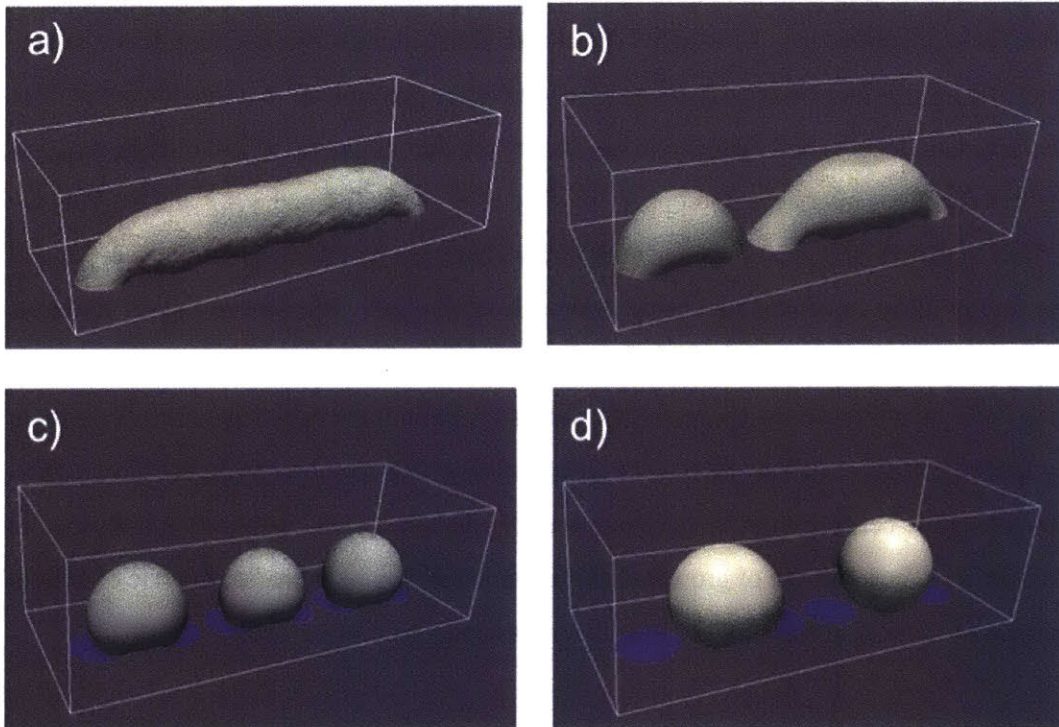
Figure 3-6: Isosurfaces of the four final precipitate morphologies observed in our model problem: a) a single extended precipitate covering all wetttable patches fully, b) all wettable patches are fully covered, but there are several distinct precipitates, c) one or more wettable patches are partially de-wettted, and d) one or more wettable patches are fully de-wetted.

these final morphologies likely represent metastable configurations corresponding to local energy minima, as opposed to stable configurations in global energy minima. For example, it seems unlikely that the global energy state for the parameter combination of 30° and 6.3λ consists of multiple precipitates while the global energy state for the parameter combination of 30° and 12.5λ results in a linear channel. In both cases, the trajectory of bubble coalescence events may lead to configurations trapped in local, metastable energy minima.

Our model is formulated entirely in terms of dimensionless lengths and energies. However, these quantities may be mapped directly to physical units by matching them to characteristic lengths and energies corresponding to helium precipitates in a specific metal. The characteristic lengths and energies in our model are the thickness, λ, and energy, γ_{AHe}, of the metal/helium interface. In copper (A=Cu), $\lambda = .4 \times 10^{-9}$ and $\gamma_{AHe} = 1.93$.This interface thickness is typical for interfaces formed between metals and liquid/gas [102] and the energy value was calculated using molecular statics [60]. The dimensionless thickness and energy of interfaces in our model are ~ 0.32 and ~ 0.29, respectively. Thus, we may map these quantities to the characteristic values for helium in copper by multiplying them by factors of 1.25×10^{-9}m and $6.6 J/m^2$, respectively. Our simulations do not have a characteristic time because they are carried out under the quasi-static assumption described in section 3.2. Thus, the rate of growth of the precipitates may be related to the rate of helium generation or implantation, rather than to any material-specific parameter.

3.5 Phase-field model discussion

We have developed a phase-field model for simulating the growth, coalescence, and stability of helium precipitates on patterned interfaces. This method accounts for the quasi-static addition of helium to the precipitates and captures the subsequent morphology changes of the precipitate network. We demonstrated this method on a linear configuration of six circular wetting MDIs surrounded by non-wetting area and found that lower contact angles generally resulted in elongated precipitates while larger contact angles resulted in more equiaxed formations. We will apply this method on helium precipitation on interfaces with

Table 3.1: Final morphologies observed for each angle and wettable patch spacing combination investigated.

	30°	40°	60°	80°	100°	120°
6.3λ	■	■	○	○	○	○
9.4λ	■	■	■	○	○	△
12.5λ	◆	■	■	△	○	○
15.6λ	◆	◆	■	△	○	○
18.7λ	■	■	■	■	△	○
21.8λ	■	■	■	△	△	○

◆ No de-wetting of MDIs, single precipitate (Fig. 3-6.a))

■ No de-wetting of MDIs, multiple precipitates (Fig. 3-6.b))

△ One or more MDIs partially de-wetted (Fig. 3-6.c))

○ One or more MDIs fully de-wetted (Fig. 3-6.d))

Cu-V distributions, linear wetting regions, and models containing more than one wettable interface in Chapters 4 and 5.

The method presented here models several essential mechanisms of helium precipitate morphology evolution at interfaces with location-dependent energies. However, due to its simplicity, there are phenomena it cannot capture. For instance, our method only considers a single order parameter and therefore cannot track the state of helium inside precipitates. Introducing a second order parameter would allow us to track quantities such as the density of helium in precipitates, which is essential for computing helium pressure and therefore for modeling osmotically driven instabilities such as the bubble-to-void transition [103, 104]. Similarly, in the interest of conserving computational resources, we did not couple our phase field equation to hydrodynamic models of helium flow within precipitates [105]. Adding hydrodynamics to the model may be helpful in simulations of outgassing: the removal of helium by flow through precipitate networks.

Our model uses the quasistatic assumption described in section 3.2. However, there are circumstances where accounting explicitly for the mechanisms of helium and vacancy transport to precipitates may become important [106], e.g. in applications characterized by very high helium implantation rates [67]. These mechanisms are likely to be affected by the distribution of crystal defects, such as vacancies, interstitials, or dislocations.

Our model does not consider elasticity of the metal phase. Introducing elasticity may be important whenever precipitates are under- or over-pressurized with respect to the capillary pressure of the precipitate/matrix surface. Our model also does not account for the anisotropy of surface energies, which may lead to the formation of faceted bubbles under some circumstances [107]. Finally, the present implementation of our model considers precipitation on only one side of a heterophase interface. Relaxing this restriction would require the introduction of an additional order parameter to describe the adjacent crystal phases. Despite these shortcomings, our model is successful as a first-order description for predicting helium precipitate morphologies on heterophase interfaces with location-dependent wetting characteristics.

The model described here is sufficiently generic that it may be applied to capillarity-driven morphology evolution in other material systems, besides He in metals. For example,

in nickel-based alloys in pressurized water reactors, carbon can react with hydrogen to form methane gas, which then precipitates out into small bubbles on grain boundaries [75]. These methane bubbles have been observed to accelerate cracking when they grow together and coalesce. Our model may provide a good first-order description of this phenomenon.

Chapter 4

Applying a phase-field model to He precipitation at a Cu-V interface

4.1 Introduction

In this chapter we combine the work from Chapter 2 and Chapter 3 to model the precipitation, growth, and coalescence of He bubbles at Cu-V interfaces. The Cu-V MDI distribution calculated in Chapter 2 informs the wetting MDI distribution we use for our simulation [108]. The phase field model described in Chapter 3 governs the temporal and spatial evolution of the He bubble system [109]. We describe the simulation set up and results for a single Cu-V interface, like that found in a Cu-V bilayer, and for two adjacent Cu-V interfaces, like those found in a Cu-V trilayer. The goal of this work is to observe the behavior of He bubbles at Cu-V interfaces. We find that linear channels form at a single Cu-V interface.

4.2 He wetting of a single Cu-V interface

4.2.1 Simulation set up for a single Cu-V interface

To understand the He behavior at a Cu-V interface, we set up a simulation of 40 MDIs that are spaced according the MDI distribution described in Section 2.4: The minimum spacing

between MDIs is: $l_{min} = 6.4 = 2.3nm$ and $l_\perp = 23.3 = 8.4nm$ [108]. The setup of our simulation cell is shown in Fig. 4-1.a). Assuming the MDI spacing sets the length scale, the size of the simulation cell is 33.6nm x 23nm x 5nm. The red circular regions represent the high energy MDI wetting regions while the rest of the interface is non-wetting. We apply periodic boundary conditions in the x and y directions. To the upper boundary in the z-direction we apply a no-flux Neumann condition. However, we do not grow the precipitate large enough such that it interacts with the upper boundary.

In the previous chapter when we developed the phase field model, we modeled He precipitate behavior for a range of wetting angles. In this simulation, the wetting angle is a function of three quantities as defined by Eqn. 3.5: the position dependent energy between the copper and the vanadium, γ_{CuV}, the energy between the copper and the helium, γ_{CuHe}, and finally the energy between the vanadium and the helium, γ_{VHe}. To determine the position dependent values of γ_{CuV}, an algorithm has been developed by Sanket Navale of the Demkowicz group. The first step is to construct a Cu-V bilayer in LAMMPS [110] or a similar molecular dynamics (MD) program. Once the system is relaxed (the potential energy is minimized), the energy value of each atom is extracted. A cylinder is drawn through the Cu-V interface with one end terminating in the center of the copper layer and the other end terminating in the center of the vanadium layer. The following summation is then performed over the all of the atoms within the cylinder to determine the surface energy contained within the cylinder:

$$\gamma_{CuV} = \frac{1}{A} \sum_{i=1}^{n_{atoms}} E_i - n_{Cu}E_{Cu}^{coh.} - n_V E_V^{coh.} \tag{4.1}$$

where A is the area of the interface within the cylinder (also the area of the end caps of the cylinder), E_i is the energy of each individual atom, n_{Cu} and n_V are the number of copper and vanadium atoms within the cylinder, respectively, and $E_{Cu}^{coh.}$ and $E_V^{coh.}$ are the cohesive energies for copper and vanadium, respectively. The cylinder is moved to a new area of the interface and the calculation is repeated to find the interface energy. This is repeated until an energy value has been found for each region of the interface. The diameter of the base of the cylinder should be large enough that enough atoms are used in the calculation, but
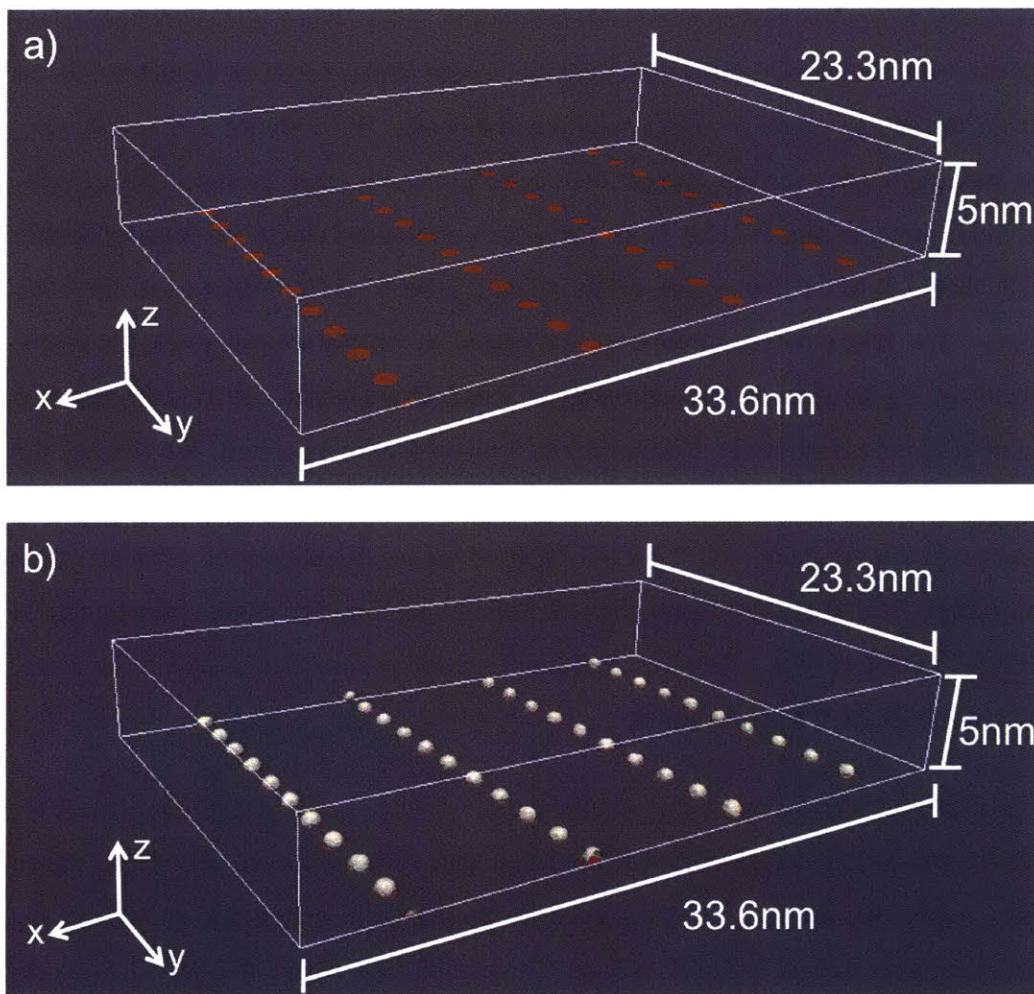
Figure 4-1: a) The simulation cell for a single Cu-V described in section 4.2.1. The red circles are wetting regions while the surrounding interface area is non-wetting. Periodic boundary conditions are applied in the x and y directions b) Initial precipitate morphology with a helium bubble covering each wettable patch. This figure shows the isosurface with order parameter c=0.

small enough to capture the interface energy variations, typically on the order of a lattice parameter: $\sim 5\text{Å}$.

However, to our knowledge, no reliable interatomic potential between copper and vanadium has been developed from which the γ_{CuV} energy values could be extracted. As an estimate, the energy values for γ_{CuNb} system will be used. This estimate is reasonable because Nb and V have surface energies within 10% of each other for the {100}, {110}, and {111} family of planes [111, 112]. From the calculations on Cu-Nb done by Sanket Navale, the γ_{CuNb} of the high energy MDIs is found to be $\sim 1.5 J/m^2$ and we use this value for γ_{CuV}. The values for γ_{CuHe} and γ_{VHe} are related to the surface energy for Cu and V respectively. Again, since the surface energy of V and Nb are similar, we used the value for $\gamma_{NbHe} = 2.4 J/m^2$ calculated by Kashinath and Demkowicz for γ_{VHe} [60]. We also use the value $\gamma_{CuHe} = 1.93 J/m^2$ [60] calculated using molecular dynamics. Using these values, we estimate a wetting angle of $\sim 115°$ for the MDIs. If we see linear channels forming at this wetting angle, it is likely that linear channels would also form for smaller wetting angles in this MDI configuration. However, additional simulations may be needed if the actual wetting angle of Cu-V MDIs is larger.

In this simulation, we initialize the simulation with a He bubble at each MDI as shown in Fig. 4-1.b. We set $f_{grow} = 0.4$, a quantity described in section 3.3, so 40% of the initial precipitate volume is added with each simulation step. While this growth rate may seem large, we choose a value that will give us a relatively quick increase in precipitate volume, while still small enough to use the quasi-static assumptions outlined in section 3.2. Initially the He bubbles are too far away to interact with each other, so even large increases in precipitate size will not effect the simulation outcome– the bubbles grow uniformly larger. Once the bubbles are large enough to interact with each other (around a volume 20 times larger than the initial precipitate volume), while we are still adding 40% of the initial precipitate volume, this corresponds to adding only $\sim 2.4\%$ of the precipitate volume at step 50.

74

4.2.2 Results and analysis: He precipitate formation at a single Cu-V interface

We repeated the growing algorithm for until we had approximately 45 times times the initial precipitate volume in our system. A perspective view and a top down view of the $\phi = 0$ isosurface is shown in figure 4-2.a) and figure 4-2.b) respectively. Qualitatively, we observe the formation of elongated linear channels. One of the channels spans the entire length of the simulation cell (10 MDIs), while other channels are shorter, spanning anywhere from 3- 6 MDIs. We also observe a solitary spherical cap precipitate that has not yet coalesced with the other He precipitates. To quantify the results of the Cu-V simulations, we extract three quantities from the individual simulation steps: the total precipitate volume, the total surface area of the precipitate, and the interfacial area wetting by the precipitate.

To determine the precipitate volume, we first consider the initial conditions. Here we set the initial number and size of the He precipitates thus setting the total initial precipitate volume equal to $V_i^{He} = 40 \cdot \frac{1}{2} \cdot \frac{4}{3}\pi r^3$. There are 40 total hemispheres. While the equilibrium wetting angle is not 90° for the Cu-V simulations, we initialize hemispheres and in the first simulation step. The precipitates then relax to their equilibrium wetting angle of 115° in the first simulation step. The radius, in this simulation is initialized to r=.5. To determine the precipitate volume of subsequent simulation steps, the integral of the phase field parameter, c, over the entire simulation cell is calculated for each step:

$$C_{total} = \int_{\Omega} c \, d\Omega \qquad (4.2)$$

To determine how much precipitate was added between subsequent simulation steps, the difference between consecutive steps is computed and divided by 2:

$$\Delta V_n = \frac{1}{2}(C_{n+1} - C_n) \qquad (4.3)$$

Where ΔV_n is the change in He precipitate between simulation steps n and n+1. The factor of 2 is result of there being a difference of 2 between the equilibrium values of the precipitate phase ($c = 1$) and the metal phase ($c = -1$). Thus the total volume, V_n^{He}, of precipitate

75
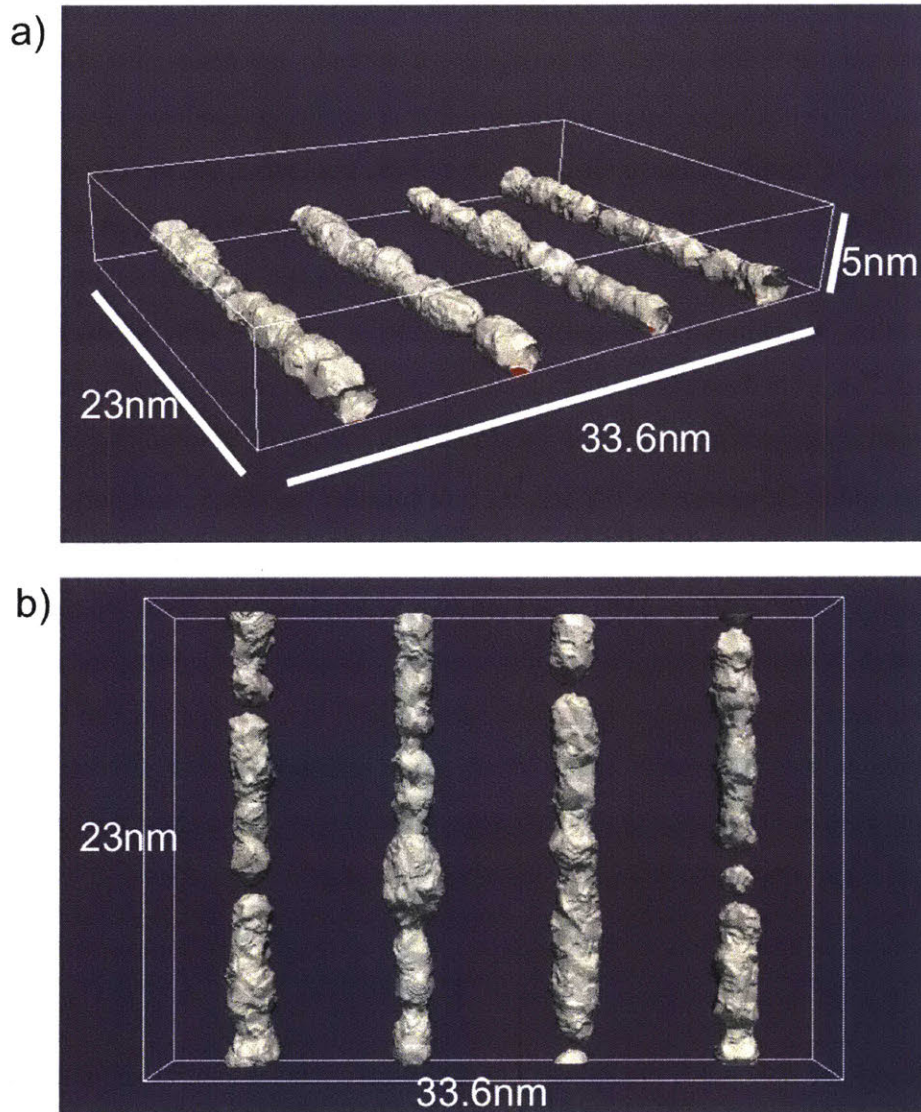
Figure 4-2: a) A perspective view of the c=0 isosurface of He precipitates at a Cu-V interface patterned with MDIs. b) A top down view of the c=0 isosurface of He precipitates at a Cu-V interface patterned with MDIs. Stable linear precipitate channels do form.

at any step is:

$$V_n^{He} = V_i^{He} + \sum_{n=2}^{n} \Delta V_n \qquad (4.4)$$

Since the amount of precipitate added in each step is controlled through the setting of f_{grow}, we can also track the number of steps to determine the precipitate volume. We find that both methods yield nearly identical results.

To extract the surface area, the following calculation is first performed on the entire phase field to calculate the total interfacial energy of each simulation step at equilibrium [79]:

$$\Gamma_{He} = \int_{\Omega} f(c) - f(c_0) + \frac{\epsilon}{2}|\nabla c|^2 d\Omega \qquad (4.5)$$

It is insufficient just to calculate the integral of the gradient energy as it only counts for part of the interfacial energy. f(c) is the bulk equilibrium free energy density as defined by Eqn.3.1 and f(c_0) is the bulk equilibrium free energy density as a function of composition defined by the common tangent line for the binary system. In this case, since both phases have the same energy, the value of f(c_0)=-0.25 for all compositions.

Since we are interested in the total surface area rather than the total surface energy, we must divide Eqn. 4.5 by the energy per unit surface area, γ for each simulation step. To calculate γ, we divide the initial total surface energy Γ_i^{He} by the initial total surface area SA_i^{He} at the end of the first simulation step when each precipitate system has relaxed to its equilibrium angle. We calculate the initial total surface area from the initial volume, V_i^{He} and the wetting angle, $\phi \sim 115°$. First, using the initial volume, the radius of a spherical cap with wetting angle of ϕ is calculated:

$$V_i^{He} = \frac{\pi r^3}{3}(cos(\phi) + 2)(cos(\phi) - 1)^2 \qquad (4.6)$$

Thus,

$$r = (\frac{3V_i^{He}}{\pi(cos(\phi) + 2)(cos(\phi) - 1)^2})^{\frac{1}{3}} \qquad (4.7)$$

77

Using the expression above for r, we can calculate the initial surface area of the precipitates:

$$SA_i^{He} = 2\pi r^2 (1 - cos(\phi)) \tag{4.8}$$

This can be done because at this point in the simulation, the precipitates are nearly perfect spherical caps and no interaction between precipitates has occurred. Furthermore, the size of the spherical caps has not yet exceeded the wetting area of the MDIs, so the equilibrium wetting angle holds.

Now γ can be calculated, by dividing the initial total surface energy by the initial surface area. This calculated γ value, can be used to normalize the total surface energy Γ_n^{He} for all simulation steps, as γ does not vary between simulation steps. The value for γ will change depending on the form of the bulk free energy density expression and the value of the gradient energy penalty. Thus the surface area, SA_n^{He} can be determined for all simulation steps.

The last quantity calculated is the interfacial area wetted by the precipitate, IA^{He}. To do this calculation, the following surface integral is performed on exclusively the wetting boundaries of the simulation cell for each simulation step:

$$IA^{He} = \frac{1}{2} \int_A (c + 1) dA \tag{4.9}$$

In addition to calculating the precipitate volume, surface area, and wetting interface area for the Cu-V case, reference cases were computed as a means of comparison. Two reference cases were considered for a single Cu-V interface: 40 spherical caps and 4 horizontal cylindrical segments on a uniform wetting surface. Given some precipitate volume, the total surface area and corresponding wetted interface area of 40 spherical caps with the same total volume was calculated, assuming a wetting angle of $\phi = 115°$. Then, for the same precipitate volume, the total surface area and wetted interface area of 4 horizontal cylindrical segments was calculated, assuming the length of each segment was fixed to the width of the simulation cell (23nm) and the wetting angle is $\phi = 115°$.

For a given precipitate volume, the surface area and wetted interface area of the precipitates on a Cu-V interfaces were compared to the reference cases described as shown

78

in figure 4-3. Figure 4-3.a) shows the precipitate surface area as a function of normalized precipitate volume. The precipitate volume has been normalized by the initial precipitate volume, V_i. The black dots correspond to the Cu-V data while the dashed red line represents the hemispherical cap reference case and the dashed blue line represents the horizontal cylindrical segment reference case.

For small normalized precipitate volumes, the Cu-V data closely follows the spherical cap reference case. This reflects the precipitates growing on the MDIs and not interacting with neighboring precipitates. A deviation from the 40 spherical cap case occurs around a normalized precipitate volume of 20. At this point, two precipitates at neighboring MDIs interact and coalesce with each other. As the precipitates continue to grow and interact, the surface area of the precipitates deviates from the 40 hemispherical cap reference case and more closely follows the 4 horizontal cylindrical segments reference case.

Figure 4-3.b) depicts the wetted interface area of the precipitates as a function of normalized precipitate volume. For both reference cases, the wetted interface area rapidly increases with increasing precipitate volume. For the Cu-V data, however, there is a steep increase in the wetted area up to a normalized precipitate volume of around 4 before leveling off. At this point, the He precipitates have completely saturated the MDI area and cannot wet any more of the interface. Thus as the precipitates grow, they are no longer at their equilibrium angle set by the Neumann boundary conditions.

Based off of the simulations of He precipitates at a single Cu-V interface, we can conclude that having MDIs that are closely spaced in one direction and relatively far apart in a perpendicular direction can give rise to stable linear channels. We observe that a linear channel spanning the entire width of the simulation cell forms and remains stable. MDIs seem to be able to "pin" the precipitate in place, preventing it from coalescing. Considering the results we presented in Chapter 3, this may be somewhat counterintuitive. The spacing between the closest spaced MDIs can influence the final precipitate shape. If these MDIs are too close together, it is easier for the precipitate to dewet and coalesce. However, if the closest MDI spacing is larger, it may be more difficult for the precipitate edges to dewet and migrate inwards to the precipitate center. Thus there may be some range of minimum MDI spacing that is optimal for pinning the He precipitate network in a linear configuration.
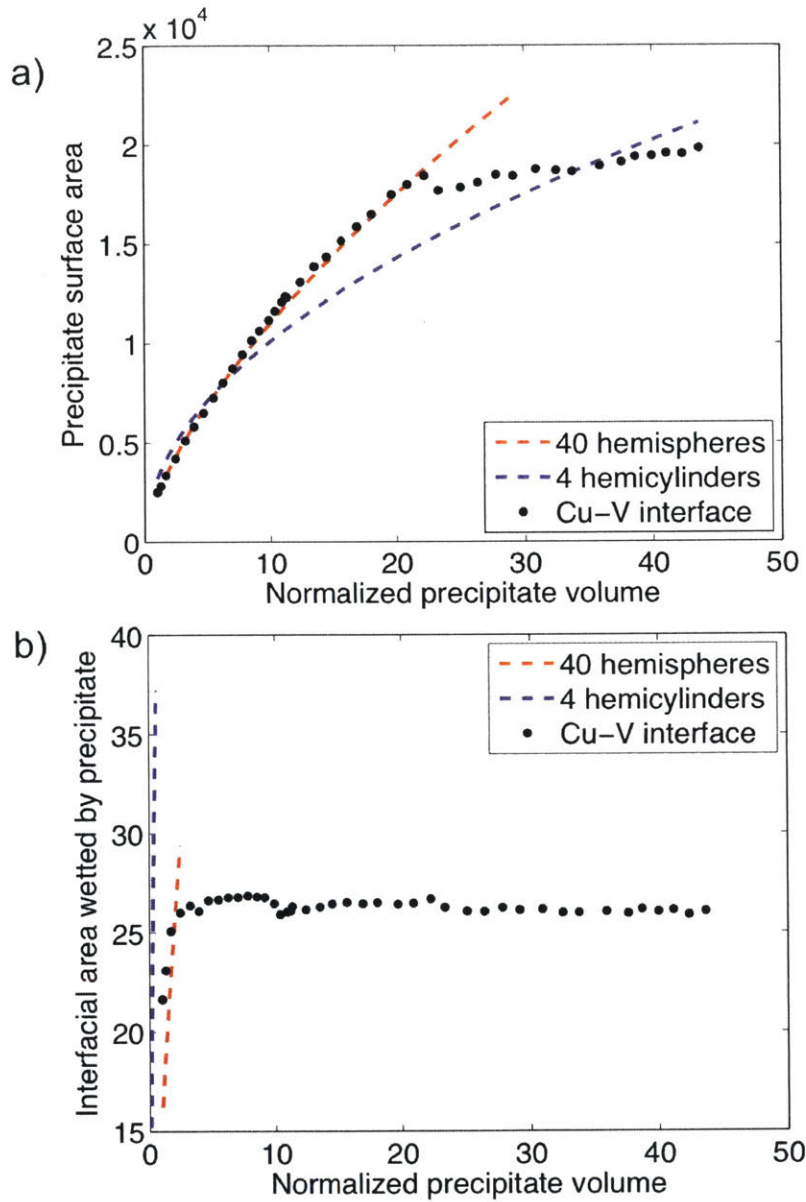
Figure 4-3: a) The total surface area of the precipitate as a function of normalized precipitate volume. The red dashed line represents the precipitate surface area of 40 spherical caps and the blue dashed line represents the surface area of 4 horizontal spherical segments with fixed length of 23nm, both on a uniform surface with wetting angle 115°. b) The interfacial wetted area of the precipitate as a function of normalized precipitate volume. The red dashed line represents the precipitate surface area of 40 spherical caps on a uniform interface and the blue dashed line represents the wetted interfacial area of 4 horizontal spherical segments with fixed length of 23nm, both on a uniform surface with wetting angle 115°.

80

4.3 He wetting of adjacent Cu-V interfaces

4.3.1 Simulation set up for two adjacent interfaces

In the previous section, we considered the growth and coalescence of He bubbles at a single Cu-V interface. However, if a Cu-V interface was used in a large scale reactor for He management, it would be insufficient to have a single interface. Rather, a macroscale multilayer (with nanometer scale layer thickness) would be needed to maximize the number of interfaces for He precipitation and outgassing. Thus we consider how the He precipitate behavior change when we have two adjacent Cu-V interfaces. Because He preferentially grows into the Cu layer, He bubbles on two adjacent interfaces will interact with each other within the Cu layer, with one set of bubbles growing up from the bottom interface and the second set of bubbles growing down from the top interface. The V layers would remain relatively free of He.

To model two adjacent Cu-V interfaces, we begin with a simulation cell very similar to the one described in section 4.2.1. On the bottom boundary we have an MDI distribution, just like in the single interface case. In addition, a MDI distribution is also present on the top boundary as shown in figure 4-4.a). The MDIs are wetting and are represented by red circles while the rest of the interface is non wetting. Periodic boundary conditions are applied in the x and y directions of the simulation. In figure 4-4.a), we show an MDI distribution on the top interface that is identical to that on the bottom interface. However, the relative orientation of the MDI distributions on the top and bottom interfaces are not necessary identical, nor are they random: there are specific orientations that will be observed in a Cu-V system.

When a Cu layer is deposited on a V layer in the K-S orientation, we see an MDI distribution predicted by O-lattice theory. The $[\bar{1}10]$ direction in the (111) Cu plane is parallel to the $[\bar{1}0\bar{1}]$ direction in the (110) V plane [90]. These directions are fixed in these two deposited layers, as is the MDI distribution. When another V layer is deposited on top of the Cu layer, the only constraint for a K-S orientation relationship is that a $<110>$ type direction in the $\{111\}$ Cu plane must be parallel to a $<111>$ type direction in the $\{110\}$ V plane. There are $2 < 110 >_{fcc}$ directions and $3 < 111 >_{bcc}$ directions as shown in Fig. 4-

81
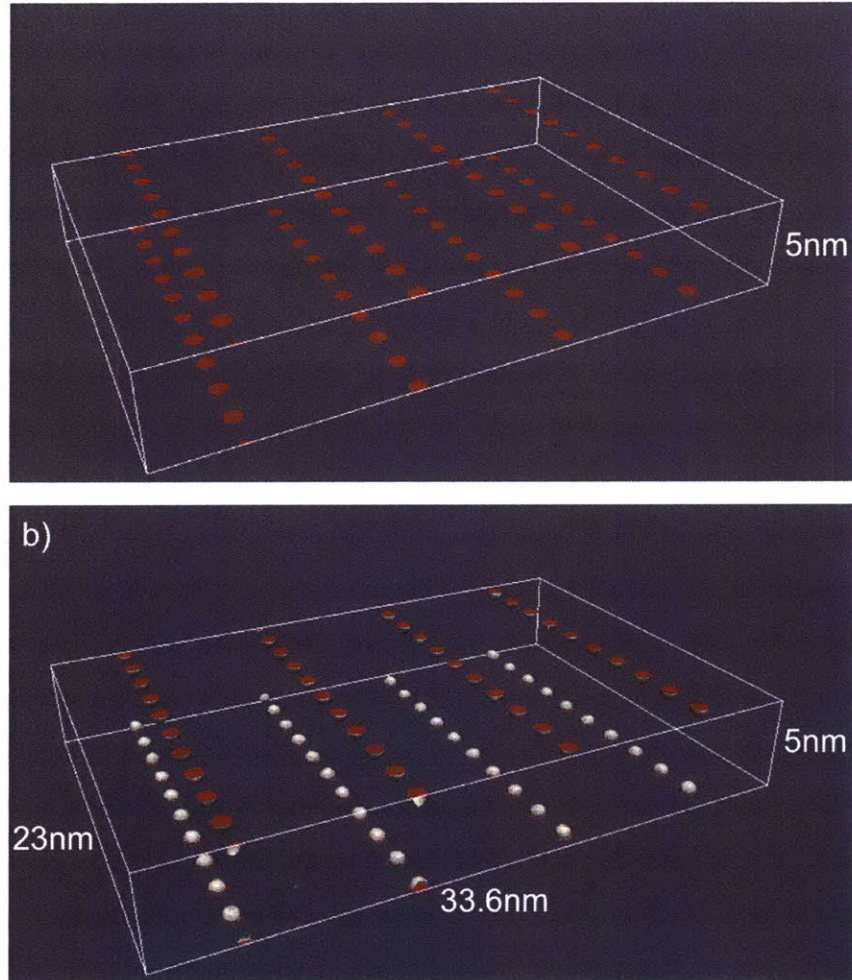
Figure 4-4: a) The simulation cell for two adjacent Cu-V interfaces described in section 4.3.1. The red circles are wetting regions while the surrounding interface area is non-wetting. Periodic boundary conditions are applied in the x and y directions b) Initial pre-cipitate morphology with a helium bubble covering each wettable patch. This figure shows the isosurface with order parameter c=0.

5.a). Thus there are six possible misorientations of the MDI distribution of the top interface relative to the MDI distribution of the bottom interface. These possible misorientations are shown in Fig. 4-5.b). The first possibility is no misorientation, such that the MDIs in the top interface are parallel to the MDIs in the bottom interface. While there is no rotation of the MDI distribution of the top interface relative to the MDI distribution of the bottom interface, there can be an inplane translation. The extreme cases are: 1) the MDI distribution in the top interface is directly above the MDI distribution in the bottom interface and 2) The MDI distribution in the top interface is offset in the $\hat{n}$ direction by $\frac{1}{2}l_\perp = 4.2nm$. The second and third possibilities are a 60° misorientation where $[\bar{1}01]_{fcc}||[\bar{1}1\bar{1}]_{bcc}$ and a 120° misorientation where $[0\bar{1}1]_{fcc}||[\bar{1}1\bar{1}]_{bcc}$. Rotating the MDI distribution 60° or 120° relative to the bottom interface yields an identical pattern, where is a reflection of the other. The fourth possibility is a 10.5° misorientation when $[\bar{1}01]_{fcc}||[\bar{1}11]_{bcc}$ as shown in Fig. 4-5.b)iv). This 10.5° angle is twice the rotation angle that corresponds to the K-S orientation in section 2.4. The fifth possibility is a 70.5° misorientation when $[\bar{1}10]_{fcc}||[\bar{1}11]_{bcc}$ as shown in Fig 4-5.b)v). Finally, the last misorientation is 130.5° which corresponds to $[0\bar{1}1]_{fcc}||[111]_{bcc}$ shown in Fig. 4-5.a)vi). The 70.5° and 130.5° misorientation cases, while differing in the MDI pattern, are qualitatively similar to the 60° and 120° cases respectively. The 10.5° misorientation MDI pattern is different from all other cases discussed.

While these different MDI distribution orientations may yield different He precipitate configurations, due to the computationally expensive nature of these simulations, we only examine the case where there was no MDI misorientation or inplane translation in the top interface. A He precipitate was placed at each MDI location, such that the diameter of the precipitate equaled that of the MDI as shown in figure4-4.b). Just like for the single interface case, we set $f_{grow} = 0.4$.

83
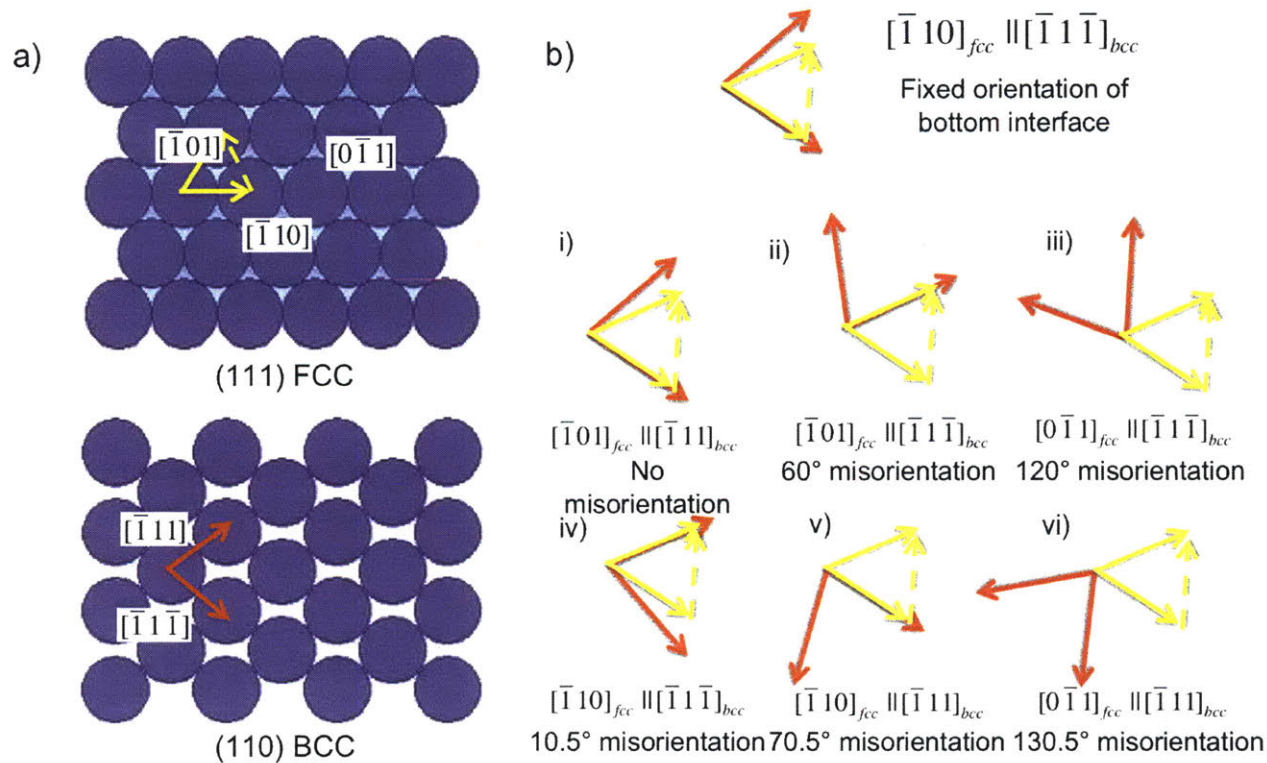
Figure 4-5: a) This shows the atomic structure of a {111} fcc plane and a {110} bcc plane with their <110> and <111> type directions respectively. b)Depicts the possible orientations of the different $<111>_{BCC}$ and $<110>_{FCC}$ directions relative to each other. There are 7 possible misorientations.
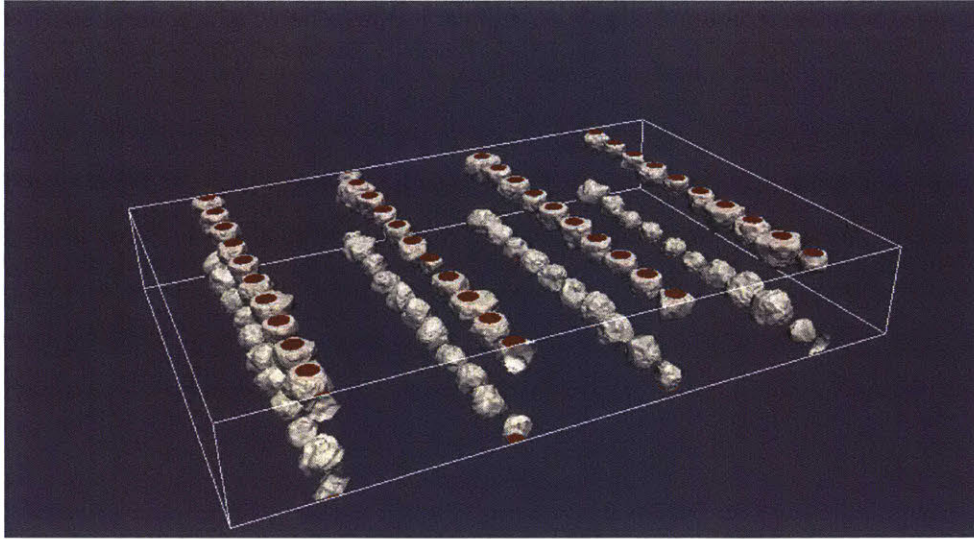
Figure 4-6: A perspective view of the c=0 isosurface of He precipitates at two adjacent Cu-V interfaces patterned with MDIs.

4.4 Results and analysis: He precipitate formation at two adjacent Cu-V interfaces

The results of the simulation of He precipitates growing at 2 adjacent Cu-V interfaces is shown in figure 4-6. Due to time and computational constraints, the precipitates were not grown sufficiently to induce coalescence either within a single Cu-V interface or between adjacent planes. Based on the results for a single interface, we can infer that linear channels would form independently at each Cu-V interface. Based on the simulations and results discussed in chapter 5, we can also assume that two wetting interfaces would stabilize the linear channels. However, to confirm this result, precipitate will need to continue to be added. The experimental results presented in the next section further support our hypothesis that linear channels will form with this interfacial structure.

4.5 Comparison to experimental results

Using the phase field methodology, we predicted that linear channels would be observed at a single Cu-V interface. While the precipitates on the two adjacent interfaces did not

interact due to time and computational constraints, it is reasonable to assume that a similar result would occur: linear channels would form. In section 2.6, the experimental results of He implantation in a Cu-V bilayer were presented. It was concluded that the dominant feature that patterned the He precipitates was wetting ribbons due to steps deposited in the interface as a result of dislocation loops undergoing confined layer slip in their glide planes. However, some evidence was observed that MDIs did indeed pattern the interface. It is possible that both MDIs and wetting ribbons were present in the interface, and that the wetting ribbons dominated: they were higher energy and thus were more favorable locations for wetting.

In order to minimize the presence of wetting ribbons and attempt to isolate only MDIs at the interface, our collaborators at LANL synthesized a Cu-V trilayer with a very thin copper layer. According to Misra *et al.*, the shear stress, τ, required to propagate a dislocation loop confined to a layer in its glide plane is given by [113]:

$$\tau = 2W/bl \tag{4.10}$$

where W is the self-energy of the dislocation, b is the Burgers vector, and l is the thickness of the layer. Thus, decreasing the layer thickness increases the shear stress needed to move the dislocation through the layer. As it becomes more difficult for the dislocation loop to propagate, the less likely that it will move through the layer and deposit a step at the interface. Thus, for the trilayer synthesis, we aimed for a Cu layer thickness on the order of nanometers to suppress step formation.

The synthesis technique used to make this sample is very similar to that described in section 2.6. A 150nm V layer was deposited on a MgO substrate. Then a thin 5nm layer of Cu was deposited on top. Finally, a 150nm V layer was deposited. TEM foils were made from the sample and subsequently implanted with 30KeV He+ ions to a fluence of $1 \times 10^{12} ions/cm^2$ at $250°C$ using a 200kV Dankysuk research ion beam implanter. Finally, in-plane and edge-on TEM imaging was performed to observe the He bubble distribution. Both under and over focus TEM was performed to ensure that the He network features observed are not artifacts in the image.
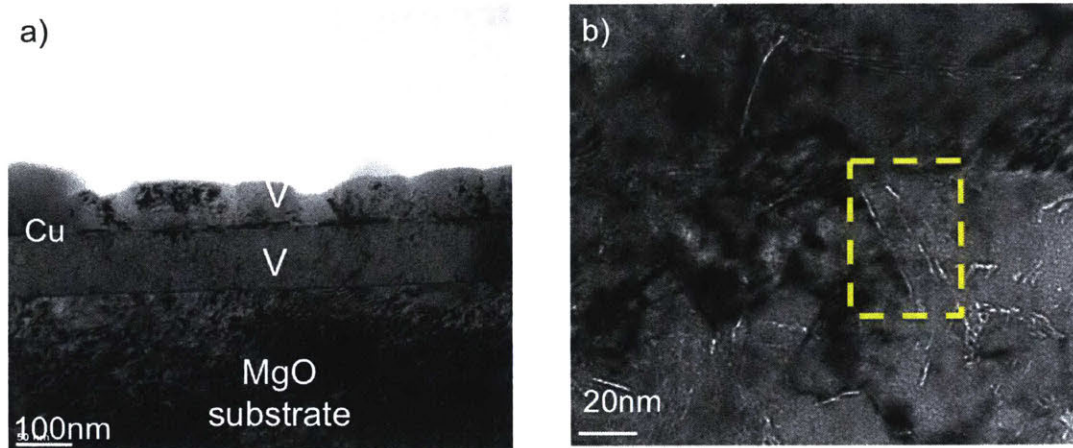
Figure 4-7: a) TEM image of the edge-on view of a Cu-V trilayer. Each vanadium layer is 150nm and the Cu layer is 5nm. b) TEM image of the in-plane view of the Cu-V interface. White lines are linear channels formed by He precipitates. The yellow box highlights two aligned channels that are approximately 10nm apart, corresponding to the spacing predicted by O-lattice theory of 8.6nm

The edge-on TEM results are shown in figure 4-7.a). The Cu-V interfaces in this sample are very flat, conducive to observing intrinsic structural interfacial features. The in-plane TEM results are shown in figure 4-7.b). The white lines are believed to be linear channels that have formed in the interface. These channels appear to aligned in somewhat random directions and do not seem to be aligned like we might expect for a grid of MDIs. However, there are 2 channels that are aligned with respect to each other, as highlighted by the yellow box in figure 4-7.b). Furthermore these two channels have a spacing of 10nm, which agrees with the O-lattice calculation that rows of MDIs (i.e. $l_\perp$) should have a spacing of 8.6nm. Further analysis will be need to be conducted to determine the orientation of the Cu-V grains and if they correspond to the predicted orientations for a Cu-V interface in a K-S orientation relationship. This experimental result has provided promising evidence that both our O-lattice and phase field predictions are valid. Furthermore, it confirms that we have successfully been able to design an interface that forms linear channels when implanted with He.

87

4.6 High performance computing troubleshooting

The simulations presented in Chapter 4 were done on two high performance computing systems: Idaho National Laboratorys Falcon cluster, and Texas A&M University's Ada cluster. While these clusters have different architecture and batch scripting environments, similar computational issues were encountered on both systems due to running resource intensive simulations. In this section, simulation scaling and memory management are discussed.

MOOSE is a C++ based finite element, fully coupled, fully implicit multiphysics solver. MOOSE has been thoroughly tested for its parallel performance, with its largest runs completed on over 100,000 processors [3]. Figure 4-8.a) demonstrates the strong scaling of MOOSE running a phase-field model created by Williamson *et al*. Strong scaling defines how the run time changes as the number of processors increases for a fixed size problem. This scaling study was performed on a grain growth simulation of 512 grains in a polycrystalline material with 1,024 coupled variables [2]. The strong scaling trends are consistent with ideal speedup (black hatched curve) up to 5,000 processors. Depending on the physics of the problem, MOOSE runs most efficiently when one processor is used per 5,000-20,000 degrees of freedom (DOFs). Below 5,000 DOFs per processor it is still possible to accelerate solve time, however, CPU performance is not maximized. A small optimization study was performed on a phase field simulation containing approximately 10^6 DOFs. This study was run on 40, 60, 100, and 140 processors. After each simulation was run, the total solve time was recorded. The results of this study are plotted in Fig. 4-8.b with solve time in seconds on the y-axis and number of processors on the x-axis. Total time linearly decreases with number of processors, as expected for strong scaling, up to 100 processors. Between 100 and 140 processors, the wall clock time levels off. This suggests that running the phase field simulations with approximately 10,000 DOFs per processor is optimal for the physics of the model. The Cu-V systems are initialized with $\sim 10^6$ DOFs, roughly proportional to the number of mesh elements in the simulation. However, because a mesh adaptivity algorithm is employed, this value increases as the amount of interface area between the He and precipitate increase. Typically, the simulations see up to 5×10^7 DOFs over the course

88
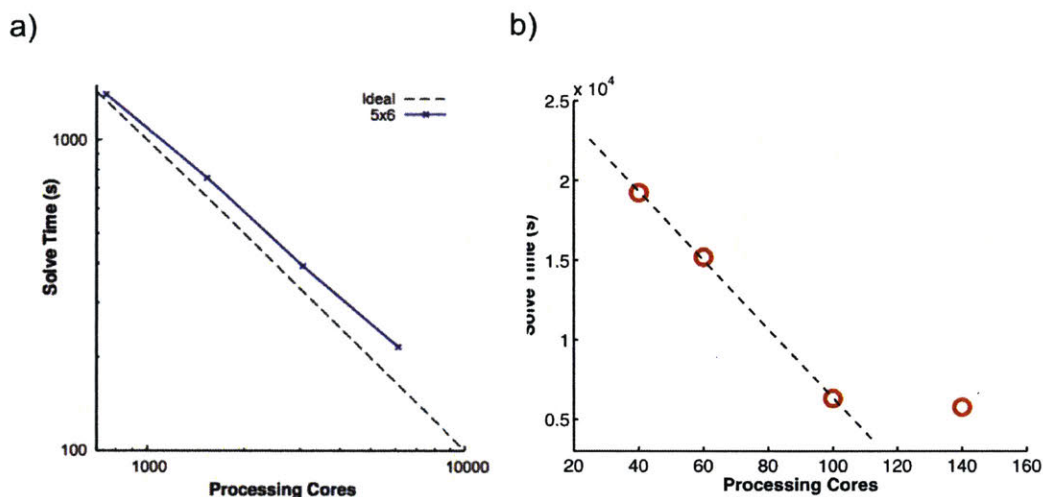
Figure 4-8: a) Solve time as a function of processing cores for a strong scaling phase-field study run by Williamson *et al.* [3]. b) Solve time as a function of processing cores for the physics relevant to the Cu-V simulation. Solve time levels out when computing power drops below 10,000 DOFs per processor.

of all steps, thus using 5,000 processors would provide the greatest simulation efficiency. Due to constraints on the number of processors allowed per user for HPC computing facilities, a maximum of 1,000 processors were used for the Cu-V simulations, but less were used for initial steps with less DOFs. Tracking the DOFs within a simulation and between simulations can help optimize number of processors as well as inform memory use.

Because of the scale of the simulations, it is important to be mindful of memory usage when running a job on a HPC cluster. The typical architecture for a large computing cluster is to have a node consisting of individual cores or processors. The Falcon and Ada cluster had 24 and 20 cores per node respectively. Each node has a memory allocation– 120GB and 64GB, with each processor having 5GB and 3.2GB available for use on Falcon and Ada respectively. However, when using all the processors on a node, the memory use of the Cu-V jobs exceeded the allocated memory and the jobs crashed. Thus it was necessary to request all of the memory on a single node but only some of the processors, ensuring more memory per process. For Falcon, requesting 120GB for 12 processors or 10GB per processes accommodated the memory requirements for the Cu-V simulations. Similarly, requesting only 5 processors per node on ADA or 12.8GB per process, but the whole node

89

memory provided enough memory for the simulations.

4.7 Discussion of Cu-V results

In this chapter we have combined the results of Ch. 2 and Ch. 3 to simulate the behavior of He bubbles at a Cu-V interface patterned with wetting MDIs. We found that given the MDI distribution of a Cu-V interface, it is possible for stable linear channels to form. This result was substantiated by experimental observations of linear channels forming in a Cu-V trilayer implanted with He.

Our Cu-V simulation captures the growth and coalescence of the He bubbles at MDIs as well as the subsequent stability of the channels. However, this model has limitations and can be improved upon to capture more features of a physical Cu-V interface. One modification to the model, discussed in section 3.5, would be to couple hydrodynamics to the phase field equations to capture possible outgassing. This would be difficult to capture experimentally, as the edges of the implanted sample would need to be very clean, and the MDIs would need to terminate on the free surface in a certain orientation, thus necessitating a computational result.

In our simulation, we model the MDIs as perfect circles with a sharp delineation between wetting and non-wetting regions as a means of simplifying the system. In reality, there is a gradient in the energy of the MDIs, peaking at the center of the MDI and decreasing radially outward [114]. This would correspond to a variation in the wetting angle, with the minimum wetting angle at the MDI center and gradually increasing outward until the wetting angle is greater than 180° i.e. non-wetting. This could be captured by introducing a position dependent wetting angle to the Neumann wetting boundary condition within the MDI region. Having a more diffuse boundary between wetting and non-wetting regions may decrease the pinning of precipitates we observed in these simulations. Furthermore, experimental evidence has been observed that both wetting ribbons and MDIs coexist at an interface. This could be captured in our simulation by introducing wetting ribbons to the MDIs. The angle of the wetting ribbons relative to the MDI distribution can be calculated, however there are innumerable possible combinations because wetting ribbons do

90

not follow a repeating pattern.

While we were not able to capture coalescence of the two interface Cu-V simulation due to time and computational constraints, we can expect that within each interface, we would find linear channels forming. However, there is still a question of what the precipitate behavior would be if the precipitates from the top and bottom interface were to interact. It is possible that having two interfaces stabilizes a linear precipitate, preventing a Raleigh-Taylor instability from occurring [115], but further work would need to be done to confirm this. Furthermore, misoriented MDI distributions on the top and bottom interface could give rise to He precipitate shapes not considered here, and would need to be investigated through additional simulations.

In this chapter, we focused on MDIs as the only structural feature of the interface that impacts He wetting. However, as mentioned previously, linear steps in the interface form wetting ribbons that can not only influence He precipitation, but may be the dominating wetting feature. In the next chapter, we study how wetting ribbons effect He precipitate network structures.

Chapter 5

Applying a phase-field model to He precipitation on high energy wetting ribbons at the interface

5.1 Introduction

While the primary goal of this thesis work was to design an interface that gives rise to He channels using MDIs, experimental results discussed in section 2.6 suggest that MDIs are not the only interfacial structural feature templating He precipitation. TEM imaging done on a He implanted Cu-V bilayer showed that He bubbles preferentially aligned along steps formed by dislocation loops gliding in the $\{111\}$ slip planes of the FCC lattice pointing the $<110>$ direction. Unlike MDIs, these slip steps do not repeat periodically, rather their distribution is random. The energy of these slip steps has been found to be somewhat higher than those of MDIs by Sanket Navale of the Demkowicz group, thus providing a greater driving force for He wetting than MDIs. This provided the motivation needed to examine the behavior of He precipitates at isolated rectangular wetting ribbons as a means of determining if high energy slip steps give rise to linear He channels at an interface. Furthermore, a wetting ribbon can be thought of as a limiting case of a row of MDIs– as the MDI closest spacing (l_{min}) decreases, the MDIs will eventually become indistinguishable

from one another and form a wetting ribbon.

5.2   Simulation set up of wetting ribbons

We consider three cases of wetting ribbons: a single wetting ribbon on an interface, two wetting ribbons on adjacent interfaces with one directly above the other, and finally two wetting ribbons on adjacent interfaces with one orthogonal to the other. These three cases can give us a qualitative picture of what we can expect from the He behavior at these high energy slip plane steps. These simulations were set up using the phase field model developed in chapter 3.

To model a high energy slip step in a bilayer, we constructed a simulation cell shown in figure 5-1.a). This cell has a wetting ribbon on the bottom face of width 1.5nm and length 20nm. The rest of the bottom face has non wetting boundary conditions applied to it. Periodic boundary conditions were applied in the direction of the ribbon (the x-direction in the figure5-1a)). The upper boundary and the remaining two sides of the simulation cell had no-flux boundary conditions applied. We do not expect the precipitate to interact with either of these boundaries. The size of the simulation cell is 20nm x 7.5nm x 5nm. Eight He precipitates of diameter 1nm were placed on the wetting ribbon with an equal spacing of 1.25nm between them. This initial condition is shown in figure 5-1.d), where isosurfaces of c=0 are rendered.

To demonstrate how He precipitates behave at two adjacent interfaces, like that of a Cu-V trilayer, we constructed a simulation cell shown in figure 5-1.b). This cell has two wetting ribbons, one on the top and one on the bottom face, of size 1.5nm x 20nm. The wetting ribbon on the top face is directly above the wetting ribbon on the bottom face. The remainder of these boundaries have non-wetting boundary conditions. Periodic boundary conditions are applied in the direction of the ribbon (the x-direction in figure 5-1.b)). The other two sides, normal to the y-direction, had no-flux boundary conditions applied. We do not expect the precipitate network to interact with these boundaries. However, we do expect the precipitates on the top and bottom boundaries to interact with each other. The size of the simulation cell is 20nm x 7.5nm x 5nm. Eight He precipitates of diameter 1nm

94

were placed on each of the wetting ribbons with an equal spacing of 1.25nm between them. The c=o isosurfaces of this initial condition is shown in figure 5-1.e).

The scenario with two adjacent interfaces containing ribbons one directly above the other can be considered an extreme case, since in a real Cu-V system there is a random distribution of where these dislocations nucleate, it is unlikely that this situation would occur. However, since there are many possible configurations, we choose to examine the "edge" cases as a way to place limits on the possible behaviors. In addition to the situation mentioned, when the wetting ribbons are in line with each other, we consider a case where the ribbon on the top interface is perpendicular to the ribbon in the bottom interface. There is also the possibility that in a trilayer system, a high energy slip step in the lower interface does not have a slip step in the upper interface. In this case, we can apply the results of the single ribbon case.

Figure 5-1.c) shows the simulation cell containing two orthogonal wetting ribbons of size 1.5nm x 20nm on adjacent interfaces. The remainder of the top and bottom boundary have non-wetting boundary conditions. Periodic boundary conditions are applied in the direction of the ribbon (thus the x and y directions in figure 5-1.c)). We expect that the precipitates will interact with all boundaries and the precipitates on the top and bottom boundary to interact with each other. The size of the simulation cell is 20nm x 20nm x 5nm. Eight He precipitates of diameter 1nm were placed on each of the wetting ribbons with an equal spacing of 1.25nm between them. Figure 5-1.f) shows this initial condition.

We ran each wetting ribbon configuration described above with three different wetting angles: 60°, 90°, and 120°. Like in the case of the Cu-V simulations described in chapter 4, we used $f_{grow} = 0.4$. Initially, the precipitates are uniformly growing in size, not interacting with any other precipitates. Coalescence events first occurred in the direction of of the ribbon (x-direction). For the parallel and orthogonal ribbon cases, subsequent precipitate interaction occurred between He on adjacent interfaces.
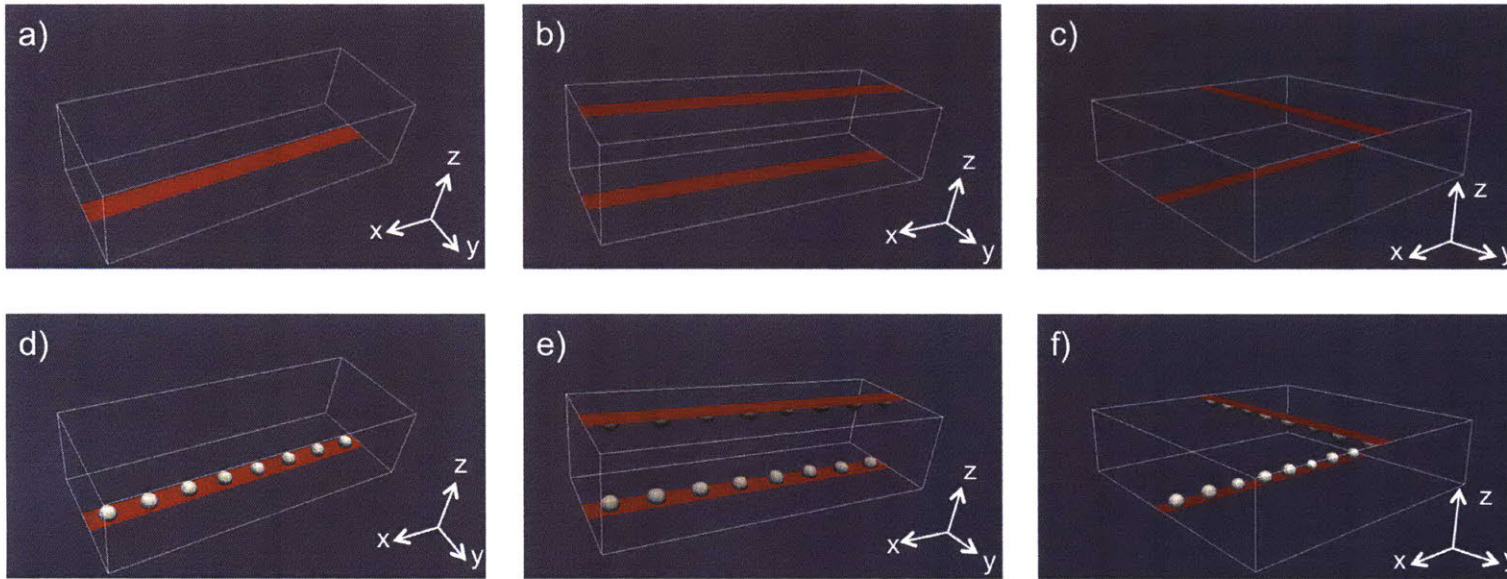
Figure 5-1: a) The simulation cell for a single wetting ribbon, b)two parallel wetting ribbons on adjacent interfaces and c) two orthogonal wetting ribbons in adjacent interfaces. The red areas are wetting regions while the surrounding interface area is non-wetting. d) Initial precipitate morphology with eight helium bubbles equally spaced along a single wetting ribbon, e) sixteen helium bubbles equally space along two parallel wetting ribbons on adjacent interfaces and f) sixteen heium bubbles equally spaced along two orthogonal wetting ribbons on adjacent interfaces.

5.3 Results of wetting ribbon simulations

The final precipitate configurations for the three constructed simulation cells and the three studied wetting angles are shown in figure 5-2. Figure 5-2.a-c) shows the results for the single wetting ribbon, 5-2.d-f) shows the results for two parallel wetting ribbons, and finally 5-2.g-i) shows the results for two orthogonal wetting ribbons. From qualitative observations of the final precipitate morphologies, we conclude that the end morphologies are similar regardless of wetting angle within each wetting ribbon configuration. Thus, for example, for the single wetting ribbon, there are no particular features that distinguish the 60° case from the 90° and 120° case. For the single wetting ribbon cases, the final morphology for all wetting angles is an elongated "baguette" like structure. For the parallel wetting ribbon case, the final morphology is also elongated but more sheet like. The sides of the precipitate are more vertical rather than bowed out like in the single wetting ribbon case. Finally, for the orthogonal ribbon case, the final precipitate morphology is elongated in the direction of the ribbon, with a rounded cylindrical feature at the center of the simulation cell where the precipitates from the top and bottom interface interact.

To further investigate morphology behavior, we tracked the precipitate surface area and interface area wetted by the precipitate as a function of the normalized volume for the nine wetting ribbon cases discussed. The methodology for calculating these values is described in section 4.2.2. The results of the surface area as a function of normalized volume and the wetted interface area as a function of normalized volume for the single ribbon, parallel ribbon, and orthogonal ribbon case are shown in figures 5-4, 5-5, and 5-6, respectively.

To contextualize the values we extract from the single ribbon simulation, we calculate reference cases for the surface area and wetted interface area for a given precipitate volume as we did in section 4.2.2. We considered the following reference cases: 8 hemispherical caps on a uniform interface and a single horizontal cylindrical segment on the wetting ribbon, with length fixed to that of the wetting ribbon. The 8 hemispherical caps are always at the specified equilibrium wetting angle– either 60°, 90°, or 120°. The horizontal cylindrical segment, however, starts off at the equilibrium wetting angle, but as the precipitate grows and exceeds the width of the wetting ribbon, the wetting angle begins to increase. Because

97
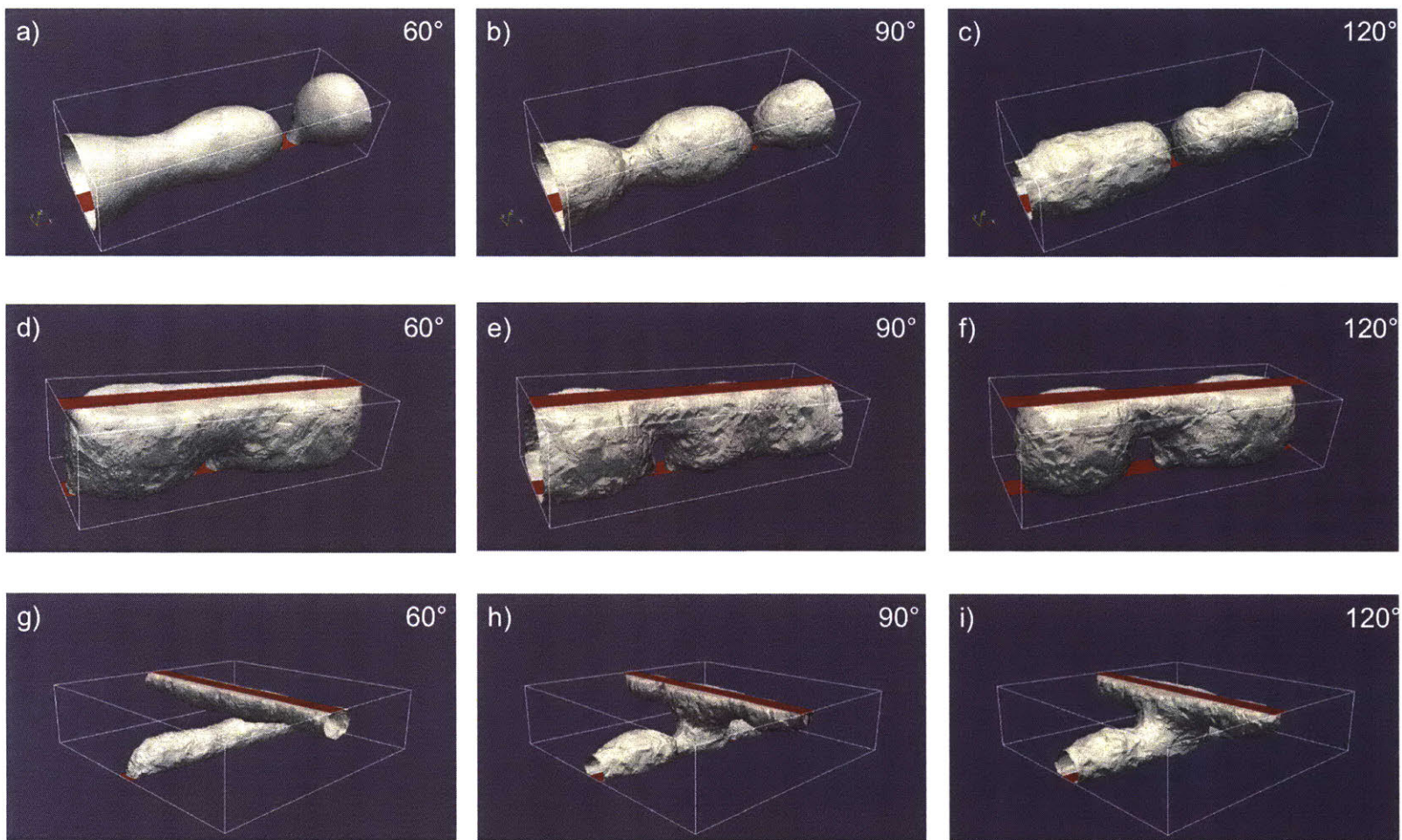
Figure 5-2: The final morphologies for the nine different combinations of wetting ribbon configuration and wetting angles. a-c) The c=0 isosurface for the single wetting ribbon configuration with 60°, 90°, and 120° wetting angles. d-f)The c=0 isosurface for the two parallel wetting ribbons configuration with 60°, 90°, and 120° wetting angles. g-i)The c=0 isosurface for the two orthogonal wetting ribbons configuration with 60°, 90°, and 120° wetting angles.
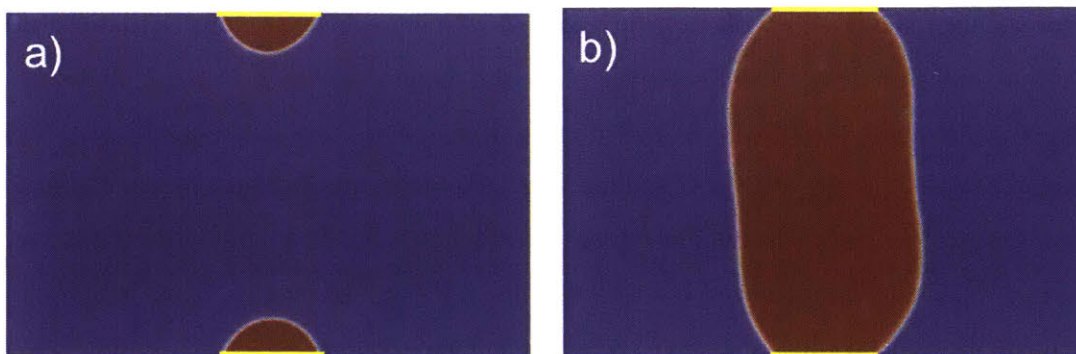
Figure 5-3: a) The initialized simulation cell used to calculate the horizontal cylindrical segments reference case for the parallel and orthogonal ribbon simulation set up, where red coloring corresponds to the helium phase and blue coloring corresponds to the metal phase. A 2D simulation was run and precipitate surface area and interfacial area was extracted. Since the length of the horizontal cylindrical segment is fixed to that of the length of the wetting ribbon, surface area and interface area values are multiplied by 20. The yellow line segments in the figure show the wetting area of the cell. Here, the wetting angle is 60°, but similar runs were done for 90° and 120°. The rest of the boundary is non-wetting. b) This image captures the coalescence event between the top and bottom precipitate, corresponding to a sharp decrease in the precipitate surface area.

of this change in the wetting angle, the horizontal cylindrical segment reference case was calculated numerically via simulation while the 8 hemispherical caps case was calculated analytically.

Since the length of the horizontal cylindrical segment was fixed to that of the wetting ribbon, three 2D simulations were run that only considered the cross-section of the cylinder (for the 90° case, this would look like a semicircle). The wetting region was defined as a line segment at the base of the 2D simulation cell. The simulation cell used to calculate the reference case for the 2 parallel wetting ribbons with a wetting angle of 60° is shown in figure 5-3.a) and the wetting segments are rendered in yellow. A precipitate is put on the wetting region and precipitate is added with each simulation step. The single ribbon case had a very similar setup, with just a single precipitate on one interface. From these 2D simulations, the volume, surface area, and wetted interface area was extracted. These values were then multiplied by 20nm, the length of the wetting ribbon.

The precipitate surface area as a function of normalized volume for the 60°, 90°, and 120° for the single wetting ribbon set up is plotted in figure 5-4.a) along with the reference

99

cases outlined above. The volume is normalized by the precipitate volume initialized in the first simulation step. The 60° case is plotted in red circles, the 90° case is plotted in blue triangles and the 120° case is plotted in black plus signs. The blue dotted line is the 90° 8 spherical caps reference case and the blue solid line is the 90° horizontal cylindrical segment reference case. The reference case curves for 60° and 120° are very similar to the 90° case and are not plotted here. For both the spherical caps and the horizontal cylindrical segment, the 60° and 120° cases have slightly higher surface areas for a given volume than the 90° reference case.

For low normalized precipitate volume (less than approximately 10), the precipitate surface area for all three cases closely follows the 8 spherical cap reference case. At higher precipitate volumes, the precipitate surface areas begin to deviate from the 8 spherical cap reference case and begin to more closely follow the horizontal cylindrical segment reference case. Based on the trajectory of the surface area, the final precipitate morphology for the three wetting angles is similar, as confirmed through visual inspection of the c=0 isosurfaces. However, the path to reach this final morphology varies for each wetting angle. From the surface area data, the 60° case follows the horizontal spherical segment reference case the closest, while the 120° deviates the most from it. The 90° reference case interpolates between the two.

Unlike the reference case curves, the data extracted from the simulations does not give smooth curves. Rather we observe small waves and "irregular" features that are a result of precipitate morphologies that are neither perfect spherical caps nor horizontal cylindrical segments, but combinations of the two. For example, in the 90° case, around a normalized precipitate volume of 15, the data begins to deviate from the horizontal cylindrical segment reference case and around a normalized precipitate volume of 30, the data once again begins to align with the reference case. Visually inspecting the c=0 isosurfaces, we find that at the maximum deviation from the reference curve we have 2 spherical precipitates and one more elongated cylindrical precipitate. When the 90° data becomes more aligned to the reference case, we find there is a coalescence between the two spherical precipitates across the periodic boundary, resulting in two rather elongated precipitates. This makes sense because as the precipitate evolves closer and closer to a single cylindrical precipitate, the

100
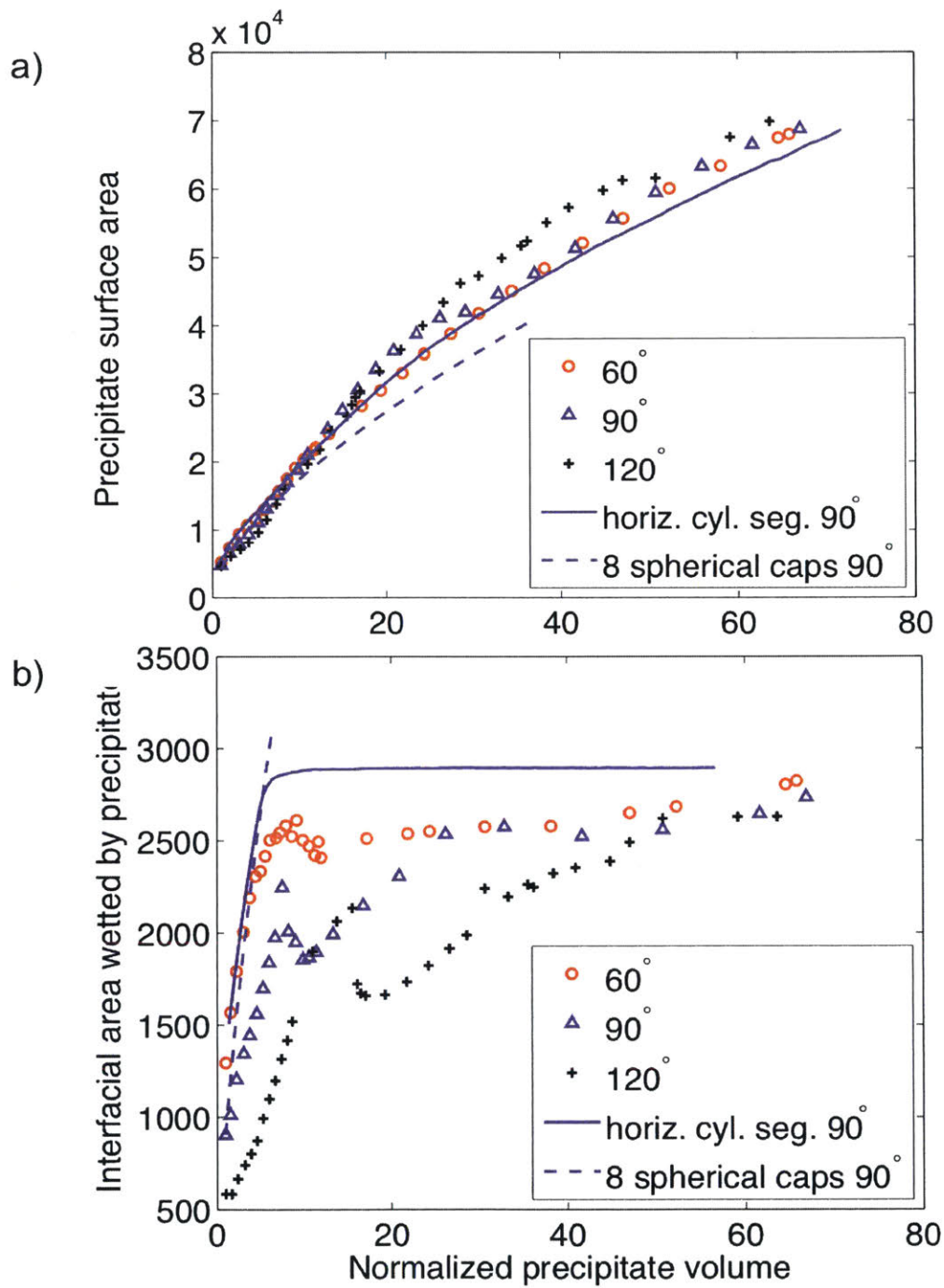
Figure 5-4: a) The plot of the precipitate surface area as a function of normalized precipitate volume for 60° (red circles), 90° (blue triangles), and 120° (black plus signs) wetting angles for a single wetting ribbon. b) The plot of the interfacial area wetted by the precipitate as a function of normalized precipitate volume for 60°, 90°, and 120° wetting angles for a single wetting ribbon. Reference cases are rendered in the blue dashed and solid lines.

more similar the surface area between the precipitate and the reference case should be.

The interfacial area wetted by the precipitate as a function of normalized volume for the 60°, 90°, and 120° for the single wetting ribbon set up is plotted in figure 5-4.b) with the corresponding reference cases. The 60° case is plotted in red circles, the 90° case is plotted in blue triangles and the 120° case is plotted in black plus signs. The blue dotted line is the 90° 8 spherical cap reference case and the blue solid line is the 90° horizontal cylindrical segment reference case. Again, we do not plot the 60° or 120° reference cases because the are very similar in magnitude and shape. For both reference cases, as normalized volume increases, there is a sharp increase in the wetted area. For the spherical cap case, the curve continually increases because in the calculation we assume the caps are non-interacting and there is no limit to the available wetting area. On the other hand, for the horizontal cylindrical segment case, we observe a sharp increase and saturation of the wetted interface area at a normalized precipitate volume of approximately 10. At this point, the cylindrical segment has wetted the entire area of the ribbon so increasing volume has no effect on the area wetted. Furthermore, the wetting angle of the cylindrical segment begins to deviate from the equilibrium wetting angle set by the boundary conditions. Once the wetting ribbon is saturated, as we increase volume, the equilibrium angle must increase. Both 60° reference cases wet a larger area than the 90° reference cases for the same volume. The 60° horizontal cylindrical segment reference case saturates at a lower normalized precipitate volume. Conversely, both 120° reference cases wet a smaller area than the 90° reference cases for the same volume. The 120° horizontal cylindrical segment reference case saturates at a higher normalized precipitate volume.

We observe our data for all wetting angles to initially follow the spherical cap reference case for small normalized precipitate volumes and saturate to a maximum wetted interfacial area for large normalized precipitate volumes. While the 60°, 90°, and 120° cases take different paths with respect to how much interfacial area they wet, at the end of the simulation, we find that all three have wetted nearly the entire ribbon. All three cases exhibit a drop in the wetted interfacial area at different normalized precipitate volumes. This features occurs at a volume of 10 for the 60° and 90° case, and and volume of 15 for the 120° case. This drop is sharpest in the 120° case, and least sharp in the 60° case, with the

90° case somewhere in between. Inspecting the precipitate c=0 isosurfaces corresponding to these drops, we find that the drop is a result of the precipitates contracting and beading up as the precipitate volume is increased. The drop is least pronounced in the 60° case because at lower wetting angles there is a higher drive for the precipitates to wet more of the interface. Conversely, the drop most pronounced in the 120° case because at higher wetting angles there is a higher drive for the precipitates to dewet the interface. Though the 60° reference case wets more of the wetting ribbon for smaller precipitate volumes compared to the other two cases, at a normalized precipitate volume of approximately 50, all three cases are wetting nearly the same area.

The precipitate surface area and wetted interfacial area as a function of normalized volume for the 60°, 90°, and 120° for two parallel wetting ribbons is plotted in figure 5-5. Here the volume is normalized by the initial volume of the single wetting ribbon configuration. For both plots, the 60° case is plotted in red circles, the 90° case is plotted in blue triangles and the 120° case is plotted in black plus signs. Like in the single wetting ribbon case, reference cases are calculated to provide context for the data: 16 hemispherical caps on a uniform interface and two horizontal cylindrical segments on two parallel wetting ribbons, with length fixed to that of the wetting ribbon. The surface area and interfacial wetted area for the spherical caps are calculated analytically. The surface area and interfacial wetted area for the horizontal cylindrical segments are calculated numerically as described in the single wetting ribbon case. For two parallel wetting ribbons, we run a 2D simulation that considers the cross-section of two cylinders with the wetting regions defined as two line segments at the bottom and top of the 2D simulation cell as shown in figure 5-3.a). The simulation is nearly identical to that of the single ribbon case, except the top and bottom precipitate can interact with each other. In figure 5-5 The blue dotted line is the 90° 16 hemispheres reference case and the blue solid line is the two 90° horizontal cylindrical segments reference case.

Figure 5-5.a) plots the precipitate surface area as a function of normalized precipitate volume for two parallel wetting ribbons along with the reference cases discussed above. We observe an interesting feature for the 2 horizontal cylindrical segments reference case. At a normalized volume of 60, we see a sharp drop in the surface area from about 8×10^4 to

6×10^4. This feature captures the coalescence between the horizontal cylindrical segment on the top interface and that on the bottom interface as shown in figure 5-3.b). While our data for the 60°, 90°, and 120° cases closely follow the cylindrical segment reference cases for small volumes, we see that they begin to deviate at a normalized volume of 40 for the 60° and 120° cases and a normalized volume of 60 for the 90° case. These deviations are the result of when the coalescence between the top and bottom precipitates occur. For example, for the 60° case, the top and bottom precipitate initialize their coalescence at a volume of 40. Unlike the reference case, this event does not occur along the entire length of the precipitate, rather it is localized to two areas along the ribbon. This accounts for the much smaller drop in the surface area. Like in the single wetting ribbon simulations, all the cases we consider here end up at the same final surface area, although the path, i.e. the coalescence events, to get there are different.

Figure 5-5.b) plots the interfacial area wetted by the precipitate as a function of normalized precipitate volume for two parallel wetting ribbons with the reference cases. The reference cases here are qualitatively very similar to that of the single wetting ribbon configuration: sharp initial increase for both reference cases and a saturation for the horizontal cylindrical segments once the entire wetting ribbon has been wetted. The data collected for the 60°, 90°, and 120° cases is qualitatively similar to to that of the single ribbon cases: each wetting angle case takes a different path, but end up with similar total wetted area. For the 60° case at a normalized precipitate volume of 40, we observe a drop in the wetted interface. This corresponds to the coalescence event observed between the top and bottom precipitate discussed earlier. The 120° case, while having a similar coalescence even at a normalized volume of 40, does not show a drop in the wetted area at this volume. This may be because the precipitates in the 120° case are less spread out to begin with and covering a smaller interfacial area. When the coalescence even occurs, it is easier for the precipitates to form a post-like configuration. In the 60° case, the precipitates are more spread out, and when the coalescence event occurs, the precipitates need to dewet and bead up to form the post-like morphology, resulting in a drop of the covered interfacial area. We do see a dewetting event for the 120° case at a normalized precipitate volume of 50. This, however, does not correspond to a coalescence event between the top and bottom precipitates, but

Figure 5-5: a) The plot of the precipitate surface area as a function of normalized precipitate volume for 60° (red circles), 90° (blue triangles), and 120° (black plus signs) wetting angles for two parallel wetting ribbons on adjacent interfaces. b)The plot of the interfacial area wetted by the precipitate as a function of normalized precipitate volume for 60°, 90°, and 120° wetting angles for two parallel wetting ribbons on adjacent interfaces. The reference cases are rendered in dashed and solid blue lines.

105

between precipitates on the same wetting ribbon.

The final configuration investigated was two orthogonal wetting ribbons. Figure 5-6.a) plots the surface area of the precipitate as a function of the normalized volume where the red circles correspond to the 60° case, blue triangles correspond to the 90° case, and black plus signs correspond to the 120° case. The reference cases are identical to the ones calculated for the parallel ribbon case and are rendered in a solid blue line for 2 horizontal cylindrical segments and a blue dotted line for 16 spherical caps. We use the same reference cases to minimize computing costs.

Like the single ribbon and parallel ribbon configurations discussed previously, the data for the orthogonal ribbons closely follows the 16 spherical caps reference case. Around a wetting angle of 50, all three cases align to the 2 horizontal cylindrical segments reference case. An interesting feature of this plot is that unlike the other wetting ribbon set ups, the three wetting angle cases follow a very similar path as the surface area evolves. Visually inspecting the c=0 isosurfaces for different precipitate volumes, we observe that the precipitates coalesce into single linear channels at much lower volumes than observed for the other simulation setups. For the 60° and 90° case this happens at a normalized volume of approximately 25. For the 120° case this happens at a normalized volume of approximately 40. For normalized volume of 60 to 80, we see a larger deviation of the simulation data from the 2 horizontal cylindrical segments reference case when compared to the parallel ribbons data. This is because in the case of orthogonal ribbons, we do not see coalescence along the entire length of the ribbon which would result in a decrease in the precipitate surface area. Rather, we have two distinct linear precipitates on the top and bottom interfaces, with some coalescence occurring in the center of the simulation cell where the ribbons intersect. Thus we do not expect to see quite as large of a drop in the surface area for the orthogonal wetting ribbon case. Finally, the precipitates do maintain their elongated shape despite the presence of a more equiaxed precipitate feature in the center.

Figure 5-6.b) plots the interfacial area wetted by the precipitate as a function of normalized precipitate volume for two orthogonal wetting ribbons. The reference cases depicted are identical to the reference cases used for the parallel ribbon case analysis. Generally, the data observed for the 60°, 90°, and 120° cases is very similar to that of the other wet-
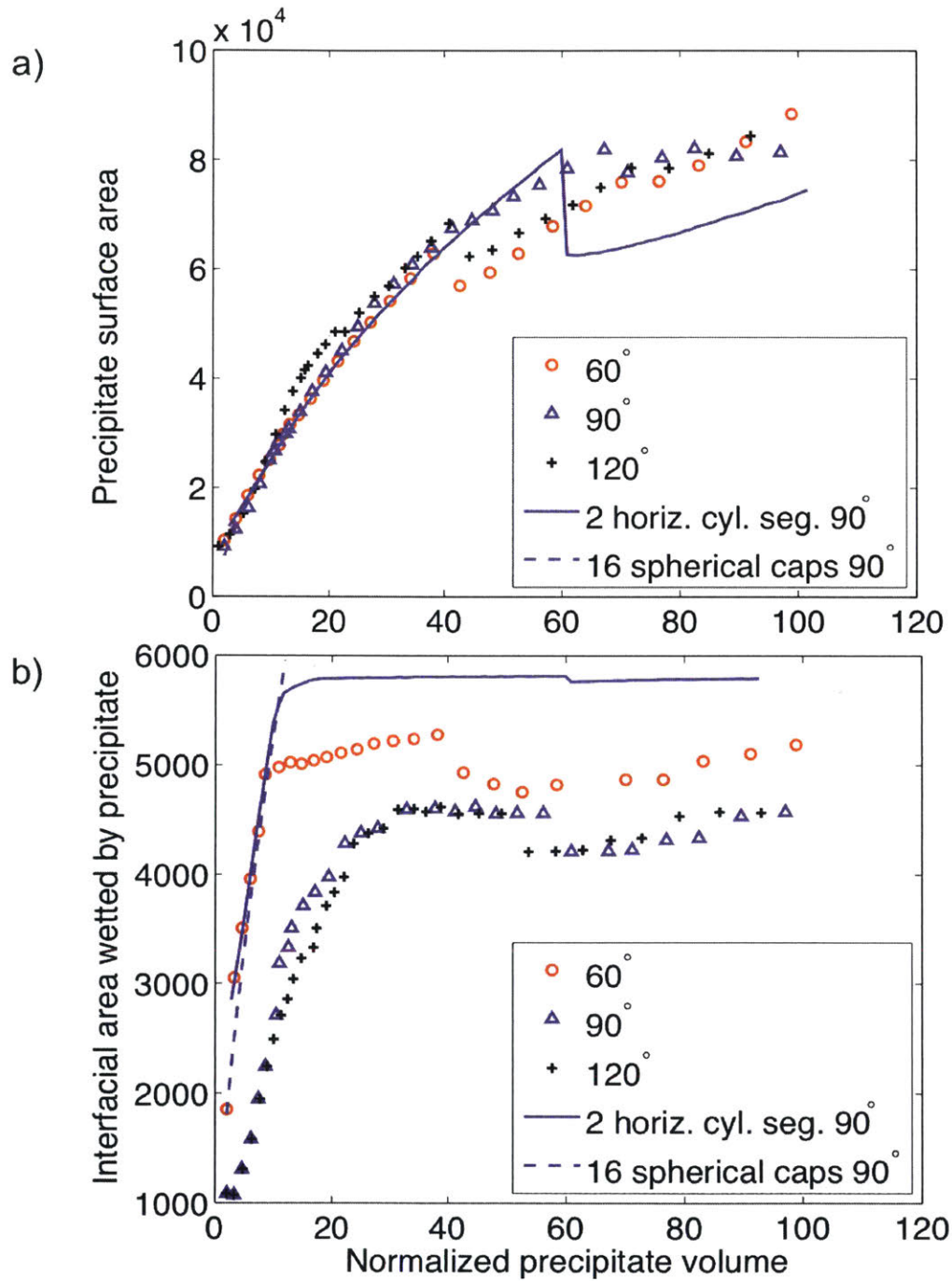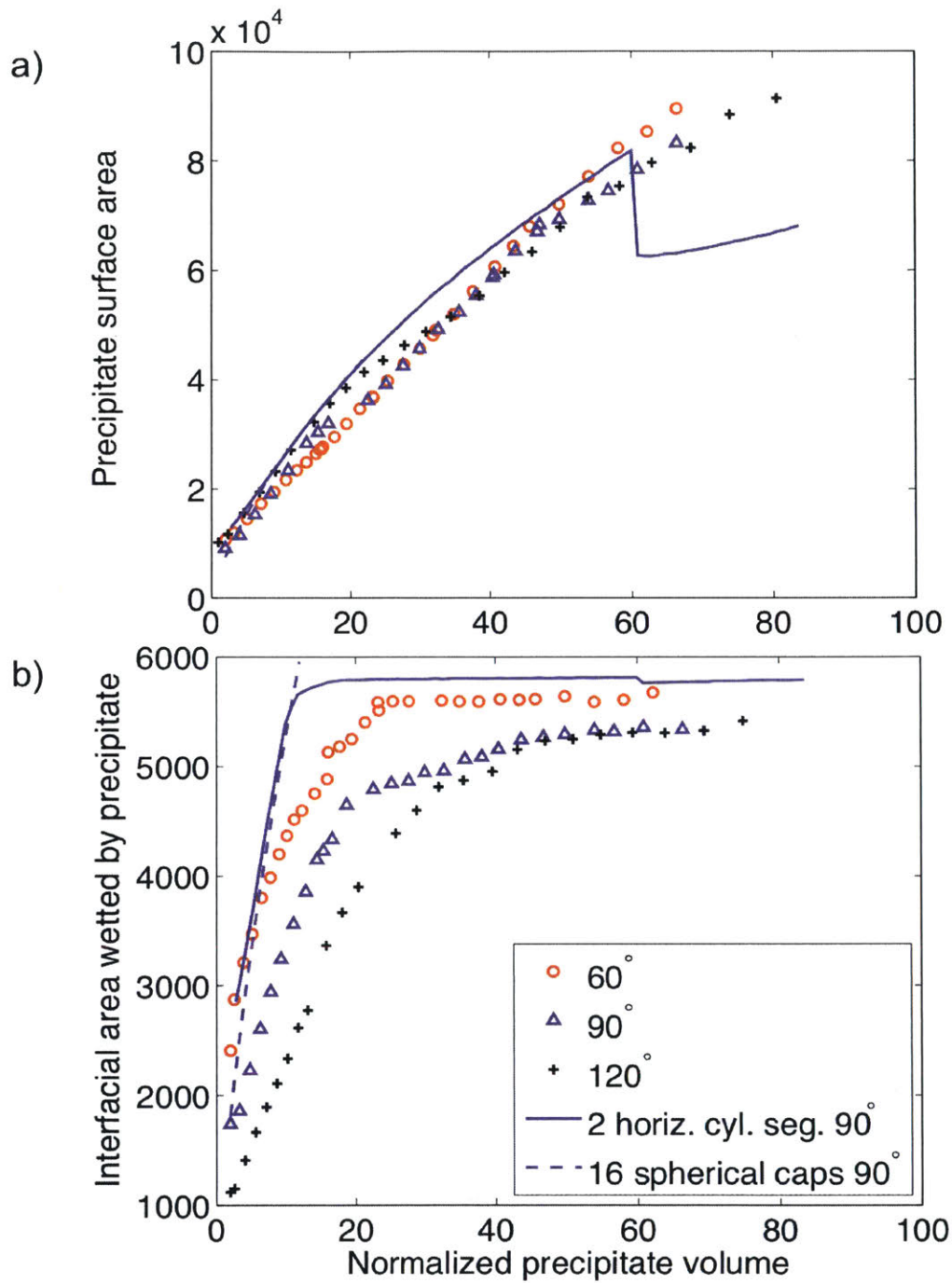
Figure 5-6: a) The plot of the precipitate surface area as a function of normalized precipitate volume for 60° (red circles), 90° (blue triangles), and 120° (black plus signs) wetting angles for two orthogonal wetting ribbons on adjacent interfaces. b)The plot of the interfacial area wetted by the precipitate as a function of normalized precipitate volume for 60°, 90°, and 120° wetting angles for two orthogonal wetting ribbons on adjacent interfaces. References cases are rendered in dashed and solid blue lines.

ting ribbon configurations: a sharp initial increase at low normalized precipitate volumes followed by a leveling off and saturation at higher precipitate volumes. The 60° case has the largest slope and saturates the total wetted area at the lowest normalized precipitate volume of 20. The 90° has a lower slope than the 60° case but a higher slope than the 120° case. However, both the 90° and 120° case saturate at the same normalized precipitate volume of 40. Unlike the single and parallel wetting ribbon configurations, the data for the orthogonal configuration lacks the "wiggles" and drops in the wetted area plots. There are few, if any, dewetting events occurring. This can be explained by the path the precipitate interaction and coalescence took. Rather than forming a combination of more spherical and more cylindrical precipitates, in this case, the precipitates coalesced into a single elongated precipitates. As volume increase, no more coalescence events occurred, (except between the top and bottom interface) and there was no contraction of the precipitate. Rather, the elongated precipitate grew steadily and increased the area it wetted.

5.4   Discussion of wetting ribbon results

In this chapter we used the phase field model developed in Ch. 3 to simulate the behavior of He bubbles on wetting ribbons. Through experimental efforts, it was found that linear wetting ribbons can occur at interfaces due to the glide of dislocation loops in their slip plane. As these loops move through a layer, steps get deposited at the interface. Due to their high energy, these steps form wetting ribbons that are favorable locations for wetting by He precipitates. Because the experimental evidence suggests that these steps are a more preferential site for wetting than MDIs, it is important to understand how they influence the behavior of He precipitate networks. We found that in all wetting ribbon configurations studied, stable elongated precipitate networks do form. Given an interface with uniform wetting properties, or two adjacent interfaces with uniform wetting properties, we would expect either a spherical cap or cylindrical precipitate configuration. Based on the results from the this study and those conducted in previous chapters, we can conclude that interfaces with non-uniform wetting properties allow us to access elongated precipitate structures.

108

Our simulations capture the wetting, growth, and coalescence of He on a single wetting ribbon, two parallel wetting ribbons on adjacent interfaces, and two orthogonal wetting ribbons on adjacent interfaces. However, our model is fairly simple and can be modified to capture more complex physical detail. For example, we modeled the wetting ribbon on a flat interface. In actuality, the high wetting region is due to a nanometer scale step in the interface. Modifying the simulation cell to include the physical step could change the results of the simulation.

Unlike MDIs, these wetting ribbons have a nominally random distribution. Their orientation, however, is set by the dislocation glide planes in the FCC metal. Thus the ribbons point in the <110> directions that lie in the {111} slip planes of Cu. We considered two extreme cases of the orientation of two wetting ribbons relative to one another: one case where one wetting ribbon is directly above the other and one case where one wetting ribbon is orthogonal to the other in the adjacent plane. In a physical system, neither case would be found. While it is likely that two wetting ribbons would be parallel to each other in adjacent planes, these ribbons would likely be offset. Furthermore, rather than wetting ribbons intersecting at 90° angles on adjacent interfaces, the wetting ribbons would intersect at 60°. This is because the <110> directions of the {111} slip plane are oriented at 60° relative to each other.

In our study, we found that introducing a second interface seemed to stabilize the precipitate in it's elongated shape. The layer thickness we estimated was approximately 5nm, corresponding to the smallest possible layer that could be deposited experimentally. As the layer thickness increases and the interfaces move farther away from each other, there exists a critical thickness at which the elongated precipitate would lose its stability. Conducting a series of simulations varying the layer thickness would give insight into what is the maximum layer thickness that can be used and still result in elongated He precipitates.

Though this study does have its limitations, it captured He precipitate behavior to first order. We found that the wetting angle does not have much effect on the final precipitate shape. The history of the precipitate, the order in which coalescence occurred, influences the trajectory of the surface area and interfacial wetted area as a function of precipitate volume. Furthermore, for all the wetting ribbon configurations considered, an elongated

precipitate formed. Finally, we observed that confinement (having 2 interfaces) promotes the formation of an elongated precipitate.

Chapter 6

Conclusion

Societal need for developing alternative energy sources to minimize environmental damage is well established. Despite the many technological challenges that stand in the way, fusion power is a promising possible alternative to fossil fuels with a potentially huge energy pay-out. The successful operation and safety of a fusion reactor hinges on materials selection and design of the plasma-facing wall. This wall needs to withstand extreme conditions and fusion reaction byproducts including implanted helium. Due to its insolubility in metals, there is a strong drive for the helium to escape, leaving behind voids in the material. As these voids grow and link up, the materials structural integrity is lost and the damage to the reactor is irreparable. The current approach to helium management involves maximizing the amount of helium a material can store before voids form, thus only delaying the onset of damage rather than eliminating it. The Demkowicz group has taken a novel approach to solving the helium problem– rather than delaying the formation of voids, we aimed to design a material that would allow for the removal of helium through controlled outgassing, thus eliminating their formation altogether.

In this thesis, a novel materials system was designed that has been experimentally shown to give rise to stable linear helium precipitate networks at the interface. If these channels terminate on a free surface, then helium can safely be removed from the material through outgassing. Furthermore, these channels can be "reused" as nucleation sites for incoming He, minimizing the number of new voids that form and maintaining the structural integrity of the material. In Ch. 2, we used O-lattice theory to determine the distribution

of MDIs, an intrinsic structural interfacial feature which is a preferential helium wetting site, and predicted a favorable materials system that would give rise to channels: Cu-V. In Ch. 3 we developed a phase-field model to capture the capillarity-driven morphological evolution of helium precipitates on nonuniform interfaces. In Ch. 4 we applied our phase field model to the Cu-V system and predicted the formation of channels. In Ch. 5 we applied the phase field model to systems of wetting ribbons and found that these too gave rise to elongated precipitate morphologies. Finally,a Cu-V layered nanocomposite was synthesized, implanted with He, and imaged, demonstrating that our computational prediction was correct and He did form linear channels at a Cu-V interface.

O-lattice theory has been previously used to predict interface structure given some interface crystallography. We used it to solve the inverse problem: given some desired interface structure, what is the corresponding crystallography? We developed maps relating MDI structure and crystallography for interfaces where the {111} FCC plane was parallel to the {110} BCC plane. We then applied design criteria relevant to the helium outgassing problem to these maps and identified numerous possible materials systems that could give us the desired precipitate morphology. These maps can be used for other applications or identification of desired MDI structures by applying design constraints relevant to the given problem. Furthermore, the method we outlined can be applied to other interfaces of interest and can be generalized to incorporate more degrees of freedom beyond lattice parameter ratio and rotation angle. Finally, given the promising results of the predicted CU-V interface, the investigation of fusion relevant materials systems predicted by our method, i.e. those containing tungsten like Cu-W, should be investigated as solutions to the helium problem.

Phase-field modeling is often used in conjunction with Navier-Stokes equations to model fluid flow in engineering systems. We used just phase phase-filed methods to capture the capillarity-driven morphological evolution of He precipitates as a way to significantly cut down on computational time. Typically systems with uniform wetting energies have been modeled rather than non-uniform, patterned interfaces. To our knowledge, no phase field simulations have been done where one phase is added to the system in a quasi-static way. Furthermore our model incorporated a phase dependent mobility to suppress Ostwald ripening phenomena to mimic that of a physical system. From the development of this

model and the small scale study, we have concluded that nonuniform interfaces allow us to access precipitate morphologies beyond equiaxed spherical caps and cylinders. Furthermore, while we found that small wetting angles favor the formation of elongated precipitates, a close spacing of MDIs does not. MDIs that are spaced farther apart may have some advantage in giving rise to linear channels by more effectively pinning the precipitates than closer spaced MDIs. Finally, we conclude that the history, the order of coalescence events, effects the final precipitate morphology. This model can be used to capture first order precipitate behavior at any interface with nonuniform wetting properties.

The phase-field framework we constructed was applied to two systems: a Cu-V interface with a distinct MDI pattern and configurations of wetting ribbons. We observed that linear precipitate channels form at Cu-V interfaces and they are stable. This simulation was validated by experimental results of a helium implanted Cu-V trilayer where helium channels were also observed. In addition to MDIs, interfaces can have wetting ribbons which form due to steps deposited by dislocations slipping in their glide planes. We found that the formation of linear channels is not strongly dependent on wetting angle or the particular wetting ribbon configuration. All investigated cases gave rise to elongated precipitates at a large enough precipitate volume. The coalescence history did effect, however, the path the precipitates took in their morphological evolution. Furthermore, confinement of precipitates between two interfaces seems to encourage formation of linear precipitates.

Using simplified models, we have been able to make predictions about complex interfacial structure and their helium wetting properties. The frameworks and procedures developed can be used in other applications where controlling precipitation of a liquid/gas species at a solid-state interface is desirable. We successfully demonstrated a "proof-of-concept" material that gives rise to linear helium channels and believe that these types of metallic multilayers will be promising class of materials critical to the success of future fusion reactors.

Appendix A

Gaussian Lattice Reduction Algorithm in 2D

A common mathematical problem based on lattices is known as the Shortest Vector Problem (SVP) [66]. This problem entails finding the shortest basis vectors that define a lattice given an any arbitrary set of basis vectors. For higher dimensions, more complex algorithms are employed such as the Lenstra-Lenstra-Lovsz (LLL) algorithm [116]. Gaussian Lattice Reduction is a subset of the LLL algorithm and is used to solve SVPs in 2D [117].

Given two basis vectors of a lattice: $\{\vec{b_1}, \vec{b_2}\}$, we want to find two successive minima of the lattice such that their cross product is minimized. When the cross product is minimized, the length of the two basis vectors are minimized and the angle between them is as close to 90° as possible. To begin, we first ensure that

$$\|\vec{b_1}\| > \|\vec{b_2}\|$$

(A.1)

If this is not the case, swap $\vec{b_1}$ and $\vec{b_2}$ values. Furthermore, $\vec{b_1} \bullet \vec{b_2} \neq 0$. If this condition holds true, the vectors are orthogonal and the smallest basis has been found. To shrink $\vec{b_1}$, we need to add integer multiples of $\vec{b_2}$ to it, such that

$$\vec{b_1}^{\,*} = \|\vec{b_1} - \mu \vec{b_2}\|$$

(A.2)

is minimized where μ is an integer value. To determine μ, we perform the calculation:

$$\mu = \frac{\vec{b_1} \bullet \vec{b_2}}{\|\vec{b_2^2}\|} \tag{A.3}$$

μ is rounded to the nearest integer. The algorithm is robust to arbitrary cutoffs for rounding up or down. Rounding incorrectly will only lead to additional iterations of the algorithm steps. A new vector, $\vec{b_1}^{*}$ is calculated. We now have a new basis defined by the vectors $\vec{b_1}^{*}$ and $\vec{b_2}$. These new basis vector are relabeled as $\vec{b_1}$ and $\vec{b_2}$ such that $\|\vec{b_1}\| > \|\vec{b_2}\|$ and the algorithm repeats. Once the calculation for μ yields a value of .5 or less (0 when rounded), the algorithm terminates and the vectors that remain are the successive minima of the lattice. Every set of vectors calculated at each successive step of the algorithm preserve the lattice. In summary, in 2 dimensions, a basis is considered reduced when the following conditions are met:

$$\|\vec{b_1}\| \geq \|\vec{b_2}\| \tag{A.4}$$

$$\frac{\vec{b_1} \bullet \vec{b_2}}{\|\vec{b_2^2}\|} \leq .5 \tag{A.5}$$

Once the reduced lattice has been found, defining the shortest vector as $\vec{u_1}$ and the second shortest vector as $\vec{v_2}$, it is still necessary to find the perpendicular spacing between the rows of MDIs, $l_\perp$. One way to do so is to take the vector projection of the second shortest vector onto the shortest vector:

$$v_2^{\vec{proj}} = \frac{\vec{v_2} \cdot \vec{u_1}}{|\vec{u_1}|} \frac{\vec{u_1}}{|\vec{u_1}|} \tag{A.6}$$

Then we can find the magnitude of the of the second shortest vector through the Pythagorean Theorem:

$$l_\perp = \sqrt{|\vec{v_2}|^2 - |v_2^{\vec{proj}}|^2} \tag{A.7}$$

The shortest spacing is the magnitude of the shortest vector: $l_{min} = |\vec{u_1}|$. The direction of $l_\perp$ is perpendicular to the direction of $\vec{u_1}$.

Bibliography

[1] R.W. Balluffi and P.D. Bristowe. On the structural unit/grain boundary dislocation model for grain boundary structure. *Surface Science*, 144:28–43, 1984.

[2] J. Hetherly, E. Martinez, Z. F. Di, M. Nastasi, and A. Caro. Helium bubble precipitation at dislocation networks. *Scripta Materialia*, 66(1), 2012.

[3] R. L. Williamson, J. D. Hales, S. R. Novascone, M. R. Tonks, D. R. Gaston, C. J. Permann, D. Andrs, and R. C. Martineau. Multidimensional multiphysics simulation of nuclear fuel behavior. *Journal of Nuclear Materials*, 423(1-3):149–163, 2012.

[4] J. Sheffield. Forecasts for the 21st century. *Journal of Fusion Energy*, 18(1):23–26, 1999.

[5] J. Ongena and Y. Ogawa. Nuclear fusion: Status report and future prospects. *Energy Policy*, 96:770–778, 2016.

[6] S. J. Zinkle. Overview of the us fusion materials sciences program. *Fusion Science and Technology*, 47(4):821–828, 2005.

[7] S. J. Zinkle and L. L. Snead. Designing radiation resistance in materials for fusion energy. *Annual Review of Materials Research, Vol 44*, 44:241–267, 2014.

[8] H Schroeder, W Kesternich, and H Ullmaier. Helium effects on the creep and fatigue resistance of austenitic stainless steels at high temperatures. *Nuclear Engineering Design & Fusion*, 2(1):65–95, 1985.

[9] K. Farrell. Experimental effects of helium on cavity formation during irradiation- a review. *Radiation Effects*, 53:175–194, 1980.

[10] R. E. Galindo, A. van Veen, J. H. Evans, H. Schut, and J. T. M. de Hosson. Protrusion formation and surface porosity development on thermally annealed helium implanted copper. *Nuclear Instruments & Methods in Physics Research Section B-Beam Interactions with Materials and Atoms*, 217(2):262–275, 2004.

[11] Nan Li, J. J. Carter, A. Misra, L. Shao, H. Wang, and X. Zhang. The influence of interfaces on the formation of bubbles in he-ion-irradiated cu/mo nanolayers. *Philosophical Magazine Letters*, 91(1):19–29, 2010.

[12] L. K. Mansur and W. A. Coghlan. Mechanisms of helium interaction with radiation effects in metals and alloys- a review. *Journal of Nuclear Materials*, 119(1), 1983.

[13] R. E. Stoller and G. R. Odette. Analytical solutions for helium bubble and critical radius parameters using a hard-sphere equation of state. *Journal of Nuclear Materials*, 131(2-3), 1985.

[14] M. J. Demkowicz, A. Misra, and A. Caro. The role of interface structure in controlling high helium concentrations. *Current Opinion in Solid State & Materials Science*, 16(3), 2012.

[15] T. Hochbauer, A. Misra, K. Hattar, and R. G. Hoagland. Influence of interfaces on the storage of ion-implanted he in multilayered metallic composites. *Journal of Applied Physics*, 98(12), 2005.

[16] Mikhail Zhernenkov, Michael S. Jablin, Amit Misra, Michael Nastasi, Yongqiang Wang, Michael J. Demkowicz, Jon K. Baldwin, and Jarek Majewski. Trapping of implanted he at cu/nb interfaces measured by neutron reflectometry. *Applied Physics Letters*, 98(24), 2011.

[17] D. Bhattacharyya, M. J. Demkowicz, Y. Q. Wang, R. E. Baumer, M. Nastasi, and A. Misra. A transmission electron microscopy study of the effect of interfaces on bubble formation in he-implanted cu-nb multilayers. *Microscopy and Microanalysis*, 18(1), 2012.

[18] V. K. Gupta and N. L. Abbott. Design of surfaces for patterned alignment of liquid crystals on planar and curved substrates. *Science*, 276(5318):1533–1536, 1997.

[19] J. Aizenberg, A. J. Black, and G. M. Whitesides. Control of crystal nucleation by patterned self-assembled monolayers. *Nature*, 398(6727):495–498, 1999.

[20] Alexander Sinitskii and James M. Tour. Patterning graphene through the self-assembled templates: Toward periodic two-dimensional graphene nanostructures with semiconductor properties. *Journal of the American Chemical Society*, 132(42):14730–14732, 2010.

[21] A. Dupuis and J. M. Yeomans. Droplet dynamics on patterned substrates. *Pramana-Journal of Physics*, 64(6):1019–1027, 2005.

[22] A. Dupuis and J. M. Yeomans. Droplets on patterned substrates: Water off a beetle's back. *International Journal for Numerical Methods in Fluids*, 50(2):255–261, 2006.

[23] A.P. Sutton and R.W. Balluffi. *Interfaces in Crystalline Materials (Monographs on the physics and chemistry of materials)*. Oxford University Press, 1997.

[24] J.W. Matthews and A.E. Blakeslee. Defects in epitaxial multilayers. i. misfit dislocations. *Journal of Crystal Growth*, 27:118, 1974.

[25] J.W. Matthews and A.E. Blakeslee. Defects in epitaxial multilayers. ii. dislocation pile-ups, threading dislocations, slip lines, and cracks. *Journal of Crystal Growth*, 29(3):273, 1975.

[26] J.W. Matthews and A.E. Blakeslee. Defects in epitaxial multilayers. iii. preparation of almost perfect multilayers. *Journal of Crystal Growth*, 32(2):265, 1976.

[27] M. Jin, P. Boolchand, and M. Mitkova. Heterogeneity of molecular structure of ag photo-diffused $ge_{30}se_{70}$ thin films. *Journal of Non-Crystalline Solids*, 354(19-25):2719–2723, 2008.

[28] I. MacLaren. Imaging and thickness measurement of amorphous intergranular films using tem. *Ultramicroscopy*, 99(2-3):103–113, 2004.

[29] P. Keblinski, S. R. Phillpot, D. Wolf, and H. Gleiter. Thermodynamic criterion for the stability of amorphous intergranular films in covalent materials. *Physical Review Letters*, 77(14), 1996.

[30] S. von Alfthan, K. Kaski, and A. P. Sutton. Order and structural units in simulations of twist grain boundaries in silicon at absolute zero. *Physical Review B*, 74(13), 2006.

[31] R. Pareja and J. Serna. Failure of the coincidence site lattice model for grain boundaries in metallic systems. *Scripta Metallurgica*, 13(2):99–101, 1979.

[32] D. Farkas. Coincident site lattice models for grain boundaries in ordered alloys. *Scripta Metallurgica*, 19(4):467–470, 1985.

[33] T. Mori, H. Miura, T. Tokita, J. Haji, and M. Kato. Determination of the energies of 001 twist boundaries in cu with the shape of boundary sio2 particles. *Philosophical Magazine Letters*, 58(1):11–15, 1988.

[34] MA Tschopp and DL McDowell. Structures and energies of sigma 3 asymmetric tilt grain boundaries in copper and aluminium. *Philosophical Magazine*, 87(22):3147–3173, 2007.

[35] J.D. Rittner and D.N. Seidman. Limitations of the structural unit model. *Materials Science Forum*, 207-209:333–336, 1996.

[36] K. M. Knowles. The dislocation geometry of interphase boundaries. *Philosophical Magazine a-Physics of Condensed Matter Structure Defects and Mechanical Properties*, 46(6), 1982.

[37] W. Z. Zhang and G. R. Purdy. O-lattice analyses of interfacial misfit .1. general-considerations. *Philosophical Magazine a-Physics of Condensed Matter Structure Defects and Mechanical Properties*, 68(2), 1993.

[38] W Bollmann. Basic concepts of o-lattice theory. *Surface Science*, 31(1):1–11, 1972.

[39] W BOLLMANN. Classification of crystalline interfaces by means of o-lattice method. *Journal of Microscopy-Oxford*, 102(DEC):233–239, 1974.

[40] J.B. Yang, Y. Nagai, Z.G. Yang, and M. Hasegawa. Quantization of the frank–bilby equation for misfit dislocation arrays in interfaces. *Acta Materialia*, 57(16):4874–4881, 2009.

[41] J. Wang, R. F. Zhang, C. Z. Zhou, I. J. Beyerlein, and A. Misra. Characterizing interface dislocations by atomically informed frank-bilby theory. *Journal of Materials Research*, 28(13):1646–1657, 2013.

[42] J. Wang, R. F. Zhang, C. Z. Zhou, I. J. Beyerlein, and A. Misra. Interface dislocation patterns and dislocation nucleation in face-centered-cubic and body-centered-cubic bicrystal interfaces. *International Journal of Plasticity*, 53:40–55, 2014.

[43] A. J. Vattre, N. Abdolrahim, K. Kolluri, and M. J. Demkowicz. Computational design of patterned interfaces using reduced order models. *Scientific Reports*, 4, 2014.

[44] N. Abdolrahim and M. J. Demkowicz. Determining coherent reference states of general semicoherent interfaces. *Computational Materials Science*, 118:297–308, 2016.

[45] A. J. Vattre and M. J. Demkowicz. Determining the burgers vectors and elastic strain energies of interface dislocation arrays using anisotropic elasticity theory. *Acta Materialia*, 61(14):5172–5187, 2013.

[46] N. Souami, D. Saidi, M. Negache, and A. Ati. Carbon segregation and inclusions effects on surface fracture morphology of a 12*Journal of Materials Engineering and Performance*, 12(6):715–720, 2003.

[47] T. Nakazawa, N. Fujita, H. Kimura, H. Komatsu, H. Kotoh, and H. Kaguchi. Effects of carbon content and chromium segregation on creep rupture properties of low carbon and medium nitrogen type 316 stainless steel. *Tetsu to Hagane-Journal of the Iron and Steel Institute of Japan*, 83(5):317–322, 1997.

[48] M. S. Laws and P. J. Goodhew. Grain-boundary structure and chromium segregation in a 316 stainless-steel. *Acta Metallurgica Et Materialia*, 39(7):1525–1533, 1991.

[49] D. Isheim and D. N. Seidman. Nanoscale studies of segregation at coherent heterophase interfaces in alpha-fe based systems. *Surface and Interface Analysis*, 36(5-6):569–574, 2004.

[50] A. Seki, D. N. Seidman, Y. Oh, and S. M. Foiles. Monte-carlo simulations of segregation at 001 twist boundaries in a pt(au) alloy .1. results. *Acta Metallurgica Et Materialia*, 39(12), 1991.

[51] A. Seki, D. N. Seidman, Y. Oh, and S. M. Foiles. Monte-carlo simulations of segregation at 001 twist boundaries in a pt(au) alloy .2. discussion. *Acta Metallurgica Et Materialia*, 39(12), 1991.

[52] HL Heinisch, F Gao, and RJ Kurtz. Atomistic modeling of helium interacting with screw dislocations in alpha-fe. *Journal of Nuclear Materials*, 367:311–315, 2007.

[53] S. R. L. Couling and R. Smoluchowski. Anisotropy of diffusion in grain boundaries. *Journal of Applied Physics*, 25(12):1538–1542, 1954.

[54] J. Sommer, T. Muschik, C. Herzig, and W. Gust. Silver tracer diffusion in oriented ag/cu interphase boundaries and correlation to the boundary structure. *Acta Materialia*, 44(1):327–334, 1996.

[55] D. Milcius, L. L. Pranevicius, and C. Templier. Hydrogen storage in the bubbles formed by high-flux ion implantation in thin al films. *Journal of Alloys and Compounds*, 398(1-2):203–207, 2005.

[56] P. A. Thorsen, J. B. Bilde-Sorensen, and B. N. Singh. Bubble formation at grain boundaries in helium implanted copper. *Scripta Materialia*, 51(6):557–560, 2004.

[57] P. A. Thorsen, J. B. BildeSorensen, and B. N. Singh. Influence of grain boundary structure: On bubble formation behaviour in helium implanted copper. *Intergranular and Interphase Boundaries in Materials, Pt 2*, 207-:445–448, 1996.

[58] H. L. Heinisch, F. Gao, R. J. Kurtz, and E. A. Le. Interaction of helium atoms with edge dislocations in alpha-fe. *Journal of Nuclear Materials*, 351(1-3):141–148, 2006.

[59] BN Singh, T Leffers, WV Green, and M Victoria. Nucleation of helium bubbles on dislocations, dislocation networks and dislocations in grain-boundaries during 600 mev proton irradiation of aluminum. *Journal of Nuclear Materials*, 125(3):287–297, 1984.

[60] A. Kashinath, A. Misra, and M. J. Demkowicz. Stable storage of helium in nanoscale platelets at semicoherent interfaces. *Physical Review Letters*, 110(8), 2013.

[61] M. J. Demkowicz, R. G. Hoagland, and J. P. Hirth. Interface structure and radiation damage resistance in cu-nb multilayer nanocomposites. *Physical Review Letters*, 100(13), 2008.

[62] A. Kashinath and M. J. Demkowicz. A predictive interatomic potential for he in cu and nb. *Modelling and Simulation in Materials Science and Engineering*, 19(3), 2011.

[63] Pierre-Gilles de Gennes, Francoise Brochard-Wyart, and David Quere. *Capillarity and Wetting Phenomena: Drops, Bubbles, Pearls, Waves*. Springer, New York, 2004.

[64] M Rosen. *Wetting and Its Modification by Surfacants*, book section 6, pages 243–276. Wiley, third edition, 2004.

[65] W BOLLMANN. O-lattice calculation of an fcc-bcc interface. *Physica Status Solidi a-Applied Research*, 21(2):543–550, 1974.

[66] Wei Zhang, Felix Arnold, and Xiaoli Ma. An analysis of seysen's lattice reduction algorithm. *Signal Processing*, 88(10):2573–2577, 2008.

[67] Shahram Sharafat, Akiyuki Takahashi, Koji Nagasawa, and Nasr Ghoniem. A description of stress driven bubble growth of helium implanted tungsten. *Journal of Nuclear Materials*, 389(2):203–212, 2009.

[68] Gary S. Was. *Fundamentals of radiation materials science : metals and alloys / Gary S. Was*. Berlin : Springer, 2007., 2007.

[69] M. J. Demkowicz, R. G. Hoagland, B. P. Uberuaga, and A. Misra. Influence of interface sink strength on the reduction of radiation-induced defect concentrations and fluxes in materials with large interface area per unit volume. *Physical Review B*, 84(10), 2011.

[70] D. Mitlin, A. K. Schmid, and V. Radmilovic. Transmission electron microscopy based study of epitaxy in nb/(100)cu bilayer and cu/nb/(100)cu trilayer nanoscale films. *Applied Physics Letters*, 86(5), 2005.

[71] G. Dobmann, S. N. Korshunov, M. Kroening, Y. V. Martynenko, I. D. Skorlupkin, and A. S. Surkov. Helium and radiation defect accumulation in metals under stress. *Vacuum*, 82(8):856–866, 2008.

[72] G. B. Olson. Computational design of hierarchically structured materials. *Science*, 277(5330):1237–1242, 1997.

[73] H. Choi, D. L. McDowell, J. K. Allen, D. Rosen, and F. Mistree. An inductive design exploration method for robust multiscale materials design. *Journal of Mechanical Design*, 130(3), 2008.

[74] J. B. Condon and T. Schober. Hydrogen bubbles in metals. *Journal of Nuclear Materials*, 207, 1993.

[75] Y. Shen and P. G. Shewmon. Intergranular stress-corrosion cracking of alloy 600 and x-750 in high-temperature deaerated water steam. *Metallurgical Transactions a-Physical Metallurgy and Materials Science*, 22(8), 1991.

[76] R. F. Zhang, J. Wang, I. J. Beyerlein, and T. C. Germann. Dislocation nucleation mechanisms from fcc/bcc incoherent interfaces. *Scripta Materialia*, 65(11):1022–1025, 2011.

[77] I. J. Beyerlein, J. Wang, K. Kang, S. J. Zheng, and N. A. Mara. Twinnability of bimetal interfaces in nanostructured composites. *Materials Research Letters*, 1(2):89–95, 2013.

[78] S. J. Zheng, I. J. Beyerlein, J. S. Carpenter, K. W. Kang, J. Wang, W. Z. Han, and N. A. Mara. High-strength and thermally stable bulk nanolayered composites due to twin-induced interfaces. *Nature Communications*, 4, 2013.

[79] LQ Chen. *Introduction to the Phase-Field Method of Microstructure Evolution*, book section 2. Wiley, 2005.

[80] PC Millett and M Tonks. Application of phase-field modeling to irradiation effects in materials. *Current Opinion in Solid State & Materials Science*, 15(3):125–133, 2011.

[81] J. W. Cahn and J. E. Hilliard. Free energy of a nonuniform system .1. interfacial free energy. *Journal of Chemical Physics*, 28(2):258–267, 1958.

[82] Matthew C. Zwier and Lillian T. Chong. Reaching biological timescales with all-atom molecular dynamics simulations. *Current Opinion in Pharmacology*, 10(6):745–752, 2010.

[83] L. J. Perryman and P. J. Goodhew. A description of the migration and growth of cavities. *Acta Metallurgica*, 36(10):2685–2692, 1988.

[84] W. Z. Han, N. A. Mara, Y. Q. Wang, A. Misra, and M. J. Demkowicz. He implantation of bulk cu-nb nanocomposites fabricated by accumulated roll bonding. *Journal of Nuclear Materials*, 452(1-3):57–60, 2014.

[85] D. B. Butrymowicz, J. R. Manning, and M. E. Read. Diffusion in copper and copper-alloys .5. diffusion in systems involving elements of group-va. *Journal of Physical and Chemical Reference Data*, 6(1):1–50, 1977.

[86] Nikolas Provatas and Ken Elder. *Phase-Field Methods in Materials Science and Engineering*. John-Wiley & Sons, Germany, 2011.

[87] PC Millett, A El-Azab, S Rokkam, M Tonks, and D Wolf. Phase-field simulation of irradiated metals part i: Void kinetics. *Computational Materials Science*, 50(3):949–959, 2011.

[88] PC Millett, MR Tonks, SB Biner, LZ Zhang, K Chockalingam, and YF Zhang. Phase-field simulation of intergranular bubble growth and percolation in bicrystals. *Journal of Nuclear Materials*, 425(1-3):130–135, 2012.

[89] Lorenz Ratke and Peter W Voorhees. *Growth and Coarsening: Ostwald Ripening in Material Processing*. Springer, New York, 2002.

[90] M. J. Demkowicz, D. Bhattacharyya, I. Usov, Y. Q. Wang, M. Nastasi, and A. Misra. The effect of excess atomic volume on he bubble formation at fcc-bcc interfaces. *Applied Physics Letters*, 97(16), 2010.

[91] F Gao, HL Heinisch, and RJ Kurtz. Diffusion of he interstitial and di-he cluster at grain boundaries in alpha-fe. *Journal of Nuclear Materials*, 367:446–450, 2007.

[92] H. Trinkaus and B. N. Singh. Helium accumulation in metals during irradiation - where do we stand? *Journal of Nuclear Materials*, 323(2-3):229–242, 2003.

[93] L. M. Hale, J. A. Zimmerman, and B. M. Wong. Large-scale atomistic simulations of helium-3 bubble growth in complex palladium alloys. *Journal of Chemical Physics*, 144(19), 2016.

[94] D. M. Stewart, Y. N. Osetsky, R. E. Stoller, S. I. Golubov, T. Seletskaia, and P. J. Kamenski. Atomistic studies of helium defect properties in bcc iron: Comparison of he-fe potentials. *Philosophical Magazine*, 90(7-8):935–944, 2010.

[95] K. Hattar, M. J. Demkowicz, A. Misra, I. M. Robertson, and R. G. Hoagland. Arrest of he bubble growth in cu-nb multilayer nanocomposites. *Scripta Materialia*, 58(7):541–544, 2008.

[96] T. Korhonen, M. J. Puska, and R. M. Nieminen. Vacancy-formation energies for fcc and bcc transition-metals. *Physical Review B*, 51(15):9526–9532, 1995.

[97] J. W. Cahn and J. E. Hilliard. Free energy of a nonuniform system .3. nucleation in a 2-component incompressible fluid. *Journal of Chemical Physics*, 31(3):688–699, 1959.

[98] Pengtao Yue and James J. Feng. Wall energy relaxation in the cahn-hilliard model for moving contact lines. *Physics of Fluids*, 23(1), 2011.

[99] J. W. Cahn. Critical-point wetting. *Journal of Chemical Physics*, 66(8):3667–3672, 1977.

[100] Michael R. Tonks, Derek Gaston, Paul C. Millett, David Andrs, and Paul Talbot. An object-oriented finite element framework for multiphysics phase field simulations. *Computational Materials Science*, 51(1):20–29, 2012.

[101] A. Kashinath, P. Wang, J. Majewski, J. K. Baldwin, Y. Q. Wang, and M. J. Demkowicz. Detection of helium bubble formation at fcc-bcc interfaces using neutron reflectometry. *Journal of Applied Physics*, 114(4), 2013.

[102] A. Caro, D. Schwen, and E. Martinez. Structure of nanoscale gas bubbles in metals. *Applied Physics Letters*, 103(21), 2013.

[103] G. R. Odette and R. E. Stoller. A theoretical assessment of the effect of microchemical, microstructural and environmental mechanisms on swelling incubation in austenitic stainless-steels. *Journal of Nuclear Materials*, 122(1-3):514–519, 1984.

[104] L. K. Mansur, E. H. Lee, P. J. Maziasz, and A. P. Rowcliffe. Control of helium effects in irradiated materials based on theory and experiment. *Journal of Nuclear Materials*, 141:633–646, 1986.

[105] B. M. Mognetti, H. Kusumaatmaja, and J. M. Yeomans. Drop dynamics on hydrophobic and superhydrophobic surfaces. *Faraday Discussions*, 146:153–165, 2010.

[106] SY Hu, CH Henager, HL Heinisch, M Stan, MI Baskes, and SM Valone. Phase-field modeling of gas bubbles and thermal conductivity evolution in nuclear fuels. *Journal of Nuclear Materials*, 392(2):292–300, 2009.

[107] A. Butterfield, V. Chan, S. Ghosh, K. Thornton, M. Tonks, and Zhang Yongfeng. Obtaining elastic constants using phase field crystal modeling. *Transactions of the American Nuclear Society*, 110:925–6, 2014.

[108] D. V. Yuryev and M. J. Demkowicz. Computational design of solid-state interfaces using o-lattice theory: An application to mitigating helium-induced damage. *Applied Physics Letters*, 105(22), 2014.

[109] D.V. Yuryev and M.J. Demkowicz. Modeling growth, coalescence, and stability of helium precipitates on patterned interfaces. *Modelling Simul. Mater. Sci. Eng.*, 25(015003), 2016.

[110] S. Plimpton. Fast parallel algorithms for short-range molecular-dynamics. *Journal of Computational Physics*, 117(1):1–19, 1995.

[111] H. L. Skriver and N. M. Rosengaard. Surface-energy and work function of elemental metals. *Physical Review B*, 46(11):7157–7168, 1992.

[112] M. W. Finnis and J. E. Sinclair. A simple empirical n-body potential for transition-metals. *Philosophical Magazine a-Physics of Condensed Matter Structure Defects and Mechanical Properties*, 50(1):45–55, 1984.

[113] A. Misra, J. P. Hirth, and R. G. Hoagland. Length-scale-dependent deformation mechanisms in incoherent metallic multilayered composites. *Acta Materialia*, 53(18):4817–4824, 2005.

[114] Shijian Zheng, Shuai Shao, Jian Zhang, Yongqiang Wang, Michael J. Demkowicz, Irene J. Beyerlein, and Nathan A. Mara. Adhesion of voids to bimetal interfaces with non-uniform energies. *Scientific Reports*, 5, 2015.

[115] RW Balluffi, SM Allen, and WC Carter. *Kinetics of Materials*. Wiley, Hoboken, NJ, 2005.

[116] I. Semaev. A 3-dimensional lattice reduction algorithm. *Cryptography and Lattices*, 2146:181–193, 2001.

[117] P. Q. Nguyen and D. Stehle. Low-dimensional lattice basis reduction revisited. *Algorithmic Number Theory, Prceedings*, 3076:338–357, 2004.